Highly active chromosome regions preferentially associate with two perispeckle networks that partition the interchromatin space

Authors:

Neha Chivukula Venkata[1], Jiah Kim[1], Gabriel Faber[2], Saireet Misra[1], Atabek Bektash[3,4], Pankaj Chaturvedi[1], Gabriela Hernanadez[1], Joseph Dopie[1], Masato T. Kanemaki[3,4,5], Kyu Young Han[6], Yaron Shav Tal[2] and Andrew S. Belmont[1,7,8]

Affiliations

1. Department of Cell and Developmental Biology, University of Illinois at Urbana-Champaign, Urbana, IL
2. The Mina and Everard Goodman Faculty of Life Sciences, Bar-Ilan University, Ramat Gan 5290002, Israel.
3. National Institute of Genetics, Research Organization of Information and Systems (ROIS), Mishima, Shizuoka 411-8540, Japan.
4. Graduate Institute for Advanced Studies, SOKENDAI, Mishima, Shizuoka 411-8540, Japan
5. Department of Biological Science, Graduate School of Science, The University of Tokyo, Tokyo 113-0033, Japan
6. CREOL, The College of Optics and Photonics, University of Central Florida, Orlando, FL, USA
7. Center for Biophysics and Quantitative Biology, University of Illinois at Urbana-Champaign, Urbana, IL
8. Carl R. Woese Institute for Genomic Biology, University of Illinois at Urbana-Champaign, Urbana, IL

Key Words:

Genome organization, active chromatin, interchromatin compartment, nuclear speckles

Abstract

A subset of highly active chromosomal "hot zones" reproducibly positions adjacent to nuclear speckles (NS). Genes within these regions amplify their expression only with NS contact. However, gene expression differences inversely correlate with differences in NS distance, genome-wide. We hypothesized the existence of additional gene expression "niches" away from, but spatially correlated with, NS. Here we report the identification of two dynamic perispeckle patterns of protein concentrations extending outwards from NS and persisting even after NS are eliminated. Highly active chromosome regions which weakly associate with NS instead show close, NS-independent association with these perispeckle patterns. Additionally, transcripts from model intron-containing versus intronless genes associate differentially with these two patterns. While genes within NS-associated genomic regions are predominantly downregulated upon NS depletion, genes associated with perispeckle patterns are biased towards upregulation. We suggest the interchromatin space is partitioned into additional gene expression “niches”- surrounding and extending from NS - that may be involved in mRNA and gene dynamics.

Introduction

Nuclear speckles (NS) were first suggested to act as a gene expression hub for a subset of active genes based on a survey of ~20 active genes using fluorescence in situ hybridization (FISH) (Smith et al., 1999; Hall et al., 2006). Over the past several years, this model has now been validated by multiple orthogonal genome-wide approaches, including TSA-seq, SPRITE, and highly multiplexed immuno-FISH (Quinodoz et al., 2018; Chen et al., 2018; Su et al., 2020; Takei et al., 2021; Zhang et al., 2021; Gholamalamdari et al., 2025). A distinct subset of chromosomal regions- GC-rich, gene-dense, and enriched with shorter genes with fewer introns and house-keeping genes- show high frequency association with NS and mean NS distances of just several hundred nm (Chen et al., 2018). While several developmentally regulated genes have been shown to move from the nuclear lamina to NS after their gene activation, unexpectedly most of these Speckle-Associated Domains (SPADs) are highly conserved across multiple cell types (Zhang et al., 2021; Takei et al., 2021, 2023; Bhat et al., 2024). The most highly expressed genes show a pronounced enrichment in SPADs, as do CTCF binding sites, super-enhancers, and active marks such as H3K27ac, H3K9ac, and K3K79me3 (Chen et al., 2018; Yu et al., 2023b; Wang et al., 2021; Joo et al., 2023). In addition to this correlation of high levels of gene expression with NS association, live-cell imaging revealed a striking increase in *HSPA1* gene expression occurring within several minutes of gene movement and contact with NS (Khanna et al., 2014; Kim et al., 2020). Similar “amplification of gene expression” with NS association was inferred for several genes flanking the *HSPA1* locus (Kim et al., 2020), for the *HSPH1* gene (Zhang et al., 2021), and for several hundred p53-

responsive genes (Alexander et al., 2021). Additionally, NS proximity has been shown to increase the efficiency of RNA splicing (Bhat et al., 2024).

While these results firmly establish NS as a nuclear hub for a subset of active genes, they raise the obvious next question of whether other nuclear compartments might similarly act as a hub for different subsets of active genes. Several previous observations led us to speculate that there might be additional nuclear compartments which act as local niches for gene expression.

First, we observed two types of chromosome regions with similarly elevated levels of gene expression; both types of these gene expression "hot-zones", on average several hundred kbp in size, aligned with SON TSA-seq local maxima (Chen et al., 2018) (Gholamalamdari et al., 2025). Whereas high-amplitude, "Type I" SON TSA-seq peaks corresponded to chromosome regions strongly associated with NS, low-amplitude, "Type II" SON TSA-seq peaks corresponded to chromosome regions with weak association with NS (Gholamalamdari et al., 2025). Second, based on the shapes of the Type I SON peaks, aligned with corresponding Lamin B TSA-seq valleys, we inferred chromosome trajectories extending from the nuclear lamina and terminating adjacent to NS for the several hundred to thousand kbp lying between Type I SON TSA-seq peaks and the nearest LAD, as validated for several trajectories by DNA FISH (Chen et al., 2018). By analogy, we hypothesized similar chromosome trajectories extending from the nuclear lamina towards an unknown nuclear body/compartment that Type II SON TSA-seq peaks would associate with instead of NS. Third, chromosome regions shifting in different cell types from far to moderate distances to NS showed similar biases towards increases in gene expression as other chromosome regions that

97 shifted from moderate to near distances to NS (Zhang et al., 2021). Fourth, live-cell
98 imaging revealed repeated nucleation and then movement of small NS towards larger
99 NS within DNA-depleted channels connecting the NS (Kim et al., 2019). Despite the
100 known fast "constrained diffusion" of chromosome loci over radii of ~500-1000 nm
101 (Marshall et al., 1997; Chubb et al., 2002; Levi et al., 2005), these channels remained
102 DNA-depleted over tens of minutes suggesting that some unknown non-chromatin
103 component(s) might be occupying these channels.

104 Our observations showing an inverse relationship between changes in gene
105 expression and changes in NS proximity across a wide range of NS distances created
106 an apparent paradox when compared to our live-cell imaging observations which
107 instead showed amplification of gene expression of certain genes only after actual
108 microscopic contact with NS. To resolve this paradox, we hypothesized that just as
109 certain genes might need to actually contact NS to enhance their gene expression,
110 other genes might need to contact a different nuclear body/compartment to enhance
111 their gene expression. If these putative additional nuclear bodies/compartments were
112 themselves spatially correlated with NS, then a gene movement leading to actual
113 contact with these nuclear bodies/compartments would appear by SON TSA-seq as a
114 relative movement towards but not close to NS, resolving the apparent paradox.

115 Here we describe identification of several markers for each of two interwoven
116 perispeckle staining patterns. Together, these perispeckle patterns meet our predictions
117 of additional novel compartment(s) surrounding and extending from NS and serving as
118 alternative gene expression hubs for a subset of highly active genes not associated with
119 NS. The differential association of intron-rich versus intron-poor mRNAs with these two

120 perispeckle staining patterns, together with the known roles of many of their marker
121 proteins in RNA processing and/or RNA export, additionally suggests that these
122 perispeckle staining patterns may define nuclear compartments that help spatially
123 integrate the processes of transcription, RNA processing, and nuclear export.
124

RESULTS

Screening for potential markers of alternative "gene expression hubs"

As summarized in the Introduction, we postulated the existence of a nuclear compartment(s), itself spatially correlated with NS, that might act as an alternative hub for the several hundred kbp chromosome gene expression "hot-zones" that were not closely associated with NS (Fig. 1A). We imagined that such a compartment(s) might lie adjacent to and/or extend outwards from NS. Thus, shifts of chromosome regions towards this compartment(s) would then score as an increase in the NS TSA-seq score, which probes the proximity of chromosome regions to NS on an approximately micron-length scale.

We previously applied Tyramide Signal Amplification coupled to mass spectrometry (TSA-MS) to identify NS-enriched proteins (Dopie et al., 2020). Similarly to TSA-seq, TSA-MS exploits the predicted and measured exponential decay of tyramide (phenol)-biotin free radicals as they diffuse outwards from the immunostained target. Given the ~1-micron radius of this spreading (Chen et al., 2018), we realized that tyramide labeling of proteins would extend beyond the NS to proteins in a significant volume surrounding each NS. We therefore ranked proteins by their relative enrichment in NS versus near centromeres, stained by CENPA, to distinguish between proteins specifically enriched near NS versus proteins present throughout the nucleus, including near centromeres; we expected that centromeres would represent a nuclear local environment with low levels of proteins involved in gene expression.

Whereas 74% of the top 91 ranked proteins had been previously reported as colocalizing with NS, the next 92-200 top ranked proteins showed a sharp decrease in

148 previously reported NS colocalization to ~13% (Dopie et al., 2020). Despite this drop in
149 NS colocalization, a large fraction of these proteins, similar to the fraction of known NS-
150 enriched proteins, was connected to various steps in gene expression. Therefore, we
151 reasoned these moderately-ranked proteins were likely enriched in transcriptionally
152 active regions surrounding NS, and thus were candidates for proteins marking our
153 hypothesized gene expression compartment(s) surrounding and extending outwards
154 from NS (yellow regions in Fig. 1A).

155 We identified 25 candidate proteins from this list of moderately-enriched proteins
156 that were reported to show non-diffuse immunostaining within the interchromatin space
157 (ICS), based on the literature and/or the Human Protein Atlas (Pontén et al., 2009). As
158 a first screen, we examined the nuclear distribution of each of these candidate proteins
159 relative to both NS and DNA-staining, looking for candidate proteins that formed distinct
160 staining patterns within and/or surrounding NS and extending out into areas of low
161 DNA-staining corresponding to the ICS (Fig. 1B, left). We visualized their nuclear
162 distribution either using transiently expressed EGFP fusion proteins or through
163 immunostaining when antibodies were available.

164 Among these 25 proteins, essentially all showed some type of nondiffuse pattern,
165 with foci of higher intensity throughout the nucleoplasm (SFig. 1A-B). However, there
166 was a continuum in the extent of the nuclear area occupied outside of NS by higher
167 than background intensities. Proteins such as SRRM2 and RBM25 showed little
168 staining outside of NS, while proteins such as DDX41 and PNN showed staining
169 occupying most of the nucleus (SFig. 1A-C). We focused on proteins which showed
170 intermediate occupancy between these extremes, with patterns of staining extending

171 between NS and throughout the nucleus, even extending all the way to the nuclear
172 periphery (Fig. 1B, SFig. 1A-C).
173 For these proteins in this intermediate nuclear occupancy category (SFig. 1B-C),
174 we observed two "perispeckle" categories of staining. We chose DDX39B and THRAP3
175 as founding members of these two intermediate patterns (SFig. 1C), which both
176 occupied ~40% of the nuclear area outside of NS (SFig. 1B). First, we observed
177 proteins distributions similar to THRAP3 in which the protein was not concentrated
178 within NS but was high in concentration surrounding NS (Fig. 1C, SFig. 1A). Second,
179 we observed protein distributions similar to DDX39B in which the protein was most
180 highly concentrated within NS (Fig. 1D, SFig.1A). These differences were made clearer
181 by comparison of the cumulative protein intensities within versus outside NS (SFig. 1C).
182 Finally, there were proteins that showed non-diffuse staining throughout the nuclear
183 interior, but with little relationship to NS. Examples included SAFB and HNRNPM (SFig.
184 1A, 1C).
185 We decided to ask whether proteins within the same perispeckle categories
186 might colocalize with each other. We did this by comparing protein colocalization with
187 THRAP3 for the first category and DDX39B for the second category (Fig. 1B, right
188 panel). To facilitate this screening, we used CRISPR-mediated knock-ins to
189 fluorescently tag endogenously expressed proteins, constructing U2OS cell lines stably
190 expressing either the combination of EGFP-SON and mCherry-THRAP3 or EGFP-SON
191 and mCherry-DDX39B (see Methods). This avoided the overexpression induced
192 changes in protein distribution sometimes seen after transient transfection (Fig. 1B).
193 We then used immunofluorescence to ask which other candidate proteins overlapped

194 extensively with either DDX39B or THRAP3 (Fig. 1B). Due to the lack of a suitable
195 antibody for MAGOH, we utilized lentivirus-based transduction of a mCherry-MAGOH
196 expression cassette followed by immunostaining of THRAP3/DDX39B.
197 Several additional candidate proteins shared high colocalization for either
198 THRAP3 or with DDX39B, suggesting that they were additional components of these
199 perispeckle patterns. We named the intranuclear protein distribution overlapping with
200 THRAP3 as "Perispeckle THRAP3 Pattern" (PSTP) and the intranuclear protein
201 distribution overlapping with DDX39B as "Perispeckle DDX39B Pattern" (PSDP) (Fig.
202 1C-E). Additional proteins showed their own distinctive nuclear distributions (SFig. 1D);
203 thus, the ICS is likely further subdivided into additional novel
204 networks/condensates/bodies that might partially overlap with PSTP and/or PSDP. For
205 example, PLRG1 was enriched inside NS, similar to PSDP, but outside of NS
206 colocalized with PSTP (SFig. 1D, F).
207 PSTP markers currently include THRAP3 (BCLAF2) and its paralog BCLAF1
208 (Fig. 1 B-C,1E). Additionally, PLRG1 overlaps with PSTP outside of nuclear speckles
209 (SFig. 1E). PSDP markers currently include DDX39B (UAP56), RBM8A (Y14), MAGOH,
210 and POLDIP3 (Fig. 1D,F, SFig. 1D). DDX39B was previously described as enriched in
211 NS but also enriched in the region surrounding NS (Kota et al., 2008). Here we show
212 that DDX39B together with other PSDP components also radiate outwards from NS in
213 thread-like projections that frequently connect neighboring speckles (Fig 1. D,F) while
214 forming a network-like pattern which in some nuclear regions show small foci lining up
215 in linear arrangements (Fig 1D- inset orange box).

Next, we examined how MALAT1 localized relative to these perispeckle patterns, as MALAT1- a long, noncoding RNA (lncRNA)- is spatially related to NS (Fei et al., 2017). Functionally, MALAT-1 associates with certain transcription factors and coactivators (Arun et al., 2020) and has been implicated in the regulation of alternative splicing (Miao et al., 2022). Using an oligolibrary containing 100 probes targeted against MALAT1, we observed both the high NS-enrichment of MALAT1 as well as single RNAs within the ICS. MALAT1 single RNAs away from NS were seen either overlapping or at the edge of both THRAP3 and DDX39B foci (SFig. 1G). Specifically, ~50-60% of MALAT1 RNA signal within the interchromatin space overlapped with both THRAP3 and DDX39B outside NS, using Otsu thresholding (Otsu, 1979) to segment MALAT1, THRAP3, and DDX39B intensities (SFig. 1G).

In summary, we have identified two novel “perispeckle patterns” that subdivide the interchromatin space, as defined by the specific localization patterns of nuclear proteins already reported to be involved in gene expression. Moving forward, we focused the differential localization of THRAP3 (PSTP) versus DDX39B (PSDP) as markers of these two perispeckle staining distributions.

Highly dynamic PSTP and PSDP networks which repeatedly recur within the same or nearby interchromatin space

Projections of higher intensity THRAP3 and DDX39B staining extend outwards from NS forming apparent networks within the interchromatin space.

Fixation can alter the cellular distribution of intrinsically disordered domain-containing proteins (Irgen-Gioro et al., 2022). We therefore used live-cell imaging in

239 U2OS cells to confirm similar PSTP and PSDP distributions in live cells and visualize
240 their dynamics over seconds (Fig. 2A-B) to hours (Fig. 2C-D) using the dual SON and
241 THRAP3 or SON and DDX39B tagged cell lines.

242 Both THRAP3 and DDX39B show non-diffuse high local concentration in linear
243 extensions that appear and disappear every few seconds in the vicinity of speckles (Fig.
244 2A&A', 2B&B', Videos 1&2). Summing these 2D projections over a time of 1 minute
245 reveals a clearer network distribution for both THRAP3 and DDX39B due to repeated
246 recurrence of these projections in the same spatial locations (Fig. 2A-B, white arrows).
247 Thus, while both the PSTP and PSDP are highly dynamic in a timescale of seconds,
248 their extensions averaged over time are quasi-stable over a timescale of minutes.

249 Over a much longer timescale of up to 10 hours, PSTP and PSDP networks
250 preserve their overall nuclear distributions despite their fast dynamics (Fig. 2C-D). NS
251 show occasional movements and fusion and fission events within relatively stable DNA-
252 depleted regions (Videos 3&4). PSTP and PSDP were more dynamic, showing
253 repeated appearance/disappearance of thread-like extensions over several minute
254 intervals within the same DNA-depleted spaces surrounding and between NS (Fig.
255 2C&D Videos 3&4). Because these projections tend to reform in the same or similar
256 regions over time, the overall nuclear distributions of PSTP and PSDP remain relatively
257 stable over longer time periods. In a companion paper, we explore these dynamics in
258 greater detail for both SON and two PSDP members- DDX39B and MAGOH (Kim et al.,
259 2025).

260

261 **PSTP and PSDP subdivide the interchromatin space and respond differently to**
262 **functional and physiological perturbations**

263 THRAP3 and DDX39B, our marker proteins for PSTP and PSDP respectively,
264 were both previously reported as overlapping with and/or surrounding NS (Lee et al.,
265 2010; Kota et al., 2008). Because PSTP and PSDP markers also occupy
266 interchromatin space further away from NS and throughout the nucleus, we next
267 examined their relative spatial distribution outside of NS. Across the range of spatial
268 resolution provided by wide-field deconvolution and STORM super resolution light
269 microscopy, THRAP3 and DDX39B staining “networks” appear largely juxtaposed rather
270 than coincident within the interchromatin space outside of NS (Fig. 3A-B). They are
271 significantly less colocalized relative to each other than the colocalization seen for other
272 components of PSTP with THRAP3 or other components of PSDP with DDX39B
273 (Fig.1E-F, SFig.1F-G).
274 After transcriptional inhibition, many NS components, including SON and a
275 number of splicing factors, are known to concentrate further within NS with a
276 concomitant decrease in their nucleoplasmic concentrations (Spector and Lamond,
277 2011); this is accompanied by NS rounding, enlargement and fusion (Kim et al., 2019).
278 However, the THRAP3 and DDX39B staining networks responded differently
279 after transcriptional inhibition, providing further support for their independent nuclear
280 localization. Between 0-2 hours of transcriptional inhibition by DRB (5,6-dichloro-1-beta-
281 D-ribofuranosylbenzimidazole), the thread-like, diffuse network of THRAP3 staining
282 outside of NS consolidates into fewer but more distinct threads, that then breakup into
283 distinct foci aligned along linear paths, plus larger concentrations adjacent to and
284 surrounding NS (Fig. 3C, Video 5). In contrast, the DDX39B distribution appeared
285 relatively intact, although their stability over time may decrease as reported elsewhere

286 (Kim et al., 2025) (Fig. 3D). DRB inhibits CDK9 and thus transcriptional pause release
287 (Bensaude, 2011; Yankulov et al., 1995). We observed similar disruption but to a lesser
288 extent after inhibiting transcription instead using either Triptolide (SFig 3A, which inhibits
289 the XBP subunit of TFIIH and thus transcriptional initiation (Titov et al., 2011), and α-
290 amanitin (SFig. 3B), which initially inhibits but then degrades RNA Pol II over the ~6 hr
291 treatment time (Nguyen, 1996).

292 To quantify the changes in THRAP3 network upon DRB treatment, we used a
293 function "skeletonize" which uses binary thinning/erosion until a one-pixel wide
294 representation remains. These one-pixel wide chains are called "skeletons" that retain
295 both the shape and connectivity of the original image (SFig. 3C). Using this skeletonize
296 function, we measured two parameters per nucleus: 1) total skeleton length, defined as
297 the sum of all skeletons; 2) the number of connections, where each connection is
298 defined as group of connected pixels >5 pixel length.

299 Based on these parameters, the THRAP3 distribution shows both a reduction in
300 total skeleton length and in the number of connections. In contrast, the DDX39B
301 distribution remains relatively intact (Fig. 3E-F). DRB treatment similarly disrupted PSTP
302 member BCLAF1 distribution which also formed foci which colocalized with THRAP3
303 foci (SFig. 3D-E). However, PSDP member RBM8A shows a heterogenous response
304 within the cell population, ranging from minimal to relatively significant perturbation
305 (SFig.3F-G). The RBM8A network, on average, breaks up from a continuous structure
306 to multiple long thread-like structures with DRB treatment as reflected in both the
307 decrease in total skeleton length and increase in the number of connections (SFig. 3G-
308 H).

309 In summary, we conclude that PSTP and PSDP form spatially and functionally
310 distinct networks that subdivide the interchromatin space.
311
312 **RNA Pol II Ser2p foci localize in close proximity to the PSTP and PSDP networks**
313 We next examined the spatial distribution of RNA Pol II foci relative to PSTP and
314 PSDP (Fig. 4). Antibodies against the Ser5p and Ser2p epitopes of the C-terminal
315 domain (CTD) of the largest RNA Pol II subunit recognize the early initiation versus
316 later elongating forms of RNA Pol II, respectively (reviewed in (Egloff and Murphy,
317 2008)). Immunostaining using these antibodies reveals ~60 nm diameter foci, originally
318 termed “RNA Pol II factories” that map near sites of transcription (Jackson et al., 1993;
319 Iborra et al., 1996; Pombo, 1999). Initially proposed as actual transcription sites (Martin
320 and Pombo, 2003; Xie et al., 2006), the functional significance of these transcription
321 factories remains unclear.
322 Although an increased density of RNA Pol II Ser5p and Ser2p foci have
323 previously been described as surrounding the NS periphery, large numbers of RNA Pol
324 II Ser2p and Ser5p foci away from NS are distributed throughout the nuclear interior in
325 no obvious pattern (Chen et al., 2018) (Fig. 4A&D). Immunostaining, however, now
326 reveals a striking spatial correlation of these RNA Pol II foci localized away from NS
327 with the THRAP3 and DDX39B networks (Fig. 4B-C and 4E-F).
328 We used an intensity threshold of 40% of local intensity maxima to segment foci
329 of both THRAP3 and DDX39B (SFig. 4). Median distances of both Ser5p and Ser2p
330 RNA Pol II foci are ~0.2 μm to the nearest edges of THRAP3 foci (Fig. 4K, magenta and
331 purple). Ser5p RNA Pol II foci are similarly close to DDX39B foci (Fig. 4K, light green),

332 while Ser2p RNA Pol II foci show a somewhat increased distance distribution but
333 remain mostly within ~0.5 μm to DDX39B foci (Fig. 4K, dark green).
334 Thus, RNA Pol II foci, used as proxies for mapping sites of active transcription,
335 nearly all map within a few hundred nm of THRAP3 or DDX39B foci, supporting the idea
336 of PSTP and PSDP acting as additional nuclear niches closely associated with
337 transcriptionally active chromosome loci.
338
339 **Gene expression hot zones interact preferentially with PSTP and PSDP as**
340 **measured by TSA-seq**
341 To follow up our demonstration of the close association of RNA pol II foci with
342 perispeckle patterns, we next asked if, as hypothesized (Fig. 1A), Type II SON TSA-seq
343 peaks would show a close association with one or both perispeckle patterns similar to
344 how Type I SON TSA-seq peaks show a close association with NS. More specifically,
345 we used TSA-seq to compare the association of Type II SON TSA-seq peaks with the
346 PSTP and/or the PSDP versus NS.
347 We combined the “super-saturation” TSA-seq 2.0 protocol (Zhang et al., 2021)
348 with the use of dithiothreitol (DTT) to improve the TSA-seq spatial resolution, as
349 described in the original TSA-seq 1.0 protocol (Chen et al., 2018). DTT improves spatial
350 resolution by decreasing the lifetime, and therefore the diffusion radius of the tyramide
351 free-radical, while the "super-saturation" protocol greatly reduces the number of cells
352 required for TSA-seq 2.0. To compensate for the reduced labelling due to quenching by
353 DTT, we increased the tyramide-biotin concentration by 10-fold.

354 Both in HCT116 (Fig. 5A-B) and U2OS cells (SFig. 5A-B), DDX39B and THRAP3
355 TSA-seq peak and valley patterns qualitatively roughly parallel the SON TSA-seq peak
356 and valley pattern. Quantitatively, however, there are informative differences. We
357 interpret DDX39B and THRAP3 TSA-seq peaks as corresponding to genomic regions
358 that associate closest to foci of DDX39B and THRAP3 staining. The highest amplitude
359 DDX39B and THRAP3 peaks do align with the largest, Type I SON TSA-seq peaks
360 (yellow highlights, Fig. 5A, SFig. 5A). However, we interpret the disproportionally higher
361 amplitude of DDX39B and THRAP3 relative to smaller SON TSA-seq peaks as
362 evidence for the association of these genomic regions near foci of DDX39B and
363 THRAP3 when they are not located near NS. For example, DDX39B and THRAP3
364 TSA-seq peak amplitudes are nearly the same over Type I SON TSA-seq peaks that
365 vary two-fold in SON TSA-seq amplitudes (yellow highlights, Fig. 5A, SFig. 5A). As
366 hypothesized, Type II SON TSA-seq peaks with near-zero SON TSA-seq amplitudes
367 show disproportionally larger DDX39B and, especially, THRAP3 TSA-seq peak
368 amplitudes (blue highlights, Fig. 5A, SFig. 5A) that in some cases approach similar
369 THRAP3 peak amplitudes as observed over Type I peaks (yellow highlights, Fig. 5A,
370 SFig 5A). This disproportionate scaling extends more generally over larger regions of
371 the genome as appreciated in scatterplots of DDX39B or THRAP3 versus SON TSA-
372 seq which show a lower slope for higher versus lower values of SON TSA-seq (Fig. 5B).
373 Finally, DDX39B and THRAP3 peaks are significantly broader and more rounded
374 than their corresponding SON TSA-seq peaks, and they extend over most of the iLADs
375 in which they are embedded, in contrast to the narrower SON TSA-seq peaks. This
376 trend is somewhat more pronounced in the THRAP3 versus DDX39B TSA-seq.

377 We interpret this broader shape of DDX39B and THRAP3 TSA-seq peaks relative to
378 SON TSA-seq peaks as due to the extent to which DDX39B and THRAP3 networks
379 extend throughout the nuclear interior such that iLAD regions are never that distant from
380 the nearest DDX39B or THRAP3 foci. The even broader shape of the THRAP3 versus
381 DDX39B TSA-seq peaks would then be consistent with the greater extent to which the
382 THRAP3 network spreads throughout the nuclear interior relative to the DDX39B
383 network.
384

385 **FISH validation of close association of gene expression hot-zones with PSTP and**
386 **PSDP**

387 To test these TSA-seq interpretations, we first selected 7 large SON TSA-seq
388 Type I peaks and 8 Type II SON TSA-seq local maxima (small peaks or "peak-within-
389 valleys") for immuno-FISH validation in both HCT116 (Fig. 5C) and U2OS (SFig. 5C)
390 cells. We used pooled oligonucleotide probes that targeted simultaneously either all 7
391 Type I peaks or all 8 Type II SON TSA-seq peaks (Supplementary Table 1). To
392 determine distances to the nearest NS, defined by SON staining, or to the nearest
393 DDX39B or THRAP3 foci, we used a local segmentation of the immunostaining based
394 on an intensity threshold corresponding to 50% of the peak intensity of the nearest
395 staining focus (see Methods).

396 As expected, the aggregated Type I SON TSA-seq peaks localized near NS (Fig.
397 5C-D, SFig. 5C-D), with median distances of 0.20 (HCT116) and <0.20 (U2OS) μm from
398 NS. The aggregated Type II peaks instead localized at varying distances from NS, with
399 median distances of 0.74 (HCT116) and 0.54 (U2OS) μm. In contrast, in both HCT116

400 and U2OS cells Type I and II SON TSA-seq peaks positioned close to THRAP3 or
401 DDX39B foci, with median distances of ≤ 0.25 μm, including alleles that are positioned
402 away from NS (Fig. 5B-G, SFig. 5C-G).

403 We next used DNA FISH in U2OS cells to paint chromosome “trajectories” from
404 the nearest LAD/iLAD boundary to either the apex of a SON TSA-seq Type I peak or to
405 the apex of a SON TSA-seq Type II peak (Fig. 6). In both cases, we used
406 oligonucleotide libraries designed to target 7-9 ~100 kb regions spaced approximately
407 evenly along these trajectories.

408 In most cells (~70-90%), both chromosome trajectories showed multiple,
409 individual DNA FISH spots corresponding to the iLAD regions flanking the TSA-seq
410 peak locations, consistent with a partly to more fully extended iLAD chromosome
411 trajectory (Fig. 6). In some cells (~10-30%), however, these FISH spots merged into a
412 single, compact signal, larger than the wide-field diffraction limit, suggesting a more
413 localized folding of the iLAD trajectory (Fig. 6). Interestingly, a high fraction of the
414 extended trajectories aligned relative to the THRAP3 (40-51%) and, especially, the
415 DDX39B staining foci (55-73%) (Fig. 6).

416 The arms of both extended and compact trajectories appeared nearly always
417 (~70-90%) as close or further from the nearest SON, THRAP3, or DDX39B foci than the
418 DNA FISH spot corresponding to the apex of the TSA-seq peak location ("Apex") (Fig.
419 6).

420 To compare quantitatively the association of different trajectory regions with the
421 perispeckle patterns and NS, we segmented and divided the DNA-FISH arm signal into
422 three parts based on their proximity to the Apex: 1) "Arm-close" region (pixels with

423 distances ≤25th percentile closest to Apex); 2) "Arm-center" region (pixels with distances
424 within the 26th-75th percentile from Apex); and 3) "Arm-far" region (pixels with distances
425 >75th percentile from Apex). Then for the Apex and each of these three arm regions, we
426 calculated the shortest Euclidian distance of the center of mass to the nearest
427 segmented NS or protein foci edge. (Note that the nearest NS or protein foci edge could
428 be different for the Apex and each of these three regions; see Methods.)
429 For the Type I trajectory, the Apex was closer to SON, THRAP3 or DDX39B foci
430 compared to Arm regions (Fig. 6A, left lower panel). Moreover, the "Arm-close", "Arm-
431 center", and "Arm-far" regions showed a progressive increase in distances relative to
432 the nearest NS or protein foci edge, respectively. As predicted from the rounded shape
433 of the DDX39B and THRAP3 TSA-seq Type II peaks, the entire Type II iLAD
434 chromosome trajectory typically lies within several hundred nm of some part of the
435 DDX39B and THRAP3 network (Fig. 6B). Distances of the Apex of the Type II peak
436 from the nearest NS edge as expected were larger than for the Type I peak (~0.4
437 versus <0.2 μm). The Type II Apex compared to the Arm-far region was significantly
438 closer to the THRAP3 foci (Fig. 6B, lower left panel). However, the distances to the
439 edge of the nearest DDX39B foci were similar for the Apex and all three arm regions
440 (Fig. 6B, lower left panel), which might reflect the apparent higher alignment of the Type
441 II overall trajectory with the DDX39B network noted previously.
442 In summary, these results confirm that the chromosome gene expression hot-
443 zones corresponding to SON TSA-seq local maxima associate close to DDX39B and
444 THRAP3 foci, even when they are positioned at a distance from NS.
445

446 **Interactions of specific RNAs with PSTP and PSDP**

447 NS were first proposed to act as gene expression hubs not only because a
448 subset of active genes closely associated with the NS periphery but also because a
449 subset of the RNAs transcribed from these genes, for example from the *COL1A1* and
450 *actin* genes, specifically entered and concentrated within the adjacent NS (Hall et al.,
451 2006). We later described how HSPA1A RNA also entered and concentrated within NS
452 (Hu et al., 2009). As reviewed elsewhere, the trafficking of a large number of specific
453 RNAs through NS has now been suggested using genome-wide sequencing-based
454 methods (Wu et al., 2024; Barutcu et al., 2022; Khyzha et al., 2025). Most NS-enriched
455 factors are involved in some aspect of RNA processing and/or export, and the idea of
456 NS acting as a gene expression hub has always included the concept that proximity of
457 genes and RNAs to NS might increase overall gene expression levels largely through
458 their acceleration of post-transcriptional RNA processing and export events (Smith et
459 al., 2020; Bhat et al., 2024; Barutcu et al., 2022; Wu et al., 2024; Wang et al., 2018).

460 The marker proteins for PSTP and PSDP that we identified here have similarly
461 been functionally tied to various aspects of RNA processing, stability, and export.
462 Therefore, using two experimental systems we decided to explore whether PSTP and/or
463 PSDP networks might not only be associated with specific chromosome regions but
464 also with specific pre-mRNAs and mRNAs, similarly to NS. Because Type I versus Type
465 II chromosome regions are enriched in genes with low versus high intron-content,
466 respectively (Gholamalamdari et al., 2025), we specifically compared the localization of
467 RNAs from intronless versus intron-containing genes.

468 First, we used two cell lines, described elsewhere (Mor et al., 2010; Brody et al.,
469 2011), carrying different stably integrated, multi-copy transgene arrays. Because these
470 transgene arrays express at high levels, they produce large numbers of RNPs whose
471 locations can be mapped relative to NS and perispeckle patterns with high statistical
472 power within individual nuclei. The “E6” cell line contains a synthetic transgene with β-
473 globin derived sequences including 6 exons and 5 introns, whereas the “Mini-
474 dystrophin” cell line ("mini-Dys") contains a truncated dystrophin transgene with a single
475 exon and no introns. Both transgene RNAs contain 24 MS2 repeats and both cell lines
476 express the MS2 coat protein (MCP) tagged with YFP that binds to this MS2 RNA
477 repeat. Because of the hundreds of transcripts per nucleus, we used an automated
478 image processing pipeline that segments the SON, DDX39B or THRAP3 intensities,
479 using Otsu global thresholding, and then computes the distance of the center of each
480 detected RNP to the nearest segmented staining feature (see Methods).
481 As our second experimental system, we used HSPA1 and HSPH1 endogenous
482 genes, thereby allowing us to complement our results using the transgene arrays.
483 Unlike most endogenous genes, HSPA1 and HSPH1 genes produce a high number of
484 transcripts. We chose times after heat shock (HS) producing high numbers of HSPA1
485 and HSPH1 transcripts per nucleus, allowing us to avoid the use of transgenes while
486 still acquiring measurements for ~10-20 RNPs per nucleus away from the site of
487 transcription. Whereas the highly homologous *HSPA1A* and *HSPA1B* genes expressed
488 from the HSPA1 locus (situated within a SON Type I peak) produce short transcripts
489 less than 1kb with no introns, the 27 kb *HSPH1* gene (resident within a SON Type II
490 peak) contains 17 introns. The smaller number of transcripts per nucleus of these heat

491 shock genes allowed us to use a semi-automated local intensity thresholding and
492 measure distance of each RNP to the nearest staining foci by an automated algorithm
493 (see Methods). This local thresholding allows detection of lower intensity staining foci
494 which are missed by global thresholding approaches. The short length of HSPA1 genes
495 results in significantly faster induction after HS as compared to the much longer HSPH1
496 gene. We chose different times after HS- 30 mins for HSPA1 and 60 mins for HSPH1,
497 which maximized the number of nuclear RNPs present in the nucleus away from their
498 transcription site for each gene.

499 In both experimental systems, the intron-rich E6 and HSPH1 RNAs localized very
500 close to THRAP3 foci in absolute distances (0.12 and 0.03 μm mean and median (E6);
501 0.13 and 0.07 μm mean and median (HSPH1)) and closer than the localization to
502 THRAP3 foci of the intronless mini-dystrophin and HSPA1 RNAs (0.30 and 0.23 μm
503 mean and median (mini-dystrophin); 0.34 and 0.30 μm mean and median (HSPA1))
504 (Fig. 7A-B,E&G, I-J). However, both intron-rich and intronless transcripts showed very
505 close and similar distances to the nearest DDX39B foci (0.10 and 0.04 μm mean and
506 median (E6); 0.17 and 0.06 μm mean and median (HSPH1); 0.11 and 0.05 μm mean
507 and median (mini-dystrophin); 0.15 and 0.06 μm mean and median (HSPA1)) (Fig. 7C-
508 D, F&H, I-J). These distances to the nearest DDX39B and THRAP3 foci for all these
509 transcripts are significantly lower than their distances to NS (SON and SRRM2); this
510 indicates that a significant fraction of the transcripts associate with DDX39B and
511 THRAP3 foci away from NS.

512 Overall, these results from both transgene arrays and endogenous genes
513 indicate that the transcripts from intron-containing genes preferentially associate with

514 PSTP within the interchromatin space while transcripts from both intron-containing and
515 intronless genes show close association with PSDP.
516
517 **THRAP3 and DDX39B networks are largely maintained after NS knockdown**
518 We next asked whether the maintenance of PSTP and PSDP networks depends
519 on NS. One possibility is that NS nucleate these PSTP and PSDP networks and
520 therefore these perispeckle networks would require NS for maintenance. Alternatively,
521 these perispeckle networks might be maintained independently of NS, possibly even
522 with NS then preferentially nucleating within regions of high local PSDP protein
523 concentrations.
524 Previous work had concluded that SON and SRRM2 are core NS proteins and
525 essential for NS formation (Ilik et al., 2020). We used simultaneous degradation of both
526 SON and SRRM2 using an improved auxin-inducible degron (AID2) system (Fig. 8A,
527 SFig. 8A) (Yesbolatova et al., 2020). Both endogenous alleles of SON and SRRM2 in
528 HCT116 cells were modified with degron tags and mClover and mCherry fluorescent
529 tags, respectively. Fixed and live-cell microscopy both show NS, identified by SON and
530 SRRM2 concentrations, shrinking and then in most cases disappearing within 0-4 hours
531 of analog 5-Ph-IAA treatment (Fig. 8B-C, SFig. 8B). Live-cell imaging reveals NS initially
532 shrinking, while maintaining elevated concentrations of SON during this shrinkage (Fig.
533 8B, 20-40 mins), consistent with SON existing as a condensate within NS.
534 Immunostaining of DDX39B and THRAP3 shows similar staining networks both
535 before and after NS depletion (Fig. 8C). We used transfection to express a HaloTag-
536 DDX39B construct and performed live-cell imaging after two weeks of drug selection.

537 The cells were imaged 20-25 minutes after adding 5-Ph-IAA-containing media. These
538 live-cell movies reveal a ~20% reduction of DDX39B intensity within the regions
539 formerly occupied by NS after SON and SRRM2 double knockdown (DKD); a
540 concomitant increase in DDX39B intensities is seen in the network staining outside of
541 the regions formerly occupied by NS (Fig. 8B).

542 At later time points (>45 mins), NS SON levels drop to just a few percent of their
543 value at 20 mins (Fig. 8B), while DDX39B levels within the same NS decrease by only
544 ~25%. Importantly, the overall nuclear DDX39B intranuclear distribution is largely
545 maintained, including the DDX39B concentrations over regions previously occupied by
546 SON in NS.

547 The previous conclusion that SON and SRRM2 are required for NS nucleation
548 and maintenance was based on the dispersion of several other NS markers throughout
549 the nucleus after simultaneous SON and SRRM2 DKD using siRNA (Ilik et al., 2020;
550 Zhang et al., 2024). An alternative explanation, however, could be that SON and
551 SRRM2 are required only for recruitment of this subset of NS components but not for
552 NS nucleation and maintenance per se. Our observation of an initial shrinking of the NS
553 after SON and SRRM DKD using AID2 (Fig. 8A, B), simultaneous with retention of
554 elevated SON and SRRM2 concentrations within these shrinking NS, is consistent with
555 the shrinkage and then disappearance of an actual condensate dependent on SON and
556 SRRM2, thus supporting a primary role of SON and SRRM2 in nucleating and
557 maintaining NS.

558 NS have been operationally defined as the light microscopy equivalent of the
559 Interchromatin Granule Clusters (IGCs) first identified by electron microscopy; these

560 granules were demonstrated by immunostaining to contain RNA (reviewed in (Chen and
561 Belmont, 2019)). At the light microscopy level, NS were also operationally defined by
562 their local concentration of polyadenylated RNAs (Carter et al., 1991, 1993).
563 We therefore next examined the distribution of polyA-RNA after SON and
564 SRRM2 acute DKD using RNA FISH. Indeed, we observed the dispersion of locally
565 concentrated polyA-RNA "islands" after SON and SRRM2 DKD (Fig. 8D).
566 We therefore conclude first that NS are indeed depleted after SON and SRRM2
567 DKD and second that the DDX39B and THRAP3 perispeckle networks are largely
568 maintained after NS depletion.
569
570 **Nuclear genome positioning relative to PSTP and PSDP is largely maintained**
571 **independent of NS**
572 Given the general alignment of THRAP3 and DDX39B with SON TSA-seq
573 signals, plus the maintenance of PSTP and PSDP after NS elimination, we next asked
574 whether chromosome positioning relative to PSTP and/or PSDP was dependent on
575 maintenance of NS. We performed DDX39B and THRAP3 TSA-seq after 4 hours of 5-
576 Ph-IAA induced SON and SRRM2 DKD, the earliest time point we had sampled
577 showing maximum KD of both SON and SRRM2 expression (Fig. 8A). We observed
578 little change in chromosome positioning relative to PSTP and PSDP after this several
579 hour loss of SON and SRRM2 and NS, including over gene expression hot-zone
580 chromosome regions corresponding to both Type I and II SON TSA-seq peaks (Fig. 8E,
581 SFig. 8B-E).

582 Overall, both the THRAP3 and DDX39B TSA-seq reveal little change after NS
583 elimination. Quantitative comparisons show a slight, largely statistically insignificant
584 increase in DDX39B TSA-seq values after NS elimination (SFig. 8B). Conversely,
585 THRAP3 TSA-seq shows a small overall decrease in signal after NS elimination, which
586 does score as statistically significant (SFig. 8C); this small change in THRAP3 TSA-seq
587 scores appears to reflect a systematic variation in scaling across the genome after SON
588 and SRRM2 DKD. Specifically, THRAP3 TSA-seq peaks are decreased in amplitude
589 slightly while valleys are deepened slightly. The reasons for these subtle genome-wide
590 changes in DDX39B and THRAP3 TSA-seq score amplitudes remain unclear but may
591 be related to small shifts in DDX39B and THRAP3 intranuclear distribution after NS KD.
592 Despite these small changes in scaling of the DDX39B and THRAP3 TSA-seq
593 signals, we do not see any significant or specific changes in the overall patterns of
594 peaks corresponding to NS and perispeckle pattern associated domains (Fig.8E,
595 SFig.8B-E).
596 Finally, we asked how genes differentially positioned relative to NS might change
597 their expression as a function of SON and SRRM2 DKD. SON depletion is known to
598 arrest cell growth through perturbation of the cell cycle, particularly during mitosis
599 (Sharma et al., 2010; Ahn et al., 2011). To minimize changes in gene expression due to
600 changes in cell cycle progression, we combined an extended 16 hr DKD of SON and
601 SRRM2 with a cell-cycle arrest in late G1/early S-phase. We applied the DKD in cells
602 as they progressed from G1-arrest into a late G1/early S phase block (see Methods).
603 RNA-seq analysis revealed that NS-proximal genes within +/- 500 kb of Type I
604 SON TSA-seq peaks showed a systematic bias towards decreased gene expression

605 after SON and SRRM2 DKD (Fig. 8F-H; Supplementary Table 2). In contrast, genes
606 within +/- 500 kb of Type II SON TSA-seq peaks, showed no strong bias towards
607 decreased versus increased differential gene expression after SON and SRRM2 DKD
608 (Fig. 8F-H; Supplementary Table 2). We note that the SON TSA-seq peak-calling used
609 Hi-C subcompartment identity to classify Type I versus Type II peaks, which caused
610 some degree of misclassification of SON TSA-seq positive peaks (Type I) versus "peak-
611 within-valley" SON TSA-seq local maxima (Type II). Instead, defining Type II peaks as
612 those with SON TSA-seq scores ≤ 0.0 (Fig. 8G, dashed line), we observe a more
613 pronounced ~2-fold bias of increased (123 genes) versus decreased (62 genes)
614 differentially expressed genes within Type II peaks after NS KD (Fig. 8G, left of dashed
615 vertical line).
616 Thus, we conclude that chromosome positioning relative to PSTP and PSDP
617 networks, including regions originally near NS defined by SON TSA-seq peaks, remain
618 unchanged for at least several hours after NS elimination. This observation raises the
619 possibility that the perispeckle patterns might maintain genome organization
620 independent of the NS defined by SON and SRRM2. Despite this maintenance of
621 genome organization of Type I and II gene expression hot-zones, genes in Type I hot-
622 zones do appear dependent on NS to sustain their normal levels of gene expression.
623
624

625 **Discussion**

626 **Summary**

627 We set out to resolve an apparent paradox. On the one hand, live-cell imaging
628 (Kim et al., 2020) and RNA FISH (Zhang et al., 2021; Alexander et al., 2021) both
629 suggested actual contact with NS was required for gene expression amplification. On
630 the other hand, a strong correlation was observed genome-wide between changes in
631 gene expression and positioning of these genes relative to nuclear speckles, even when
632 these changes in positioning did not involve changes in actual nuclear speckle close
633 association (Zhang et al., 2021; Gholamalamdari et al., 2025). To reconcile these two
634 distinct observations, we hypothesized the existence of a previously unidentified gene
635 expression hub(s) that was itself spatially correlated with but distinct from NS.

636 Here we describe the identification of two perispeckle patterns, characterized by
637 the concentrations of specific proteins, which are both tightly spatially correlated with
638 NS (Fig. 9). PSTP components surround NS, defined by SON and SRRM2
639 immunostaining, and in some cases may colocalize but not concentrate within NS, while
640 PSDP components concentrate within NS. More importantly, both extend outwards and
641 throughout the nuclear, DNA-depleted interior in thread-like patterns from NS. Together
642 PSTP and PSDP subdivide the ICS. Meanwhile, other proteins that concentrate within
643 the ICS overlap with neither PSTP nor PSDP, suggesting that these two perispeckle
644 patterns together still occupy only a fraction of the total ICS; this would leave substantial
645 additional space which other condensates might occupy.

646 PSTP and PSDP appear to represent an alternate gene expression hub in the
647 sense that a large fraction of the chromosomal regions with high gene expression levels

648 not localized near NS are instead localized very close to the thread-like patterns of
649 PSTP and PSDP. Similarly to nuclear speckles, PSTP and PSDP contain a mixture of
650 components involved in various steps of gene expression, especially RNA splicing and
651 export. Additionally, we show the preferential association of RNAs from two model
652 intron-containing genes with PSTP as compared to the RNAs from two model intron-
653 less genes. In contrast, the RNAs from both intron-containing and intronless genes are
654 closely associated with PSDP. Thus, we speculate that the PSTP and PSDP
655 perispeckle networks may additionally facilitate a spatial coupling between the
656 machinery of transcription and RNA processing and export for a subset of active genes
657 and their transcripts (Fig. 9).
658
659 **Possible resolution of our paradox**
660 We propose that the close association of highly active chromosomal regions not
661 near NS with these perispeckle patterns may resolve the apparent paradox between our
662 previous live-cell imaging and genomic analysis of the relationship of active genes
663 relative to NS. Because of the close spatial arrangement of PSTP and PSDP relative to
664 NS, repositioning of chromosomal regions with gene activation to bring them into
665 contact with these perispeckle patterns (Fig. 9, right panel) will also bring these active
666 chromosomal regions closer to NS on average over the cell population. Most RNA Pol II
667 Ser2p and Ser5p foci localize within several hundred nm of PSDP and, especially,
668 PSTP foci, even those positioned away from NS. Similarly, chromosomal gene
669 expression hot-zones, identified as Type I and Type II SON TSA-seq peaks, localize
670 within several hundred nm of PSTP and PSDP foci. This is true even when positioned

671 away from NS, as is the case for the majority of alleles of Type II SON TSA-seq peak
672 regions. Moreover, as predicted in our original model (Fig. 1A), we showed that a
673 chromosome gene expression hot-zone corresponding to a Type II SON TSA-seq was
674 the closest chromosome region to a PSTP or PSDP foci over the entire chromosome
675 iLAD trajectory stretching from the nearest LAD to this Type II SON TSA-seq peak.
676

677 **Perispeckle patterns are dynamic networks rather than stable nuclear bodies**

678 In our original hypothesis, we had envisioned Type II SON TSA-seq peaks as
679 interacting with an alternative nuclear body/compartment of comparable stability to NS.
680 Instead, we observe both PSTP and PSDP networks away from NS to be highly
681 dynamic over a time period of seconds to tens of seconds, even though we see their
682 repeated recurrence in similar spatial patterns on a time scale of minutes such that
683 time-averaging reveals a more definite network pattern. In a companion paper, we
684 more thoroughly examine dynamics of PSDP components DDX39B and MAGOH and
685 show that their preferential concentration into stable time-averaged patterns disappears
686 with ATP-depletion and at least partially with transcriptional inhibition (Kim et al., 2025).
687 We also show directional, bulk transfer of SON condensates between NS within PSDB
688 network connections (Kim et al., 2025).
689

690 **Relationship of DDX39B perispeckle pattern to NS**

691 Despite the close spatial relationship of PSTP and PSDP to NS, both THRAP3
692 and DDX39B distributions are largely maintained after NS disruption. SON and SRRM2
693 were considered to be required for NS integrity because their double KD (DKD) led to

694 dispersal of several other known NS proteins (Ilik et al., 2020). DDX39B, and possibly
695 other PSDP components, retain the same high concentrations within bodies that
696 originally colocalized with NS even after SON and SRRM2 KD that is reported to
697 eliminate NS (Ilik et al., 2020). Should these high-concentration DDX39B bodies then
698 be considered as NS that persist after SON and SRRM2 DKD with SON and SRRM2
699 necessary only for retention of a subset of NS proteins?

700 NS were described originally as clusters of RNPs and foci of polyA accumulation.
701 From this functional view of NS as concentrators of RNPs, we therefore suggest that the
702 observed loss of NS- associated poly-A RNA accumulations after SON and SRRM2
703 DKD means NS are indeed eliminated after SON and SRRM2 KD. Just as nucleolar
704 GC proteins such as nucleolin can mix with the FC (Lafontaine et al., 2021), we suggest
705 PSDP components have the ability to mix with NS components. Similar to how the
706 dense fibrillar component and fibrillar centers (FC) form within the granular
707 compartment (GC) of nucleoli, we suggest that NS form within accumulations of PSDP
708 components

709 A second question is whether gene positioning is controlled not by NS per se but
710 by PSDP, given that gene positioning is largely maintained for at least several hours
711 after NS disruption, and what functions NS may impart separate from PSDP. The
712 observation of gene expression amplification with NS contact (Kim et al., 2020;
713 Alexander et al., 2021; Chaturvedi and Belmont, 2024), plus the observed reduced
714 expression specifically of a subset of genes positioned very close to NS after SON and
715 SRRM2 KD, suggests that NS are indeed required for the increased expression of a
716 subset of NS proximal genes.

717 **Connections of perispeckle patterns to RNA processing and trafficking**

718 Similar to NS, which are enriched especially for proteins related to multiple levels
719 of RNA processing, modification, and export, the perispeckle pattern marker proteins we
720 identified here are all related to RNA splicing and export. Our demonstration of close
721 association of RNA with these two perispeckle patterns raises the interesting possibility
722 that these perispeckle patterns might be pathways for mRNAs moving away from the
723 gene and trafficking through the nucleus.

724 Among the PSTP marker proteins, THRAP3 (TRAP150) was described as a
725 member of the TRAP/Mediator complex (Ito et al., 1999) but also associates with mRNA
726 export factor TAP (Lee et al., 2010) and has been shown to play roles in pre-mRNA
727 splicing (Lee et al., 2010; Lee and Tarn, 2014; Vohhodina et al., 2017), mRNA
728 degradation (Lee et al., 2010), and R-loop resolution (Kang et al., 2021). BCLAF1 has
729 known roles in pre-mRNA splicing (Vohhodina et al., 2017), nuclear retention of RNAs
730 (Varia et al., 2013) and as a transcriptional repressor (Shang et al., 2022) . PLRG1 is a
731 component of the cell division cycle 4-like (CDC5L) complex which is part of the
732 spliceosome (Ajuh, 2000) and is involved with alternative splice-site selection (Llères et
733 al., 2010), as well as DNA repair (Zhang et al., 2005) and the ATR-response (Zhang et
734 al., 2009). During development, PLRG1 regulates proliferation and apoptosis
735 (Kleinridders et al., 2009). Interestingly, we observed the mRNAs from intron-rich
736 genes, but not intronless genes, associating closely with PSTP.

737 Among the PSDP marker proteins, DDX39B is a DEAD-box RNA helicase
738 already known to regulate release of spliced mRNAs from NS (Hondele et al., 2019;
739 Taniguchi and Ohno, 2008; Luo et al., 2001; Fan et al., 2018). DDX39B is also

740 essential for R-loop resolution (Pérez-Calero et al., 2020) and is a member of the TREX
741 export complex (Dias et al., 2010; Wang et al., 2018; Shen et al., 2008). RBM8A (Y14)
742 and MAGOH are both members of the core Exon Junction Complex (EJC) that
743 assembles on pre-mRNAs over the junction of two exons that are spliced together (Le
744 Hir, et al. 2000) and provides binding platform for additional factors involved in mRNA
745 export and nonsense-mediated decay (NMD) (Le Hir, Hervé, et al. 2001).
746 Interestingly, DDX39B previously was suggested to regulate the entry and
747 release of RNAs from phase-separated condensates in an ATP-dependent manner
748 (Hondele et al., 2019). Immunogold EM against DDX39B coupled to EDTA-regressive
749 staining showed DDX39B associating at the periphery of IGCs and thread-like, likely
750 RNA-containing projections extending from IGCs into the interchromatin space (Kota et
751 al., 2008). DDX39B is evolutionarily-conserved and is essential for the export of spliced
752 RNA and intronless RNA (Jensen et al., 2001; Gatfield et al., 2001; Kota et al., 2008;
753 Dias et al., 2010; Wang et al., 2018). Higher-order assembly of export-competent
754 mRNPs is also mediated by DDX39B (Xie et al., 2023). Cosistent with a role of DDX39B
755 in nuclear RNA export, we observed mRNAs from both intron-rich and intron-less genes
756 associating closely with PSDP.
757 All together, these observations raise the hypothesis of RNPs being moved
758 sequentially through different spatially organized “processing” condensates before and
759 during export out of the nucleus.
760
761 **Future Directions**

762 Our description of perispeckle patterns suggest multiple avenues for future
763 investigation. Of central interest will be going beyond correlation to test causality
764 between chromosomal and RNA association with PSTP and PSDP networks with
765 modulation of gene expression, including RNA export. Future live-cell imaging will be
766 valuable to test the temporal correlation between contact with PSTP and/or PSDP and
767 changes in gene expression and/or RNA movements as well as monitoring changes in
768 gene expression after acute knockdown of PSTP and PSDP components. Beyond
769 gene expression, we anticipate future investigations into the possible role of perispeckle
770 patterns in DNA repair and genome stability given that multiple PSTP and PSDP
771 components have been implicated in both R-loop resolution (THRAP3, DDX39B,
772 POLDIP3) (Kang et al., 2021; Pérez-Calero et al., 2020; Björkman et al., 2020) and
773 DNA repair and genome stability (THRAP3, BCLAF1, RBM8A, DDX39B, PLRG1)
774 (Vohhodina et al., 2017; Yu et al., 2023a; Chuang et al., 2019; Xu et al., 2020; Choi et
775 al., 2023).
776 Two additional functions of perispeckle patterns are suggested by our work and
777 others. First, a role of PSDP in bulk trafficking of NS components is suggested by a
778 companion study. Using live-cell imaging, we demonstrated the directional bulk transfer
779 of SON protein as small condensates between NS in ATP-dependent "connections"
780 marked by dynamic DDX39B, MAGOH, and SON multi-phase protein concentrations
781 whose interactions form a more stable unit that any of the individual components (Kim
782 et al., 2025). Second, perispeckle patterns may play a role in genome stability, as
783 multiple components of both PSTP and PSDP have been implicated in both R-loop
784 resolution (THRAP3, DDX39B, POLDIP3) (Kang et al., 2021; Pérez-Calero et al., 2020;

785 Björkman et al., 2020) and DNA repair and genome stability (THRAP3, BCLAF1,
786 RBM8A, DDX39B, PLRG1) (Vohhodina et al., 2017; Yu et al., 2023a; Chuang et al.,
787 2019; Xu et al., 2020; Choi et al., 2023).
788 Finally, although we focused here on PSTP and PSDP, our initial screening
789 suggested that there will be additional perispeckle patterns/ protein condensates that
790 further subdivide the interchromatin space. We therefore suggest additional
791 investigations will be needed to fully appreciate the integration of these dynamic protein
792 condensates with each other and with important nuclear functions.
793
794

795 **Methods:**

796 **Cell lines and cell culture**

797 U2OS and HCT116 cells were obtained through the ATCC, expanded through
798 pyramid stocking, and maintained as per the 4D Nucleome SOP
799 (https://data.4dnucleome.org/resources/experimental-resources/cell-lines). U2OS cell
800 lines containing E6 β-globin and mini-Dystrophin A1 transgenes were described
801 previously (Mor et al., 2010; Brody et al., 2011).

802 All cells were grown at 37°C in a humidified incubator with 5% CO_2. Specifically,
803 both U2OS and HCT116 cells were cultured in McCoy's 5A medium (UIUC cell media
804 facility) supplemented with 10% fetal bovine serum (FBS) (VWR, cat# 97068-091, Lot
805 #035B15). Cells were passaged (or harvested) at 70%-80% confluency using Trypsin-
806 EDTA (0.05%) (Thermo Fisher Scientific, cat# 25300062).

807 U2OS cell lines with the E6 β-globin and mini-Dystrophin transgenes were
808 cultured in low glucose containing DMEM (UIUC cell media facility). The E6 β-globin cell
809 line was maintained with 10 μg/ml Puromycin (Puromycin Dihydrochloride, Gibco, cat#
810 A1113803) and 0.54 mg/ml Zeocin (Gibco, cat# R25001). The mini-dystrophin A1 cell
811 line was cultured with 50 μg/ml Hygromycin (Gibco, cat#10687010) and 0.54 mg/ml
812 Zeocin (Gibco, cat# R25001). Cells were passaged using Trypsin-EDTA (0.05%)
813 (Thermo Fisher Scientific, cat# 25300062).

814 For all cell lines, cells were cultured for a maximum of 10-12 passages after
815 thawing.

816

817 **cDNA Constructs and screening**

818 For the screening of selected protein candidates, PCR amplicons were prepared
819 from cDNA. For genes with multiple transcript variants, the longest protein-coding
820 transcript sequence was chosen for PCR amplification and cloned into pEGFP-C1
821 vector as described previously (Dopie et al., 2020). Briefly, total RNA was isolated using
822 the RNeasy kit (Qiagen, cat#74104) and 1μg total RNA was reverse transcribed using
823 the Protoscript First Strand cDNA Synthesis Kit (New England Biolabs, cat# M0368S) to
824 generate cDNA. Using primers containing the appropriate restriction enzyme sites
825 (Supplementary Table 1), cDNA amplicons were PCR amplified with Q5 High-Fidelity
826 DNA Polymerase (New England Biolabs, cat# M0491S), purified and cloned into
827 pEGFP-C1 (originally obtained from Clonetech). The sequences of all plasmids
828 generated were validated by Sanger sequencing before their use.
829 For transfections, ~120,000 U2OS cells were seeded per well in a 6-well plate
830 containing 12mm diameter #1.5 coverslips (Electron Microscopy Sciences, cat#72230-
831 01) and the next day, 500 ng of plasmid was transfected using 5ul Lipofectamine 2000
832 (Thermo Fisher Scientific, cat#11668019) in OptiMEM (Thermo Fisher Scientific, cat#
833 31985070) as per the manufacturer's instructions. After 24 hours, cells were fixed with
834 freshly prepared 4% paraformaldehyde (Sigma, cat#P6148) in calcium and magnesium
835 free phosphate buffered saline (CMF-PBS) for 10 mins at room temperature (RT). Cells
836 were washed for 5 mins 3 times with CMF-PBS and then either mounted directly using
837 Mowiol-DABCO antifade mounting medium or processed further.
838
839 **Antibody generation**

840 A rabbit polyclonal anti-DDX39B antibody (Pacific Immunology) was generated
841 against the 24 amino acid synthesized peptide (Cys)-DRFEVNISELPDEIDISSYIEQTR,
842 conserved across human, mouse and Chinese hamster DDX39B protein sequences.
843 Briefly, two rabbits were immunized once with AdjuLiteTM Complete Freund's Adjuvant
844 followed by three rounds of AdjuLiteTM Incomplete Freund's Adjuvant immunizations.
845 The first production bleed was validated by ELISA against the peptide used for
846 immunization. After validation, serum from both rabbits was pooled prior to affinity
847 purification. 25 mL pooled serum was subjected to affinity purification using the same
848 target peptide. This affinity-purified antibody was diluted in 50% glycerol for long-term
849 storage at a concentration of 0.6 mg/ml. The antibody was further validated by
850 demonstrating its colocalization after immunostaining with the mCherry-DDX39B signal
851 in a U2OS cell line with the endogenous DDX39B gene tagged with mCherry (See "Cell
852 Line Construction" Section, below).
853
854 **Immunostaining**
855 Cells were fixed with freshly prepared 4% (w/v) paraformaldehyde solution in
856 CMF-PBS (pH 7.0) (Sigma-Aldrich, cat# P6148) for 10 mins at RT. Coverslips were
857 washed three times with CMF-PBS and cells were permeabilized with 0.5 % Triton X-
858 100 in CMF-PBS for 10 mins at RT. Washes for 5 mins with CMF-PBS were repeated
859 three times followed by blocking for 1 hr at RT in 5% (v/v) goat serum solution prepared
860 in 0.1 % Triton X-100 in CMF-PBS. Primary antibodies were diluted as stated
861 (Supplemetary Table 1) in blocking buffer and applied to coverslips overnight at 4°C for
862 12-16 hours in a humidified chamber. Coverslips then were washed for 5 mins three

863 times using 0.1 % Triton X-100 in CMF-PBS at RT. Secondary antibodies were diluted
864 as stated (Supplementary Table 1) in blocking buffer and applied to coverslips for 1 hr
865 at RT in a humidified chamber before 5 min washes with 0.1 % Triton X-100 in CMF-
866 PBS repeated three times. Coverslips were mounted using Mowiol-DABCO antifade
867 mounting medium without or with DAPI (Sigma-Aldrich cat#D9542) (10ug/ml).
868

869 **Cell line construction**

870 Knock-in cell lines containing endogenous gene sequences tagged with different
871 fluorescent proteins were constructed using CRISPR/Cas9 as described previously
872 (Gholamalamdari et al., 2025). For gRNA synthesis, a 2-step overlap PCR strategy was
873 employed. In the first step, a forward primer including the T7 promoter sequence
874 followed by the target specific sequence 20bp immediately upstream of the PAM
875 sequence and a reverse primer containing the tracrRNA template sequence (5'-
876 AAAAGCACCGACTCGGTGCCACTTTTTCAAGTTGATAACGGACTAGCCTTATTTTAA
877 CTTGCTATTTCTAGCTCTAAAAC -3') (Supplementary Table 1) were used. This first
878 step generated a 120bp T7-gRNA-tracr fragment. In the second step, we amplified this
879 DNA template using a T7 promoter sequence forward primer (5'-
880 TAATACGACTCACTATAG-3') and a reverse primer sequence (5'-
881 AAAAGCACCGACTCG-3').

882 This DNA template was gel purified (QIAGEN # 28704) and used for an in vitro-
883 transcription reaction to generate gRNA. 1 µg of DNA template was incubated with
884 2.5mM ribonucleotides (NTP, New England Biolabs cat#N0466S), 1U/µl Ribolock
885 RNase inhibitor (Thermo Fisher Scientific, cat# EO0381), 8 µl T7 RNA Polymerase

886 (purified in the laboratory) in 50 µl reaction volume in IVT buffer (50mM Tris-HCl, pH
887 7.6, 15mM magnesium chloride, 5mM dithiothreitol (DTT) and 2mM spermidine). The
888 reaction was incubated at 37°C for 6-16 hours in a thermocycler. In-vitro transcribed
889 product was treated with 2.5 U DNase I (2 U/µl; New England Biolabs cat# M0303S) at
890 37°C for 15 mins to remove the DNA template prior to purification. gRNA was purified
891 using the RNeasy plus kit (QIAGEN cat# 74134). Purified gRNAs eluted in RNase-free
892 water (Accugene cat#51200) were stored as aliquots at -80°C.
893 2 µg of target-specific gRNAs were complexed with 3µg purified Cas9 Nuclease
894 V3 (Integrated DNA Technologies, cat# 1081058). gRNA sequences and primers used
895 for homology arms of Donor DNA sequences are provided in Supplementary Table 1.
896 Primers 70-90 bp long with their 5' end modified with an amine group coupled to a C6
897 linker (Yu et al., 2020) were used for generating donor DNA with homology arms
898 including sequences upstream and downstream of the target genomic DNA cut site;
899 (Supplementary Table 1). PCR amplification of the donor DNA used Q5 High-Fidelity
900 DNA Polymerase (New England Biolabs, cat# M0491S) and was applied to a plasmid or
901 BAC template DNA containing sequences coding for the fluorescent protein and linker
902 peptide to be added to the NH2-terminus of the target protein (Supplementary Table1).
903 This donor DNA was purified after the PCR using magnetic beads (MAGBIO, HighPrep
904 PCR, cat#AC-60050). Nucleofection was performed using an Amaxa Nucleofector II
905 device (Lonza) as per the manufacturer's instructions.
906 After 5 days of recovery, fluorescence-positive cells were sorted using the FACS
907 ARIA II sorter at the UIUC Roy J. Carver Biotechnology Center. Using this approach,
908 the "U2OS EGFP-SON C5" cell clone was first generated. U2OS EGFP SON C5 was

909 then further modified to generate the "U2OS EGFP-SON C5 mCherry-DDX39B C11"
910 cell clone and the "U2OS EGFP-SON C5 mCherry-THRAP3 gRNA#1" mixed clonal cell
911 line. Similarly, a U2OS HaloTag-SON" mixed clonal cell line was generated and then
912 further modified to generate the "U2OS HaloTag-SON EGFP-THRAP3 gRNA#1" mixed
913 clonal cell line (Supplementary Table1).

914 HCT116 SON and SRRM2 double-degron cell line (expressing mAID-Clover-
915 SON and SRRM2-mAID-mCherry) was generated by CRISPR-Cas9-mediated genome
916 editing as previously described (Yesbolatova et al. Nat. Commun., 2020; Saito et al.
917 Current Protocols, 2021). Briefly, we initially fused mAID-mCherry to the C-terminus of
918 SRRM2. For this, we designed a CRISPR-Cas9 plasmid for targeting the SRRM2 locus
919 (5'-AGGTCTCCATAAATTGTCTT(TGG)-3'). A donor plasmid harboring mAID-mCherry
920 and a selection marker (BSD) with two homology arms (approximately 500 bp each)
921 was constructed. HCT116 cells stably expressing OsTIR1(F74G) from the AAVS1 locus
922 were transfected with the CRISPR and donor plasmids. Clones surviving blasticidin
923 selection were screened for biallelic by genomic PCR, and expression of the fusion
924 protein was confirmed by immunoblotting. Subsequently, we fused mAID-Clover to the
925 N-terminus of SON. For this, we designed a CRISPR-Cas9 plasmid for targeting the
926 SON locus (5'-AGAGAACGGAGCGGACGCCA(TGG)-3'). A donor plasmid harboring
927 HygroR-P2A-mAID-mClover with two homology arms was constructed. The SRRM2-
928 mAID-mCherry cells were transfected with the CRISPR and donor plasmids for tagging
929 SON. Clones surviving hygromycin selection were screened for biallelic insertion of the
930 tagging construct by genomic PCR, and expression of the fusion protein was confirmed

931 by immunoblotting. To induce degradation of SON and SRRM2, 5-Ph-IAA was added to
932 the final concentration of 1 μM.
933
934 **Transcriptional inhibition treatment**
935 30,000 U2OS cells were seeded per #1.5 12 mm diameter coverslip (Electron
936 Microscopy Sciences, cat# 72230-01) in a 24-well plate. After two days, cells were
937 treated with 50 μg/ml DRB (Sigma-Aldrich, cat# D1916), 50 μg/ml α-amanitin (Sigma-
938 Aldrich, cat# A2263), or 0.1 μg/ml triptolide (Sigma-Aldrich, cat# T3652) added in
939 McCoy's 5A media for the time indicated and fixed. For heat shock experiments, cells
940 were seeded on #1.5 12 mm coverslips placed within 35mm dishes (Corning, cat#
941 430165) at 120,000 cells per dish. After two days, cells were incubated in a water bath
942 at 42°C after sealing the dishes with parafilm (Parafilm, cat# S25929) for the indicated
943 time and fixed immediately.
944
945 **Tyramide Signal Amplification-sequencing (TSA-seq)**
946 A detailed protocol for TSA-seq is described elsewhere (Zhang et al., 2022). For
947 high-resolution mapping, we combined the use in the original TSA-seq 1.0 procedure
948 (Chen et al., 2018) of both sucrose and Dithiotheitol (DTT) to increase spatial resolution
949 with the higher tyramide concentration and longer TSA reaction time used in the TSA-
950 seq 2.0 protocol, which saturated the protein TSA labeling but increased the DNA
951 tyramide labeling without saturation (Zhang et al., 2021). More specifically, we used a
952 TSA reaction buffer prepared in CMF- PBS with 50% sucrose: 1.5 mM DTT (Millipore
953 Sigma, cat#233155-10GM), and 0.33 mM tyramide-biotin (Apex-Bio, cat# A8011) with a

954 reaction time of 30 mins. By boosting the tyramide concentration beyond previous TSA-
955 seq 2.0 TSA reaction conditions, we compensated for the decreased TSA-labeling
956 caused by the addition of the DTT, while keeping the nucleic acid labeling
957 undersaturated as judged by microscopy as described previously (Zhang et al., 2021).
958 For each TSA-seq sample in U2OS cells, cells were grown in two T-300 flasks
959 (~15 million cells per T-300 flask). For each TSA-seq sample in HCT116 cells, cells
960 were grown in one T-150 flask (~30-40 million cells). For the TSA-seq of the HCT116
961 mAID-Clover-SON SRRM2-mAID-mCherry CMV-OsTIR1(F74G) cell line, cells in T-150
962 flasks were first treated with either DMSO (Avantor # IC0219605590) or 5μM 5-Ph-IAA
963 (Tocris Biosciences #7392) for 4 hours before proceeding to the TSA-seq procedure.
964 All TSA-seq libraries were prepared using 3-10 ng of purified DNA using the
965 TruSeq ChIP Library Preparation Kit (Illumina, cat# IP-202-1012) as per the
966 manufacturer's instructions. Libraries were PCR-amplified for 8 cycles and purified
967 using AMPure XP magnetic beads (Beckman Coulter, cat# A63881). Concentrations of
968 individual libraries were estimated by qPCR and then pooled accordingly. They were
969 then sequenced from one end of the fragments on a NovaSeq X Plus with V1.0
970 sequencing kits. FASTQ files were generated and demultiplexed with the bcl-convert
971 v4.1.7 Conversion Software (Illumina). TSA-seq normalization, scores and identification
972 of changed regions were performed using a previously reported pipeline (Chen et al.,
973 2018; Zhang et al., 2021).
974
975 **Oligolibrary design and probe synthesis**

976 For DNA FISH of TSA-seq peaks, we used an oligolibrary containing ~500 FISH
977 probes targeted to DNA sequences within each ~100 kb targeted peak region
978 (Supplementary Table 1). Oligo probes (Supplementary Table 1) were designed using
979 PAINTSHOP (https://paintshop.io/) as per published recommendations (Beliveau et al.,
980 2012, 2017). Briefly, selected genomic region coordinates were uploaded and advanced
981 probe settings specified as: no repeats allowed, max off-target score 15, max K-mer
982 count 5, Min prob value 0 and probe set optimized to generate ~500-523 probes per
983 100 kb target with "trim" setting for each region. Each probe set was appended with
984 universal outer primers for each TSA-seq peak type, and a unique inner primer set for
985 each 100 kb genomic peak region. The 3' inner and outer primer was followed by the T7
986 promoter sequence.
987 For trajectory mapping, the distances between two consecutive ~100 kb regions
988 were kept at least 200 kb apart between the nearest edges of two neighboring regions.
989 The outer primer was unique for "Apex" and "Arm" regions and each 100 kb genomic
990 region had a unique inner primer set. The 3' inner and outer primer was followed by the
991 T7 promoter sequence. Otherwise, settings for probe selection were kept the same as
992 for the TSA-seq peak probe selection.
993 For RNA-FISH, ~100 probes were selected for MALAT1 RNA. The outer primer
994 was unique for the target. The outer primer was followed by the T7 promoter sequence.
995 Otherwise, settings for probe selection were kept the same as used for the DNA FISH
996 probe selection.
997 The detailed protocol used for probe preparation is described elsewhere
998 (Beliveau et al., 2017). Briefly, probes were amplified using PCR with Q5 High-Fidelity

999 DNA Polymerase for 7-8 cycles, followed by in-vitro transcription using HiScribe T7 High
1000 Yield RNA Synthesis Kit (New England Biolabs cat# E2040S) and reverse-transcription
1001 using Maxima H Minus Reverse Transcriptase (Thermo Fisher Scientific cat# EP0751)
1002 as described previously (Beliveau et al., 2017).

1003 2 μl of reactions were loaded on a urea-TBE gel to check for the desired ~70-
1004 80% incorporation of reverse transcription RT primer (20bp) into the probes (~150 bp).
1005 Probes were purified using Zymo DCC-25 columns as described previously (Beliveau et
1006 al., 2017).

1007 2 μg purified probes were end-labelled using 12U Terminal Deoxynucleotidyl
1008 Transferase (TdT 20U/μl; Thermo Scientific, cat# EP0161) in TdT buffer (Thermo
1009 Scientific, cat# EP0161) with 108μM unlabelled dATP or dTTP and 54μM Biotin-dATP
1010 (Invitrogen #19524016) or Digoxigenin-11-dUTP (Roche #11093088910) respectively in
1011 a 25 μl reaction volume. Reactions were incubated at 37°C for 1hr in a thermocycler.
1012 Probes were purified using the QIAquick Nucleotide Removal kit (QIAGEN, cat# 28306).
1013 Probes were eluted in 100 μL molecular biology grade water (Accugene, cat#51200)
1014 and human Cot-1DNA (Invitrogen #15279011) was added to each probe such that
1015 human Cot-1 DNA was 10x higher than the probe concentration. The resulting probe
1016 solutions were concentrated using a Vacufuge concentrator (Eppendorf) with the
1017 settings for aqueous solutions at 45°C for 45 mins until the probe solutions were
1018 reduced to ~2-5 μl volumes. To these solutions, equal volumes of 100% formamide
1019 (Sigma-Aldrich, cat#F9037) and 2x hybridization buffer (20% w/v dextran sulphate
1020 (Sigma-Aldrich, cat# D8906) in 4x Saline-Sodium Citrate (SSC) buffer) are added such

1021 that the final probe concentrations are 25 ng/μl in hybridization buffer (10% w/v dextran
1022 sulphate in 2X SSC buffer with 50% formamide).
1023
1024 **DNA-FISH**
1025 Cells were fixed and immunostained as described previously (Solovei and
1026 Cremer, 2010). Briefly, cells were immunostained as described above with the
1027 exception of replacing the goat serum with 5% Bovine Serum Albumin (Sigma-Aldrich
1028 cat#A9418) for blocking and post-fixing after the immunostaining using 2%
1029 paraformaldehyde in CMF-PBS buffer. After three 5 min washes with CMF-PBS,
1030 coverslips were incubated with 20% glycerol (Fisher Scientific, cat# BP229-1) in CMF-
1031 PBS for 24 hours. Coverslips underwent 6 rounds of freezing and thawing in 20%
1032 glycerol in PBS with liquid nitrogen immersion followed by three 5 min washes with
1033 CMF-PBS containing 0.1% Triton X-100 (Thermo Fisher Scientific, cat# 28314).
1034 Coverslips were then rinsed with 0.1 N HCl in molecular biology grade water
1035 (Accugene, cat#51200) and incubated in same at RT for 10 mins. Three 5 min washes
1036 with CMF-PBS containing 0.1% Triton X-100 were followed by immersion in 2x SSC
1037 containing 50% formamide at 4°C for at least 3 days and up to 15 days. For
1038 hybridization, oligolibrary probes (100-125ng of labelled oligoprobes in 10% dextran
1039 sulphate in 2X SSC buffer containing 50% formamide and 1μg of unlabelled human Cot-
1040 1 DNA (Invitrogen cat#15279011) were added to a glass slide and the 12 mm circular
1041 #1.5 mm coverslip was inverted and sealed using rubber cement (Elmers).
1042 The slide was placed on a heating block at 75°C for 3 mins and then immediately
1043 moved to a humidified chamber at 37°C for 4 days of hybridization. Post-hybridization,

1044 coverslips were removed from the slide and washed for 10 mins three times with 2x
1045 SSC at 37°C followed by two 5 min washes with 0.1x SSC at 60°C.
1046 Probes were detected using anti-Digoxin antibody (Jackson #200-602-156) or
1047 Streptavidin (Jackson #016-600-084) conjugated to Alexa 647 diluted 1:200 in 4% BSA
1048 in 4x SSC containing 0.2% Tween20 (Sigma-Aldrich, cat# P1379) at RT for 1 hr in a
1049 humidified chamber. Three 5 min washes were performed using 4x SSC with 0.2%
1050 Tween20 at 37°C. Coverslips were rinsed with CMF-PBS containing 0.1% Triton X-100
1051 and mounted with DABCO containing mounting medium with/without DAPI.
1052
1053 **RNA-FISH**
1054 smRNA-FISH was performed as reported previously (Kim et al., 2020). All
1055 reagents used for this procedure were RNase free and/or diethyl pyrocarbonate
1056 (DEPC)-treated (Sigma-Aldrich cat# D5758). Cells were fixed with 4%
1057 paraformaldehyde for 10 mins at RT in CMF-PBS. Three 5 min washes in CMF-PBS
1058 were followed by permeabilization with 0.5% Triton X-100 in CMF-PBS for 10 min at RT
1059 followed by 3x 5 min washes in CMF-PBS. Cells were equilibrated using 10%
1060 formamide in 2X SSC for 30 min at RT.
1061 smRNA FISH probes designed against HSPA1A (Kim et al., 2020), HSPH1
1062 (Zhang et al., 2021), and oligolibrary probes designed against MALAT1 (Supplementary
1063 Table 1) were used at a final concentration of (~300-500nM in hybridization buffer
1064 composed of 10% formamide, 10% (w/v) dextran sulphate (Sigma-Aldrich, cat# D8906),
1065 1 mg/ml Escherichia coli tRNA (Sigma-Aldrich, cat# R8759), 2 mM ribonucleoside
1066 vanadyl complex (NEB, cat# S1402), and 0.02% RNase-free BSA (Invitrogen, cat#

1067 AM2618) in 2X SSC. For Stellaris MALAT1-Quasar670 probes (Stellaris, cat# SMF-
1068 2046-1), 1.25μM final concentration was used instead of the recommended 0.125μM.
1069 Probe solution in hybridization buffer were applied to coverslips followed by incubation
1070 at 37°C for 15 hours in a humid chamber. Two 30 min washes with 10% formamide in
1071 2X SSC at 37°C were followed by post-fixation with 3.6 % paraformaldehyde in CMF-
1072 PBS buffer for 10 min at RT, followed by 3 x 5 min washes with CMF-PBS.
1073 Coverslips were incubated with blocking buffer containing 1% BSA (RNase-free,
1074 Invitrogen, cat# AM2618), 0.5% Triton X-100 and 20μM ribonucleoside vanadyl complex
1075 (NEB, cat# S1402) in CMF-PBS for 30 min at RT. Coverslips were then rinsed three
1076 times with CMF-PBS, followed by incubation with the appropriate antibody titer
1077 (Supplementary Table 1) diluted in CMF-PBS with 0.1% Triton X-10 containing 0.4 U/μl
1078 Ribolock RNase inhibitor (Thermo Fisher Scientific, cat# EO0381) for 45 min-1 hour at
1079 RT in a humid chamber. Coverslips were then washed 3 x 5mins with 0.1% Triton X-100
1080 in CMF-PBS for 5 minutes each. Secondary antibody incubation was performed similar
1081 to the primary antibody incubation except that the fluorescently tagged Goat anti-Rabbit
1082 / Goat anti-Mouse secondary antibodies (Supplementary Table 1) were diluted at 1:500.
1083 Subsequently, coverslips were washed 3 x 5 mins in CMF-PBS with 0.1% Triton X-100
1084 and mounted using Mowiol-DABCO antifade mounting medium.
1085
1086 **Wide-field fixed-cell imaging**
1087 Wide-field images were acquired (0.08 um pixel size) using an OMX V4
1088 microscope (Applied Precision) equipped with a U Plan S-Apo 100×/1.40-NA oil-
1089 immersion objective (Olympus), two Evolve electron-multiplying Charge-Coupled Device

1090 cameras (Photometrics). Images were aligned and deconvolved using the conservative
1091 deconvolution option within the Softworx program (Applied Precision).
1092
1093 **STORM imaging**
1094 For 2-color STORM imaging, we used the U2OS cell line expressing mEOS3.2-
1095 DDX39B from the endogenous locus as described elsewhere (Kim et al., 2025). Cells
1096 were fixed with 3.6% paraformaldehyde in CMF-PBS for 15 mins at RT, washed 3 x 5
1097 mins in CMF-PBS, and then incubated in blocking buffer (3% BSA (Thermo Scientific,
1098 cat# 37520), 0.5%Triton X-100 in CMF-PBS) for 30 mins at RT, followed by 3 x 5 min
1099 washes in CMF-PBS. Coverslips were incubated overnight at 4°C with the anti-THRAP3
1100 primary antibody (Santa Cruz Biotechnology Inc, cat# sc-133250) at 1:300 dilution in
1101 1% BSA in CMF-PBS.
1102 Coverslips were then washed 3 x 5 mins in CMF-PBS and then incubated for 2
1103 hours at RT with the goat anti-mouse Fab (Jackson ImmunoResearch, cat# 115-007-
1104 003) labeled with Alexa 647 at 5µg/ml at final concentration in 1% BSA in CMF-PBS.
1105 The Fab fragment was labeled with Alexa 647 (Invitrogen, Cat A20006) as described
1106 elsewhere (Hermanson, 2013; Bates et al., 2013). After this secondary antibody
1107 staining, coverslips were washed 3 x 5 mins in 0.1%Triton X-100 in CMF-PBS and then
1108 washed 2 x 5mins in CMF-PBS.
1109 The STORM imaging microscope system was described elsewhere (Kim et al.,
1110 2025). Alexa 647 signals were collected first, under continuous excitation with 647 nm
1111 laser (2kW/cm^2) and brief manual illumination with 405 nm LED illumination (0.1-0.5%
1112 intensity, Aura Light, Engine) for dye reactivation. Imaging was performed using a

1113 previously described imaging buffer (Bates et al., 2007), containing 5% glucose (Sigma-
1114 Aldrich, cat# G8270), 1% Glox (0.5mg/ml glucose oxidase, Sigma-Aldrich, cat#
1115 G2133), 40mg/ml catalase (Sigma-Aldrich cat# C100, in 50mM Tris with 10mM NaCl
1116 and 100 mM beta-mercaptoethanol (BME, Sigma-Aldrich, cat# M6250)). mEOS3.2
1117 signals were then acquired under continuous excitation with 561 nm laser (1.5kW/cm^2),
1118 and with brief manual illumination with 405 nm LED illumination for dye reactivation.
1119 Images were acquired at 15-20ms per frame in continuous mode, for a total of
1120 30000~50000 frames. Localization, drift correction, and chromatic alignment were
1121 performed using SMAP (Li et al., 2018; Ries, 2020).
1122
1123 **Live cell imaging**
1124 **Rapid wide-field imaging for short-term dynamics (second-timescale)**
1125 Cells were plated (~48 hours before imaging) on uncoated glass bottom 35 mm
1126 dishes with 14mm diameter and 1.5 thickness coverslip (MatTek, cat# P35G-1.5-14-C)
1127 such that cells were ~80-90% confluent at the time of imaging. For cell lines expressing
1128 proteins tagged with HaloTag, conditioned media containing Janelia Fluor(R) 646
1129 HaloTag(R) Ligand (Promega, cat# GA1120) diluted 1:5000 was added for 1-2 hours
1130 before imaging.
1131 For live-cell imaging we used the OMX V4 microscope together with a live cell
1132 incubator chamber (Applied Precision) and system including separate temperature
1133 control for the objective lens and incubator chamber and a humidified, 5% CO_2 air
1134 supply. Both the objective lens and incubator heaters were set to 37°C; after these

1135 temperatures were reached, the cell culture dish was placed on the microscope and
1136 cells were allowed to acclimatize to these conditions for ~1hr before beginning imaging.
1137 Imaging was performed using simultaneous solid-state illumination with 31.3%
1138 transmittance for THRAP3/DDX39B and 10% transmittance for SON using 10-15 ms
1139 exposure for each Z-section. Optical section z-stacks (Z spacing 200 nm, ~ 1 micron z-
1140 depth) were acquired every 1 sec for 1-2 mins.
1141
1142 **Wide-field imaging for long-term dynamics (multiple hour-timescale)**
1143 Live cell imaging for greater than 10 hours was performed as described elsewhere (Kim
1144 et al., 2025) using a custom-built microscope setup.
1145
1146 **5-Ph-IAA induced SON-SRRM2 degradation**
1147 SON and SRRM2 double knockdown in the HCT116 mAID-Clover-SON SRRM2-
1148 mAID-mCherry cell line was achieved by adding to the media 5-phenyl-1H-indole-3-
1149 acetic acid (5-Ph-IAA, Tocris Biosciences, cat # 7392) to a final concentration of 5μM
1150 using a stock solution of 10mM in dimethyl sulphoxide (DMSO, Avantor cat#
1151 IC0219605590).
1152 For live cell visualization of DDX39B during SON and SRRM2 DKD, the HCT116
1153 mAID-Clover-SON SRRM2-mAID-mCherry cell line was transfected with the Halotag-
1154 DDX39B plasmid (Supplementary Table 1) and selected in cell culture media containing
1155 450 μg/ml G418 (Gibco,cat# 10131035) for ~ 2 weeks. Cells expressing Halotag-
1156 DDX39B were stained overnight with JF646 (50 pM Promega cat# GA1120). After

1157 adding 10~20μM 5-Ph-IAA, we acquired live cell movies to observe SON and SRRM2
1158 degradation while visualizing Halotag-DDX39B.
1159
1160 **RNP transgene induction and RNP localization relative to DDX39B, THRAP3, and**
1161 **SON / SRRM2 (NS)**
1162 U2OS cell lines stably expressing the E6 β-globin and mini-Dystrophin A-1
1163 transgenes tagged with the MS2 repeats and expressing a YFP-fused MS2 binding
1164 protein (Mor et al., 2010; Brody et al., 2011), were seeded (~30,000 cells) on 12mm
1165 #1.5 coverslips (Electron Microscopy Sciences cat# 72230-01). For E6, cells were
1166 treated with 15 μg/ml doxycycline (Sigma-Aldrich cat#D5207) for 6, or 16 hours, while
1167 mini-dystrophin cells were treated with 1 μg/ml Ponasterone A (Enzo Life Sciences) for
1168 the same durations to induce transgene expression. Cells were fixed in 4% PFA for 20
1169 mins at RT. Cells were permeabilized in 0.5% Triton X-100 in 1x PBS for 10 min, and
1170 blocking was applied using a buffer composed of 0.1% Triton X-100 and 5% bovine
1171 serum albumin (BSA) fraction V (MP Biomedicals cat# 160069) for 1 hour at RT.
1172 Primary antibodies were diluted in blocking buffer (Supplementary Table 1) and applied
1173 to coverslips overnight at 4°C for 16 hours in a humidified chamber. Coverslips then
1174 were washed for 5 mins three times using 0.1 % Triton X-100. This was followed by
1175 incubation with secondary antibodies for 1 hour at RT and then washes for 5 mins three
1176 times using 0.1 % Triton X-100. The nucleus was stained with SYTOX deep red nucleic
1177 acid stain (Invitrogen cat# S11381) for 20 min, followed by final rinses with 1x PBS.
1178 Secondary antibodies used; Alexa Fluor 405-conjuated goat anti rabbit IgG (1:500,

1179 Abcam cat# ab175652) and Rhodamine red-conjugated donkey anti mouse IgG (1:250,
1180 Jackson Immunoresearch cat# 715-297-003).
1181 Confocal imaging was performed on a Leica SP8 inverted microscope. The
1182 objective used was 100x 1.4 NA, with Leica immersion oil, at room temperature. The
1183 mounting medium was custom made 80% glycerol with p-phenylenediamine antifade
1184 (Sigma). The resulting images were deconvolved with Huygens Professional (Scientific
1185 Volume Imaging, Hilversum, The Netherlands) using the CMLE algorithm, with signal-
1186 to-noise ratios of 12 and 5 iterations, using the Huygens confocal module.
1187
1188 **RNA-Seq sample preparation and analysis**
1189 **Cell synchronization and protein depletion:** For synchronization at the G1/S
1190 boundary (JavanMoghadam-Kamrani and Keyomarsi, 2008), HCT116 mAID-Clover-
1191 SON SRRM2-mAID-mCherry CMV-OsTIR1(F74G) cells were seeded in 6-well plates
1192 and grown to approximately 80% confluency, followed by treatment with 20 μM
1193 Lovastatin (Mevinolin; LKT Laboratories, cat# M1687) for 24 hours. To release the G1
1194 arrest but block cells at the G1/S boundary, cells were rinsed three times with pre-
1195 warmed, CO_2-equilibrated culture medium supplemented with 2 mM Mevalonic acid
1196 (Mevalonolactone; Millipore-Sigma cat# M4667) and 2 mM thymidine (Millipore-Sigma,
1197 cat# T9250).
1198 Degradation of AID-tagged proteins was induced by the addition of 5 μM 5-Ph-
1199 IAA simultaneously with the release of the G1 block by addition of the Mevalonic
1200 acid/thymidine-containing media. Cells were incubated for 16 hours after this G1 block
1201 release. Control cells were treated the same except that an equivalent volume of DMSO

1202 without added 5-Ph-IAA was added. The G1 arrest followed by addition of 5-Ph-IAA
1203 coincident with the release of this block for the G1/early S synchronization was used to
1204 minimize cell cycle-related variability between DMSO-treated controls and the
1205 SON/SRRM2-depleted samples.
1206
1207 **RNA extraction and RNA-seq:** Cells in a 6-well plate were rinsed twice with ~1
1208 mL of cold CMF-PBS per well, and total RNA was extracted immediately using the
1209 RNeasy Plus Mini Kit (Qiagen, cat# 74134), following the manufacturer's protocol.
1210 Purified RNA eluted in RNase-free water was treated with 2U DNase I (New England
1211 Biolabs, cat# M0303S) for 20 mins at 37°C, followed by DNase I inactivation by adding
1212 5 μM EDTA (Thermo Fisher Scientific, cat# J15694.AE) and 10 mins incubation at 75°C.
1213 RNA integrity was assessed at the DNA Services Facility, Roy J. Carver
1214 Biotechnology Center (University of Illinois at Urbana-Champaign), using an Agilent
1215 Bioanalyzer. All samples exhibited RNA Integrity Numbers (RIN) of 10. Ribosomal RNA
1216 was depleted using the FastSelect HMR kit (Qiagen, cat# 334386). RNA-seq libraries
1217 were prepared with the KAPA HyperPrep Stranded mRNA Library Kit (Roche, cat#
1218 KK8580), quantified by qPCR, pooled, and sequenced on a NovaSeq X Plus instrument
1219 using V1.0 sequencing chemistry for 151 paired-end cycles. Adapter trimming was
1220 performed on the 3′ ends of reads, using the first 33 nucleotides of the adapter
1221 sequences for trimming. FASTQ files were generated and demultiplexed using
1222 Illumina's bcl2fastq v2.20 software.
1223

1224 **RNA-seq analysis:** The quality of trimmed reads was assessed using FastQC
1225 with default parameters. High-quality reads were aligned to the human reference
1226 genome (GRCh38/hg38) using STAR aligner (Dobin et al., 2013), with the
1227 corresponding GTF annotation file obtained from Ensembl. Differential gene expression
1228 analysis was performed using the DESeq2 R package (Love et al., 2014) using DMSO-
1229 treated samples as controls. Genes with an adjusted p-value (Padj) < 0.05 (Benjamini-
1230 Hochberg correction) were considered significantly differentially expressed
1231 (Supplementary Table 2).
1232
1233 **Image analysis**
1234 All fixed-cell images shown are single optical sections unless indicated
1235 otherwise. Non- linear exponential gamma scaling of 0.8 was applied to all images of
1236 DDX39B, MALAT1 and RBM8A to reduce the intensity dynamic range and thus facilitate
1237 the visualization of low-intensity nuclear regions. Images presented in the live-cell
1238 imaging videos are 2D maximum-intensity projections of the original optical section z-
1239 stacks acquired at each time point. All images were processed using Fiji (ImageJ)
1240 (Schindelin et al., 2012).
1241
1242 **Protein-intensity quantification within and outside NS**
1243 A single optical z-section containing the max-signal over the entire z-stack for NS
1244 (SON or SRRM2) was selected using the np.max function in the Python NumPy
1245 package (Harris et al., 2020). The intensity distribution of each candidate protein inside
1246 versus outside of NS was assessed as follows: Pixels with intensities < 10% of the

1247 maximum signal of the protein were considered “noise” and discarded. A nuclear mask,
1248 established by DAPI staining, was applied to both the NS and candidate protein images.
1249 NS were defined by SON/SRRM2 intensity thresholds established using Otsu
1250 thresholding (Otsu, 1979). The remaining pixels showing candidate protein "positive"
1251 signals (>10% maximum intensity threshold) were then divided into two categories:
1252 “Protein within NS” for pixels overlapping with the NS segmented regions and “Protein
1253 outside NS” for remaining positive pixels outside the NS segmented regions. The
1254 resulting images were displayed using the “viridis” LUT color-map. Cumulative-intensity
1255 percentile plots of the “Protein within NS” and “Protein outside NS” staining distributions
1256 were generated using the Python package Matplotlib (Hunter, 2007).
1257

1258 **Network changes upon transcriptional inhibition with DRB**

1259 A Fiji macro (“Skeletonize”, See Code Availability Section) was created for this
1260 quantification. Briefly, for each image, the SON channel was used to generate a NS
1261 mask. Then, all pixels of the protein channel that overlapped with the NS mask were set
1262 to zero intensity to generate an image of only the protein outside NS. The resultant
1263 image was converted into a binary image using Otsu thresholding (Otsu, 1979). Using
1264 the Fiji Skeletonize function (fiji.sc/Skeletonize3D), “protein skeletons” were generated,
1265 and branch lengths and number of branches/skeleton were calculated. Total skeleton
1266 length was computed by summing the lengths of all the skeletons within a nucleus.
1267 Number of connections was the number of unique skeletons (length > 5 pixels)
1268 identified within a single nucleus.
1269

1270 **Distance measurement for RNA Pol II foci relative to SON, THRAP3 and DDX39B**
1271 **networks**

1272 RNA Pol II Ser2p and Ser5p staining foci locations were determined using the
1273 'Find Maxima' function in ImageJ. Detected locations were assigned a pixel value of 1,
1274 while all other pixel values were set to 0, converting the Pol II image into a binary image
1275 containing only Pol II locations. The binary image was then imported into a custom
1276 MATLAB code for distance measurements relative to NS
1277 (https://github.com/Jiahkim/distancebtwlocusNS.git) . Pol II-positive pixels were first
1278 classified based on whether they overlapped with NS regions. NS areas were defined
1279 by segmentation of a target NS marker using local thresholding (Bradley and Roth,
1280 2007). For Pol II-positive pixels outside NS area, distances to the nearest pixel at the
1281 NS boundary were as calculated.
1282

1283 **Distance measurement for Type I and Type II DNA-FISH spots relative to SON,**
1284 **THRAP3 and DDX39B**

1285 To measure distance of a spot to SON, THRAP3 and DDX39B, we used the
1286 Loci_Compartment_Distance ImageJ plugin described elsewhere (Kumar et al., 2024).
1287 Since the THRAP3 and DDX39B networks are widely distributed within the nucleus, and
1288 due to limited Z-resolution, we used a single optical section for THRAP3 and DDX39B
1289 analysis. For NS detection, we used the sum-projection of 3 optical sections centered
1290 over the brightest spot of the locus. To define the edge of the compartment boundary,
1291 the intensity drop of 50% of the local maximum intensity (after background correction)
1292 was used to locally segment the image. The center of mass of the DNA FISH spot

1293 signal was used as the spot center location and the shortest distance between the spot
1294 center to the nearest compartment edge was measured.
1295

1296 **Categorizing and assessing alignment of DNA-FISH trajectories relative to SON,**
1297 **THRAP3 and DDX39B foci**

1298 To eliminate DNA FISH background staining signals, for the DNA FISH mapping
1299 of chromosome trajectories, only the "Apex" biotin signals that colocalized adjacent to
1300 DNA-FISH signals for the “Arm” regions were considered as true positive Apex signals.
1301 Additionally, the Apex signal had to be at least 2-fold higher intensity than single biotin
1302 spots seen elsewhere in the nucleus to be considered for analysis. For analysis, a sum-
1303 projection was generated of all the consecutive optical sections which contained an
1304 individual trajectory FISH signal consisting of positive DNA-FISH Apex and Arm signals.
1305 Chromosome trajectories were categorized as condensed if the Arm region appeared
1306 as a single spot or blob next to an Apex DNA-FISH spot. Any Arm region appearing as
1307 2 or more spots was termed “decondensed”. For alignment, a trajectory was considered
1308 aligned only if all the spots of the Arm and Apex were either overlapping or adjacent and
1309 in-contact to THRAP3 or DDX39B foci. In all other cases, the chromosome trajectory
1310 was classified as not aligned.
1311

1312 **Distance measurements of Trajectory Apex versus Arm regions from nearest NS,**
1313 **THRAP3, or DDX39B foci**

1314 DNA-FISH spots for Trajectory Apex and Arm were detected using the "blob log"
1315 function within the scikit-Image Python package (Van Der Walt et al., 2014) and were

1316 clustered using DBSCAN (Ester et al., 1996). For this clustering, an iterative threshold
1317 estimation method was employed such that the number of clusters per nucleus was 3-4.
1318 For each cluster, the cluster center was calculated and a box of 30x30 pixels (x-y) from
1319 the center was cropped; within this cropped volume, 7 optical sections (z-slices) were
1320 sum intensity projected to create a new 2D image, within which the center of mass of
1321 the Apex signal was calculated. Within the same 2D cropped projection, the Arm region
1322 signal was segmented and the pixels within the segmented region were split into three
1323 categories, for each of which their center-of-mass determined: 1) "Arm-close": 25%
1324 pixels closest to Apex; "Arm-far": 25% pixels farthest from Apex; "Arm-middle";
1325 remaining pixels. The DDX39B or THRAP3 and NS signals were thresholded using the
1326 Otsu function (Otsu, 1979). The shortest Euclidean distance between the center of each
1327 DNA-FISH spot (Apex or Arm) to the nearest edge of the segmented protein/speckle
1328 was measured.
1329
1330 **Distance measurements of E6 and mini-Dystrophin transgene RNAs relative to**
1331 **SON, THRAP3 and DDX39B foci**
1332 Distance measurements for transgene RNAs, tagged with MS2 repeats and
1333 MS2-binding proteins, relative to NS (SON/SRRM2), DDX39B, or THRAP3 foci were
1334 performed similarly to the RNA PolI II foci distance measurements. Nuclear regions
1335 were manually selected, and RNA spots within each nuclear region were identified
1336 using the 'Find Maxima' function, to generate binary images. NS areas were segmented
1337 using the Otsu' thresholding algorithm (Otsu, 1979) which effectively defined

1338 perispeckle and NS boundaries. For this data, plotting and statistical tests were
1339 performed using GraphPad Prism.
1340

1341 **Distance measurement of HSPH1 and HSPA1 RNAs relative to SON, THRAP3, and**
1342 **DDX39B foci**

1343 For HSPH1 and HSPA1 RNA-FISH analysis, images were denoised using the
1344 “despeckle” function in ImageJ and a Gaussian filter of 1 pixel radius applied afterwards
1345 Distance measurements relative to SON, THRAP3 and DDX39B foci were performed
1346 using the ImageJ plugin as described for DNA-FISH measurements of Type I and Type
1347 II SON TSA-seq peaks.

1348 For Mander’s coefficient calculations, we used a maximum-intensity projection of
1349 3 optical sections of the "despeckle" denoised and Gaussian fitered images. A nuclear
1350 mask was generated using the DAPI signal and Otsu thresholding (Otsu, 1979) and
1351 applied to the RNA and protein signals. These nuclear-masked images were then used
1352 for calculating Mander’s coefficient using the JaCoP plugin (Bolte and Cordelières,
1353 2006) in Fiji (Schindelin et al., 2012).
1354

1355 **Plotting and Statistical Analysis**

1356 All plots, unless otherwise stated, were generated using the ggplot2 package in
1357 R version R4.2.2. All analysis of variance (ANOVA) used type 3 comparison using the
1358 “car” package. The options were set as options (contrasts=c (“contr.sum”, “contr.poly”)).
1359 We used a generalized linear model with gamma distribution followed by the Tukey
1360 posthoc test. For RNA Pol II foci and RNA-FISH distance measurements, the Kruskal-

1361 Wallis test followed by the pairwise Wilcoxon test was used to calculate P-values as
1362 indicated in the figures. For Mander's coefficient comparison, an unpaired t-test was
1363 used in R. All boxplots represent the interquartile range with the upper line indicating
1364 75% and the bottom line indicating 25%. Central line indicates median, and whiskers
1365 represent the range of data shown.

1366 **Figure legends:**

1367 **Figure 1: Screening for potential markers of alternative "gene expression hubs"**

1368 A. TSA-seq SON Type 1 (dark magenta) and Type 2 (dark green) peaks differ in their
1369 association with and average distance from NS. Type 2 peaks represent active genomic
1370 regions, weakly associated with NS, that might instead preferentially interact with an
1371 alternative nuclear active niche (yellow) present in the interchromatin (IC) space.
1372 Contact with this alternative active niche might boost gene expression (right panel).
1373 B. Screening pipeline for the identification of proteins that occupy IC space, illustrated
1374 with THRAP3 as an example candidate protein. (Left) Transient transfection of EGFP-
1375 tagged constructs (gray) in some cases showed varied distributions based on
1376 expression levels (gradient, left), which often accompanied changes in NS morphology.
1377 (Middle) Candidates showing a network-like pattern at low expression levels were
1378 validated by antibody staining of the endogenous protein. (Right) Candidate proteins
1379 were grouped into the same staining pattern if they showed extensive colocalization
1380 throughout the nucleus.
1381 C-D: Perispeckle THRAP3 Pattern (PSTP) (C) and Perispeckle DDX39B Pattern
1382 (PSDP) (D) represent two networks within the IC space that show protein
1383 concentrations in the vicinity of NS but also extend outwards in a network-type pattern.
1384 Insets: Box 1 (yellow borders): string of foci form linear thread-like structures; Box 2
1385 (white borders): thread-like extensions at the nuclear periphery; Box 3 (pink borders):
1386 thread-like extensions connecting nearby NS. PSTP proteins are present at similar
1387 concentration within and outside NS, but PSDP proteins are concentrated inside NS as
1388 compared to the network outside of NS.

1389 E-F: Colocalization of PSTP (E) and PSDP (F) proteins. (E) Immunostaining of BCLAF1
1390 (gray) relative to THRAP3 (magenta) and EGFP-SON (yellow). (F) Immunostaining of
1391 RBM8A (gray) relative to mCherry-DDX39B (green) and EGFP-SON (yellow). Line
1392 profiles along the arrows (shown in merged insets) show overlapping peaks
1393 (arrowheads) of BCLAF1 and THRAP3 (left) or RBM8A and DDX39B (right). Scalebars:
1394 5 μm (main images) and 1 μm (insets).
1395
1396 **Figure 2: Highly dynamic PSTP and PSDP networks appear, disappear, and**
1397 **reappear within the same or nearby IC space**
1398 A and B: Live-cell imaging of endogenously tagged EGFP-THRAP3 (A, Video 1) and
1399 mCherry-DDX39B (B, Video 2) along with SON (gray) over 1 second (s) intervals shows
1400 linear thread-like protein concentrations ("structures") appear and disappear within the
1401 vicinity of NS (see Videos 1 and 2). Time projections over 60 seconds (middle and right
1402 panels) show these thread-like structures more clearly, indicating they consistently recur
1403 within the same spatial locations, with some foci (arrows) showing a relative increase in
1404 brightness, suggesting more stable and/or frequent accumulation of protein at these
1405 regions over time. Scale bar=5 μm. Insets (A' and B') show the dynamics of single
1406 thread-like structures over 1 second intervals. Blue (A') and green (B') boxes show
1407 sequential frames in which thread-like structures form and remain stable over a number
1408 of seconds. These structures then disappear but reform at later times (arrowheads) in
1409 the same region. Sixty second time projection of the same structures are shown
1410 enlarged in insets ((A)and (B), right). Scale bar= 1 μm. THRAP3 and DDX39B
1411 intensities are scaled using a blue-orange LUT (Fiji, blue-orange-icb LUT).

1412 C and D: Endogenously tagged mCherry-THRAP3 (C; magenta, Video 3) and mCherry-
1413 DDX39B (D; magenta, Video 4) networks are stable within the interchromatin (IC) space
1414 over hours (~10-14 hours (h)) in live cells (see Videos 3 and 4). Insets (bottom panels)
1415 show boxed region (top panel, white borders) at multiple time-points. Nuclear speckles
1416 (yellow) form and fuse and/or remain stable (arrowheads) within the vicinity of
1417 perispeckle networks, while thread-like projections of THRAP3 or DDX39B appear,
1418 disappear, and then reappear repeatedly within the same regions (arrows). DNA (cyan)
1419 is visualized by SiR-Hoechst staining. Scale bar= 1 μm.
1420
1421 **Figure 3: PSTP and PSDP subdivide the interchromatin space and respond**
1422 **differently to functional perturbation**
1423 A: Wide-field imaging of immunostained THRAP3 (magenta) and DDX39B (green)
1424 relative to SON (EGFP-SON knock-in; yellow) in U2OS cells shows that the two
1425 perispeckle networks are juxtaposed outside of NS. Insets show enlargements of boxed
1426 regions (rectangles 1,2). Line profile plots (along white arrows within insets) show
1427 THRAP3 and DDX39B peaks are offset from each other. Scale bars- 5 μm main image;
1428 1 μm inset.
1429 B: STORM super-resolution imaging of immunostained THRAP3 (magenta) and
1430 DDX39B (green) demonstrates more clearly the spatial separation of THRAP3 versus
1431 DDX39B concentrations suggested by wide-field microscopy (A). Insets are
1432 enlargements of boxed regions (white rectangles 1, 2) and highlight nuclear regions
1433 showing THRAP3 and DDX39B occupying distinct spaces. Line profile plots (along
1434 yellow or white arrows within inset 1) show peaks of THRAP3 and DDX39B

1435 concentrations separated by distances of ~20-30 nm. Scale bars- 5 μm main image; 1
1436 μm inset.
1437 C-D: Transcriptional inhibition by 5,6-Dichloro-1-β-D-ribofuranosylbenzimidazole (DRB)
1438 treatment disrupts THRAP3 perispeckle pattern (C; magenta) but DDX39B perispeckle
1439 pattern (D; green) remains relatively unchanged. NS (yellow) are marked by SON (C-
1440 top) or SRRM2 (D-bottom). THRAP3 progressively condenses into distinct foci arranged
1441 frequently in thread-like structures and ultimately accumulates in cap-like accumulations
1442 adjacent to NS (Video 5). Scale bars- 5 μm main image; 1 μm inset.
1443 E-F: Box plots showing total skeleton length (E) and number of connections (F) of
1444 THRAP3 and DDX39B networks (SFig. 3A) upon DRB treatment (1, 2 hours (h)) as
1445 compared to DMSO (2 hours). Central line indicates median and square within the
1446 boxplot indicates mean. n (number of nuclei) = 10 for each condition. One-way ANOVA
1447 with Tukey post-hoc test was used to calculate P-values. ns : $P > 0.05$; ** : $P \leq 0.01$; ***:
1448 $P \leq 0.001$.
1449
1450 **Figure 4: RNA pol2 Ser2p foci localize in close proximity to PSTP and PSDP**
1451 A-F: Immunostaining of RNA Pol II serine 2 phosphorylated foci (white) (A-C) and serine
1452 5 phosphorylated foci (white) (D-F): RNA pol II foci (arrowheads) not near NS (SON,
1453 orange; endogenously tagged with EGFP) align adjacent to THRAP3 (magenta;
1454 immunostaining) and DDX39B (green; endogenously tagged with mCherry) foci within
1455 the IC space. RNA Pol II foci at the edge of SON-marked speckles indicated by yellow
1456 circles. Images A-B and D-E (gray boxes) show Pol II foci in the same nucleus relative
1457 to SON and DDX39B.

1458 G-H Distance distribution curves for the percentage of RNA Pol II serine 2
1459 phosphorylated foci (G) and serine 5 phosphorylated foci (H) relative to SON, THRAP3
1460 and DDX39B.
1461 I: Boxplots showing average distance of foci relative to RNA Pol II foci relative to SON,
1462 THRAP3 and DDX39B. Central line indicates median distance and square within the
1463 boxplot indicates mean distance. P-values calculated using Wilcoxson sum rank test; **:
1464 P ≤ 0.01; ****: P ≤ 0.0001. (n=9124-81267 RNAPII foci).
1465
1466 **Figure 5: Gene expression hot-zones interact preferentially with PSTP and PSDP**
1467 **in HCT116 cells**
1468 A: Representative TSA-seq plot for chromosome 2 in HCT116 cells for SON (blue),
1469 DDX39B (green), THRAP3 (magenta), Lamin B1 (black), and Lamin B1 Dam-ID (gray).
1470 Yellow and blue highlights mark Type I peaks and Type II peaks, respectively. Type I
1471 peaks show large magnitude peaks for SON but lower amplitude and broader peaks for
1472 DDX39B and THRAP3. Type II peaks show well-defined and higher magnitude peaks
1473 for DDX39B and THRAP3 as compared to SON.
1474 B: Scatterplots between two SON TSA-seq replicates (orange), SON vs DDX39B
1475 (green) and SON vs THRAP3 (magenta). Overall, TSA-seq scores for DDX39B and
1476 THRAP3 correlate closely with SON. Both DDX39B and THRAP3 versus SON
1477 scatterplots show two regions with distinct slopes: higher for negative SON scores
1478 (black dotted line) but lower for positive SON scores (white dotted line).
1479 C: DNA-FISH (yellow) in HCT116 cells for multiple Type I and Type II peaks (apex)
1480 shows higher frequency of association with NS (SON-cyan or SRRM2-blue) for Type I

versus Type II peaks. NS non-associated alleles show close proximity or locate adjacent to THRAP3 (magenta) or DDX39B (green) foci/accumulations. Regions highlighted in white boxes are shown on the right as insets. Scale bars- 5 μm main image; 1 μm inset.

D: Violin plots showing distance of DNA-FISH spots relative to SON, DDX39B and THRAP3 foci/accumulations. Central line indicates median distance and white square within the boxplot indicates mean distance. (n (alleles) as indicated: 67 (Type I) and 95 (Type II) SON; 114 (Type I) and 103 (Type II) DDX39B; 105 (Type I) and 96 (Type II) THRAP3). One-way ANOVA with Tukey post-hoc test was used to calculate P-values. ns : $P > 0.05$; *** : $P \leq 0.001$; **** : $P \leq 0.0001$.

E-G: Probability density plots for distance distribution of DNA-FISH spots relative to SON (E), DDX39B (F) and THRAP3 (G) foci/accumulations for Type I (yellow) and Type II (blue) peaks. (n (alleles) as indicated: 67 (Type I) and 95 (Type II) SON; 114 (Type I) and 103 (Type II) DDX39B; 105 (Type I) and 96 (Type II) THRAP3).

Figure 6: Mapping of chromosome trajectory- SON TSA-seq peak to nearest LAD- shows alignment along PSTP and PSDP foci / concentrations

(A-B) Left, top panels: Browser views showing SON, DDX39B, THRAP3, Lamin B1 TSA-seq and Lamin B1 DamID tracks corresponding to one Type I (A) or Type 2 (B) SON TSA-seq peak-to-valley chromosome trajectories mapped by DNA FISH. Highlights show locations of peak "Apex" (yellow) and multiple "Arm" (grey) DNA FISH probes.

1503 (A-B) Right: Sum-intensity projections of Type I (A) or Type II (B) Apex versus Arm
1504 probes along peak-to-valley chromosome trajectories and their spatial positioning
1505 relative to THRAP3 (magenta), DDX39B (green), and nuclear speckles (SON/SRRM2;
1506 blue) immunostaining. The percentage of DNA trajectories appearing aligned with
1507 perispeckle staining is higher for DDX39B versus THRAP3. Scalebar=1 μm.
1508 (A-B) Left, bottom panels: Statistics for Apex versus Arm chromosome orientation
1509 relative to foci of SON, THRAP3, and DDX39B summarized in box plots. Apex FISH
1510 signals are statistically significantly closer to SON, THRAP3, and DDX39B foci than to
1511 middle and distal Arm FISH signals for the Type I trajectory. Apex FISH signals are
1512 closer to middle and statistically significantly closer to distal Arm signals relative to
1513 THRAP3 foci, but not SON or DDX39B foci, consistent with the distal positioning of
1514 Type II trajectories relative to NS and the higher trajectory alignment seen relative to the
1515 DDX39B versus THRAP3 staining. Black squares represent mean distances and central
1516 line represents median distances. n (number of trajectories analyzed): Type I trajectory:
1517 THRAP3/SON = 40; DDX39B/SRRM2= 66; Type II trajectory: THRAP3/SON=82;
1518 DDX39B/SRRM2=54. Kruskal-Wallis test followed by Dunn's post-hoc test was used to
1519 calculate P-values. ns : $P > 0.05$; * : $P \leq 0.05$; ** : $P \leq 0.01$; *** : $P \leq 0.001$; **** : $P \leq$
1520 0.0001.
1521
1522 **Figure 7: RNA from intron-containing and intronless genes associate**
1523 **differentially with PSTP and PSDP**
1524 A-B: RNAs (yellow) produced by the transgene array expressing the "E6" (6 exons)
1525 construct with βeta-globin sequences (A) localize more closely to THRAP3 foci /

1526 concentrations (magenta) than RNAs produced by the transgene array expressing the
1527 "mini-Dystrophin" (B) construct with a single exon (no introns). SON (NS) is cyan. Both
1528 RNAs are tagged with MS2 repeats and visualized by expression of the MS2-coat
1529 protein fused with YFP.
1530 (C-D) RNAs produced by both the E6 (C) and mini-Dystrophin (D) constructs localize
1531 closely with DDX39B (green) foci / concentrations. SRMM2 (NS) is blue.
1532 (E-F) FISH signals (yellow) for RNAs produced by the endogenous HSPH1 gene with
1533 many introns (E) localize closer to THRAP3 foci / concentrations (magenta) than RNAs
1534 produced by the endogenous HSPA1A and HSPA1B genes with no introns (F). SON
1535 (NS) is cyan.
1536 (G-H) FISH signals (magenta) for RNAs produced by the endogenous HSPH1 gene
1537 with many introns (E) and the endogenous HSPA1A and HSPA1B genes with no introns
1538 (H) both localize close to DDX39B (green) SRRM2 (NS) is blue.
1539 I: Box-plots of distances of β-globin E6 and mini-Dystrophin RNAs relative to SON,
1540 THRAP3, SRRM2 and DDX39B. n (number of RNPs per sample)= 1212-2627. Kruskal-
1541 Wallis test followed by Dunn's multiple comparisons test was used to calculate P-
1542 values. ns : P > 0.05; * : P ≤ 0.05; ** : P ≤ 0.01; *** : P ≤ 0.001; **** : P ≤ 0.0001.
1543 J: Box plots of distances of HSPH1 and HSPA1 RNA relative to SON, THRAP3 and
1544 DDX39B. n (RNA spots) = 168-257. RNPs from 5-8 nuclei used for this analysis.
1545 Kruskal-Wallis test followed by pairwise Wilcoxon test was used to calculate P-values.
1546 ns : P > 0.05; * : P ≤ 0.05; ** : P ≤ 0.01; *** : P ≤ 0.001; **** : P ≤ 0.0001.
1547 K: Box plots showing average fraction overlap (Manders coefficient) between RNA
1548 signals and THRAP3 or DDX39B foci / concentrations for HSPH1 and HSPA1 RNAs.

1549 White squares represent mean and central line represents median. (n (number of
1550 nuclei): HSPH1 18; HSPA1 18). Kruskal-Wallis test followed by pairwise Wilcoxon test
1551 was used to calculate P-values. ns : P > 0.05; * : P ≤ 0.05; ** : P ≤ 0.01; *** : P ≤ 0.001;
1552 **** : P ≤ 0.0001.
1553 (A-D) Scale bar=1 μm. (E-H) Scale bar= 5 μm main image; 1 μm inset.
1554 (A-H) Regions highlighted within white boxes are shown as insets on the right.\
1555
1556 **Figure 8: Perispeckle networks and genome positioning are largely maintained**
1557 **after NS depletion but NS-proximal genes are downregulated**
1558 A: SON (mClover, green) and SRRM2 (mCherry, magenta) intensities (y-axis) as a
1559 function of time (x-axis, hours) after 5-Ph-IAA treatment as measured by flow cytometry
1560 reveals maximum double knockdown after ~ 4 hours in these HCT116 cells.
1561 B: Live-cell imaging reveals DDX39B distribution shows minimal changes during
1562 process of NS elimination (Video 6). Left: Pseudocolor intensity mapping of mClover-
1563 SON (endogenous gene expression, top panels) versus HaloTag-DDX39B (transiently
1564 expressed, bottom panels) at 20 (left) versus 65 (right) minutes after 5-Ph-IAA induced
1565 double knockdown (DKD) of SON and SRRM2. Right: Inset frames show SON (top) or
1566 DDX39B (bottom) over a single NS region at different times (minutes, m) after DKD.
1567 Percentages of SON (top) or DDX39B (bottom) remaining over NS region relative to the
1568 first frame intensities are shown as white numbers (bottom right, each frame).
1569 Scale bar- 5 μm main image; 1 μm inset.

1570 C: Immunostaining of DDX39B (cyan) and THRAP3 (magenta) without (top panel) or
1571 with 5-Ph-IAA treatment for 4 hours (bottom panel). SON (yellow) and SRRM2 (gray)
1572 marked NS undergo degradation within 4 hours.
1573 D: Loss of nuclear poly-A RNA concentrations within NS occurs after NS elimination by
1574 DKD (5-Ph-IAA treatment). Nucleus (upper left) with significant SON (green) and
1575 SRRM2 (magenta) still remaining in NS also still shows poly-A (middle panel, grey; right
1576 panel, yellow) FISH signal accumulations within NS; dispersal of poly-A accumulation is
1577 seen in two nuclei (right) with greater SON and SRRM2 DKD.
1578 E: DDX39B (green) and THRAP3 (magenta) TSA-seq profiles of chromosome 2 in
1579 HCT116 cells engineered with AID2-inducible degron tagged SON and SRRM2 alleles
1580 after DMSO (dark colors) versus 5-Ph-IAA (light colors) treatment for 4 hours. SON
1581 TSA-seq (black) from WT cells is shown in comparison. Type I (yellow highlights) and
1582 Type II (blue highlights) peaks show little or no change in DDX39B and THRAP3 peak
1583 amplitudes after DKD.
1584 F-H. Differentially expressed genes (DEG) near SON TSA-seq Type 1 peaks show a
1585 strong bias towards downregulation. In contrast, DEG near SON TSA-seq Type 2
1586 peaks show bias towards upregulation, particularly for SON TSA-seq peak amplitudes
1587 less than or equal to zero.
1588 F: Volcano plot showing log2 fold expression changes versus log10 (False Discovery
1589 Rate) for DEG present +/- 500 kb from SON TSA-seq Type I (yellow) and Type II (blue)
1590 peaks in HCT116 cells after 5-Ph-IAA-induced SON-SRRM2 degradation.
1591 G: Scatterplot showing mean SON TSA-seq score versus log2 fold changes for DEG
1592 present +/- 500 kb of Type I (yellow) and Type II (blue) peaks. Numbers of DEG flanking

1593 Type II peaks with SON TSA-seq peak amplitudes less than or equal to zero (left of
1594 grey dashed vertical line) are indicated in blue.
1595 H: Density plot with log2 fold change of upregulated and downregulated genes within
1596 Type I and Type II regions. Type I: 162 upregulated genes and 897 downregulated
1597 genes; Type II: 192 upregulated genes and 144 downregulated genes.
1598
1599 **Figure 9: Model showing organization of genes relative to NS and DDX39B (PSDP)**
1600 **and THRAP3 (PDTP) perispeckle patterns**
1601 A: We propose NS versus perispeckle patterns correspond to two different nuclear
1602 niches acting as gene expression "hubs" for two different sets of genes. These sets of
1603 genes are contained within chromosomal regions with similarly elevated levels of gene
1604 expression but differential localization relative to NS. Genes near SON TSA-seq Type I
1605 peaks (Type I gene expression hot-zones) associate closely with NS (blue). Genes
1606 near SON TSA-seq Type II peaks (Type II gene expression hot-zones) mostly locate
1607 away from NS but near perispeckle patterns marked by THRAP3 (magenta, PSTP) and
1608 DDX39B (green, PSDP). Transcripts from intron-rich genes (yellow) associate with
1609 PSTP and PSDP while transcripts from intronless genes (red) associate only with
1610 PSDP.
1611 B: After NS depletion, genome organization relative to PSTP and PSDP remains largely
1612 the same, although many of the Type I set of genes are downregulated in the absence
1613 of NS, suggesting that NS confer added gene expression amplification for this set of
1614 genes.

1615 C: We imagine that positive regulation of gene expression may result from one set of
1616 genes associating with NS and the other set of genes associating with perispeckle
1617 patterns. Previous observations of gene movements from the nuclear lamina towards
1618 the nuclear interior and/or towards NS would suggest this occurs, at least in some
1619 cases, through genes moving towards either of these two hubs (top), but this might also
1620 occur through NS and/or perispeckle patterns moving or extending towards genes
1621 (middle), nucleating near genes (not shown), or a combination of gene and hub
1622 movements towards each other (bottom).
1623

1624

1625 **Supplementary Figure Legends:**

1626 **Supplementary Figure 1: Screening for proteins exhibiting perispeckle patterns**

1627 A: Representative protein candidates showing different categories of distributions within
1628 the interchromatin space (ICS). (Left to right) SRRM2: NS-enriched protein with no
1629 extended staining network in ICS; DDX39B: NS-enriched protein with additional
1630 extended staining network in ICS; protein concentration is highest within NS and lower
1631 in ICS network than within NS; THRAP3: protein concentrations are similar in and/or
1632 surrounding NS as the extended staining network in ICS; EIF4A3: protein concentration
1633 is present within NS but protein has a diffuse distribution, rather than a network-like
1634 staining pattern, within ICS; SAF-B: protein is largely absent within NS but shows an
1635 extended staining network not obviously correlated with NS within ICS. Each protein
1636 distribution is shown in grey (top row) and relative to NS (SON or SRRM2, magenta)
1637 (top 2 rows; scalebar: 5 μm). Regions highlighted within the whole nuclear images
1638 magnified to show protein distribution (grey) relative to NS (magenta; 3rd and 4th rows;
1639 scalebar: 1 μm). Pseudo-color images show the protein distribution segmented into
1640 "protein within NS" and "protein outside NS" fractions. Intensity plots (bottom row) show
1641 protein intensities over every percentile for "protein within NS" (blue) and "protein
1642 outside NS" (orange) fractions.

1643 B: Plot showing fraction of total protein intensity found outside NS. (n (number of nuclei)
1644 =3). Each point represents mean± standard deviation (SD).

1645 C: Plot showing fraction of nuclear area occupied by protein distribution outside NS (n
1646 (number of nuclei)=3). Each point represents mean±SD.

1647 D: Representative images of protein distributions all candidates surveyed in the
1648 screening ordered based on fraction of protein staining outside of NS (low to high).
1649 Pseudocolor intensity-mapped images (middle and right panels) highlight the lower
1650 intensity protein distributions seen within the ICS.
1651 E: Protein distributions segmented into “Protein within NS” and “Protein outside NS”
1652 intensity-mapped images for each candidate.
1653 F: PLRG1 colocalizes with THRAP3 in staining network outside of NS but is enriched
1654 within NS: Immunostaining of PLRG1(gray) along with endogenously tagged mCh-
1655 THRAP3 (magenta) U2OS cells. (Main image-scalebar: 5 μm; inset- scalebar: 1 μm).
1656 G: Cells expressing lentiviral mediated mCherry MAGOH (gray) immunostained with
1657 DDX39B (green) show colocalization of both proteins within ICS. (Main image-scalebar:
1658 5 μm; inset- scalebar: 1 μm).
1659 H: RNA FISH (using oligonucleotide probes) distribution for MALAT1 (grey) relative to
1660 THRAP3 (magenta) and DDX39B (green) immunostaining within the ICS. Second and
1661 fourth rows represent enlargements of boxed regions (white borders) from first and third
1662 rows, respectively. Apart from NS-enriched MALAT1, diffraction-limited spots of
1663 MALAT-1 are seen in the ICS in the vicinity of NS and show close spatial relationship to
1664 THRAP3 and DDX39B foci. Box plot showing fraction of RNA signal outside NS
1665 overlapping with THRAP3 or DDX39B signals. (n (number of nuclei) =10 for each
1666 comparison). White square represents mean and central line represents median value.
1667
1668 **Supplementary Figure 3: Transcriptional inhibition causes changes in perispeckle**
1669 **network PSTP.**

1670 A-B: Disruption of THRAP3 (magenta) network upon transcriptional inhibition also seen
1671 with Triptolide (A) and α-amanitin (B) treatments. NS marked by SON in yellow. The
1672 extent of disruption of the THRAP3 pattern after 2 hours of Triptolide and α-amanitin
1673 treatment resembles the disruption observed with 1 hour DRB treatment.
1674 C: Intensity-mapped images of THRAP3 (1st column) and DDX39B (3rd column) and
1675 their corresponding skeletons (2nd and 4th columns) upon treatment with 5,6-Dichloro-
1676 1-β-D-ribofuranosylbenzimidazole (DRB) comparing changes with DMSO control versus
1677 1 and 2 hours (h) of treatment.
1678 D: Multiple members of PSTP colocalize even as the networks are disrupted.
1679 Comparison of BCLAF1 (immunostaining, grey) and EGFP-THRAP3 (endogenous gene
1680 tagged, magenta) networks shows colocalization of BCLAF1 and THRAP3 as they are
1681 both disrupted upon DRB treatment (2 hours (h)). NS are marked by HaloTag-SON
1682 (endogenous gene tagged, yellow). Scale bar- 5 μm main image; 1 μm inset.
1683 E-F: Intensity mapped images and their corresponding skeletons of BCLAF1 (PSTP
1684 member) and RBM8A (PSDP member) upon DRB treatment as compared to DMSO
1685 shows similar disruption of PSTP network versus modest perturbation of PSDP network
1686 using staining against other PSTP (BCLAF1) and PSDP (RBM8A) components.
1687 G-H. Boxplots showing total skeleton length (G) (in pixels) and number of connections
1688 (H) of BCLAF1 (left, pink and magenta) and RBM8A (right, light and dark green) with
1689 DMSO or DRB treatment for 2 hours. n (number of nuclei) = 10-13 for each condition.
1690 One-way ANOVA with Tukey post-hoc test was used to calculate P-values. ns : $P > 0.05$; * : $P \leq 0.05$; ** : $P \leq 0.01$; *** : $P \leq 0.001$; **** : $P \leq 0.0001$.
1691
1692

1693 **Supplementary Figure 4: RNA Polymerase II foci associate closely with PSTP as**
1694 **compared to PSDP**
1695 A-B: Representative images of RNA Pol II foci (Ser5p top rows, Ser2- bottom rows)
1696 detected for distance measurements from THRAP3 (magenta, A) and DDX39B
1697 (magenta, B) and SON (green, B). Shown alongside are line profile plots of RNA Pol II
1698 foci relative to the three compartments. RNA Pol II foci appear to frequently localize
1699 adjacent to or overlapping with staining concentrations of THRAP3 and DDX39B, as
1700 seen by offset of their peaks with RNA pol II foci. Images on the right show segmented
1701 THRAP3 (top) and DDX39B (bottom) networks used for distance measurements of RNA
1702 Pol II foci. Circled foci colored based on distance: Red: <0.15 μm; Blue: >0.15 μm and
1703 <0.45 μm; Yellow: ≥0.45μm.
1704
1705 **Supplementary Figure 5: TSA-seq reveals gene expression hot-zones**
1706 **preferentially associate with PSTP and PSDP also in U2OS cells**
1707 A: Representative TSA-seq and Lamin B1 DamID tracks for chromosome 2 in U2OS
1708 cells: SON (blue), DDX39B (green), THRAP3 (magenta) and Lamin B1 DamID (grey).
1709 Yellow highlights mark Type I peaks and blue highlights mark Type II peaks.
1710 B: Heat map showing Pearson's correlation coefficients for SON, THRAP3 and DDX39B
1711 TSA-seq datasets (mean of two replicates) in U2OS cells.
1712 C: DNA-FISH (yellow) for Type I and Type II peaks (Apex) relative to SON (cyan) and
1713 THRAP3 (magenta) or DDX39B (green) and SRRM2 (blue). Type I regions are NS-
1714 associated and remain in contact with THRAP3 and DDX39B. Type II regions that are
1715 away from a NS are also in contact or close proximity of THRAP3 or DDX39B

1716 accumulations. Regions highlighted in white boxes are shown on the right as insets.
1717 Scale bars- 5 μm main image; 1 μm inset.
1718 D: Violin plots showing distance of DNA-FISH spots relative to SON, DDX39B and
1719 THRAP3 in U2OS cells. Central line indicates median distance and white square within
1720 the boxplot indicates mean distance. (n (alleles) as indicated: 126 (Type I) and 104
1721 (Type II) SON; 130 (Type I) and 106 (Type II) DDX39B; 126 (Type I) and 104 (Type II)
1722 THRAP3). One-way ANOVA with Tukey post-hoc test was used to calculate P-values.
1723 ns : $P > 0.05$; *** : $P \leq 0.001$; **** : $P \leq 0.0001$.
1724 E-G: Probability density plots for distance distribution of DNA-FISH spots relative to
1725 SON (E), DDX39B (F) and THRAP3 (G) for Type I (yellow) and Type II (blue) peaks in
1726 U2OS cells. (n (alleles) as indicated: 126 (Type I) and 104 (Type II) SON; 130 (Type I)
1727 and 106 (Type II) DDX39B; 126 (Type I) and 104 (Type II) THRAP3).
1728
1729 **Supplementary Figure 8: NS knockdown does not alter spatial positioning of**
1730 **genome relative to DDX39B and THRAP3 in HCT116 cells**
1731 A: Representative images showing mClover-SON (green) and SRRM2-mCherry
1732 (magenta) fluorescence intensities change over time with 5-Ph-IAA treatment for 0 min,
1733 2 hours or 4 hours.
1734 B: Heat map showing Pearson's correlation coefficients across WT HCT116 (SON,
1735 THRAP3, DDX39B) and HCT116 SON-SRRM2 degron cells (DMSO THRAP3, 5-Ph-
1736 IAA THRAP3, DMSO DDX39B, 5-Ph-IAA DDX39B) TSA-seq datasets.
1737 C: TSA-seq score tracks for chromosome 2 in HCT116 SON-SRRM2 degron cells: SON
1738 (TSA-seq score from WT cells; black shown for comparison) Type I (yellow highlights)

1739 and Type II Peaks (blue highlights). Normalized TSA-seq scores between DMSO-
1740 treated and 5-Ph-IAA-treated cells show small changes all over the entire chromosome
1741 for THRAP3 (magenta; negative residual; P-value in grey significant) and DDX39B
1742 (green; positive residual; P-value in grey not significant). P-value threshold set at log10
1743 scale at 2 (red line).
1744 D: Ideogram plots of all chromosomes in percentile change (DMSO-treated minus 5-Ph-
1745 IAA treated) in TSA-seq scores in HCT116 SON-SRRM2 degron cells for DDX39B (left)
1746 and THRAP3 (right) show little or no changes (-5 to +5 green) except for very few bins
1747 showing higher changes (indigo -20 / yellow +20).
1748 E: Scatterplots between mean TSA-seq scores of DMSO-treated and 5-Ph-IAA-treated
1749 DDX39B (green) and THRAP3 (magenta) show similar correlation coefficient as two
1750 individual replicates of DMSO-treated DDX39B (blue) and THRAP3 (yellow) TSA-seq.
1751
1752 **Supplementary Information**
1753 Supplementary Table 1: Reagent information (Primers, antibodies, oligolibraries and
1754 related information).
1755 1. cDNA constructs generated for screening: Primer sequences used for PCR
1756 amplification and restriction enzymes used for cloning
1757 2. Antibodies: Details and dilutions used
1758 3. CRISPR-Cas9 mediated gene tagging: Target specific gRNA sequences,
1759 homology arm sequences for Donor template generation and genotyping primers
1760 used.

4. Selected Type I and Type II genomic regions for FISH validation of TSA-seq in HCT116 and U2OS cells
5. Oligolibrary DNA-FISH probe sequences for 7 Type I peaks
6. Oligolibrary DNA-FISH probe sequences for 8 Type II peaks
7. Genomic coordinates of selected regions of Trajectory FISH of TypeI peak to nearest LAD or Type II peak to nearest LAD region
8. Oligolibrary DNA-FISH probe sequences for Apex of Type I peak
9. Oligolibrary DNA-FISH probe sequences for Arm regions of Type I trajectory
10. Oligolibrary DNA-FISH probe sequences for Apex of Type II peak
11. Oligolibrary DNA-FISH probe sequences for Arm regions of Type II trajectory
12. Human MALAT1 oligolibrary RNA-FISH probe sequences
13. Human MALAT1 Stellaris RNA-FISH probe sequences
14. 4DN Data Portal Accession numbers of TSA-seq datasets generated for this study.
15. 4DN Data Portal Accession numbers of RNA-seq generated for this study.

Supplementary Table 2: Complete list of significantly affected genes after nuclear speckle knockdown

Supplementary Videos

Video 1: Rapid dynamics of THRAP3 network in U2OS

A video of EGFP-THRAP3 (left, green) and its corresponding intensity mapping (right) in live U2OS cells showing THRAP3 non-diffuse accumulations forming, disappearing and

1784 reforming in the same space within tens of seconds. Images are acquired at 1 second
1785 intervals. Video is displayed at 5 frames per second. NS are marked by HaloTag-SON
1786 (left, magenta).
1787
1788 **Video 2: Dynamics of DDX39B network in U2OS cells**
1789 A representative video of mCherry-DDX39B (left, green) and its corresponding intensity
1790 mapping (right) in live U2OS cells showing connections of DDX39B forming and
1791 disappearing in the vicinity of NS marked by EGFP-SON (left, magenta). Images are
1792 acquired at 1 second intervals. (Gamma 0.8 used to display DDX39B). Video is
1793 displayed at 5 frames per second.
1794
1795 **Video 3: Perispeckle THRAP3 network remains stable over many hours within the**
1796 **interchromatin space**
1797 A video of mCherry-THRAP3 (magenta), EGFP-SON (yellow) and SiR-Hoechst DNA
1798 (cyan) imaged over 16 hours (h) at 40-minute intervals. THRAP3 network is dynamic
1799 but remains overall stable over time within the interchromatin space.
1800
1801 **Video 4: Perispeckle DDX39B network within the interchromatin space remains**
1802 **stable over many hours**
1803 A video of mCherry-DDX39B (magenta), EGFP-SON (yellow) and SiR-Hoechst DNA
1804 (cyan) imaged over 13 hours (h) at 10-minute intervals. DDX39B connections fluctuate
1805 but reappear within the same space over time making the overall network highly stable.
1806

1807 **Video 5: Transcriptional inhibition by 5,6-Dichloro-1-β-D**
1808 **ribofuranosylbenzimidazole (DRB) causes gradual disruption of THRAP3 network**
1809 A video of EGFP-THRAP3 (left, green) and HaloTag-SON (left, red) along with intensity
1810 mapping of THRAP3 (right) shows the network of THRAP3 collapses into nuclear
1811 speckles over the course of DRB treatment. Imaging was started 10 minutes (min) after
1812 adding DRB and images were taken every 2 minutes for up to 2 hours.
1813
1814 **Video 6: Live imaging of DDX39B upon nuclear speckle knockdown**
1815 Live-cell imaging of transiently expressed HaloTag-DDX39B (green, center) along with
1816 intensity mapping (right) and mClover-SON (in magenta, left) and SRRM2-mCherry in
1817 HCT116 cells shows DDX39B network is maintained even after double knockdown of
1818 SON and SRRM2 and complete loss of nuclear speckles. DDX39B also shows minimal
1819 changes to “speckle-like” structures corresponding to the concentration of DDX39B in
1820 regions originally occupied by the NS identified by SON and SRRM2 concentrations.
1821 Images were taken every 5 minutes (min) beginning 20 minutes after start of 5-Ph-IAA
1822 treatment.
1823
1824 **Data Availability**
1825 All the raw image data are available upon request. All TSA-seq and RNA-Seq datasets
1826 (raw and processed files) generated in this study are available at the 4DN Data Portal
1827 (see Supplementary Table 1 for ID numbers) and the GEO (GSE304818)
1828
1829 **Code Availability**

All custom scripts generated for this study are available on Github (https://github.com/nehacv93/PerispecklePatterns_partitionICS).

Author Contributions:

N.C.V. and A.S.B. conceived of and designed the study; N.C.V. performed most experiments and analyzed data including the screening, fixed-cell imaging, TSA-seq, oligo library design and DNA-FISH. N.C.V. and S.M. performed short timescale live-cell imaging of networks and DRB treatments. J.K. performed long term live-cell imaging, STORM and image analysis for the Pol II distribution and reporter transgene RNP distances relative to the networks. G.F. performed experiments of E6 and mini-Dys transgene RNPs and STED imaging. S.M. and N.C.V. replicated the transgene data set and also performed RNA-FISH for endogenous genes. Endogenous RNA-distance measurements were by N.C.V. and S.M. performed Mander's coefficient analysis. A.B. and M.K. generated and validated the SON-SRRM2 degron cell line. G.H., N.C.V., J.K. and S.M. made the endogenous fluorescent tagged cell lines by CRISPR-Cas9. P.C. performed FACS analysis of degron cell line and RNA-Seq analysis. N.C.V. performed TSA-seq and RNA-Seq correlation analyses. J.D. helped design and supervised the initial implementation of primary screen. K.Y.H. and Y.S.T provided reagents and supervision. N.C.V. and A.S.B. wrote the manuscript with inputs from other authors.

Acknowledgements:

This work was supported by the National Institutes of Health Common Fund 4D Nucleome Program grant U01DK127422 (ASB, KYH, YS) and also NIH R01GM058460

(ASB) and JSPS KAKENHI JP23H04925 and JP25H00979 (MTK) grants. We acknowledge assistance provided by the DNA Services, Roy J. Carver Biotechnology Center, University of Illinois at Urbana-Champaign for quality control on TSA-seq libraries, RNA-seq library construction, and sequencing (TSA-Seq and RNA-Seq libraries). Custom RNA-Seq scripts for processing and analysis of data were provided by the High-Performance Computing in Biology group (HPCBio), Roy J. Carver Biotechnology Center, University of Illinois at Urbana-Champaign. We thank Ratna Karatgi for advice regarding statistical analysis and Mishal Assif for assistance with image analysis.

REFERENCES:

Ahn, E.-Y., R.C. DeKelver, M.-C. Lo, T.A. Nguyen, S. Matsuura, A. Boyapati, S. Pandit, X.-D. Fu, and D.-E. Zhang. 2011. SON Controls Cell-Cycle Progression by Coordinated Regulation of RNA Splicing. *Mol. Cell*. 42:185–198. doi:10.1016/j.molcel.2011.03.014.

Ajuh, P. 2000. Functional analysis of the human CDC5L complex and identification of its components by mass spectrometry. *EMBO J.* 19:6569–6581. doi:10.1093/emboj/19.23.6569.

Alexander, K.A., A. Cote, S.C. Nguyen, L. Zhang, O. Gholamalamdari, P. Agudelo-Garcia, E. Lin-Shiao, K.M.A. Tanim, J. Lim, N. Biddle, M.C. Dunagin, C.R. Good, M.R. Mendoza, S.C. Little, A. Belmont, E.F. Joyce, A. Raj, and S.L. Berger. 2021. p53 mediates target gene association with nuclear speckles for amplified RNA expression. *Mol Cell*. 81:1666-1681 e6. doi:10.1016/j.molcel.2021.03.006.

Arun, G., D. Aggarwal, and D.L. Spector. 2020. MALAT1 Long Non-Coding RNA: Functional Implications. *Non-Coding RNA*. 6:22. doi:10.3390/ncrna6020022.

Barutcu, A.R., M. Wu, U. Braunschweig, B.J.A. Dyakov, Z. Luo, K.M. Turner, T. Durbic, Z.-Y. Lin, R.J. Weatheritt, P.G. Maass, A.-C. Gingras, and B.J. Blencowe. 2022. Systematic mapping of nuclear domain-associated transcripts reveals speckles and lamina as hubs of functionally distinct retained introns. *Mol. Cell*. 82:1035-1052.e9. doi:10.1016/j.molcel.2021.12.010.

Bates, M., B. Huang, G.T. Dempsey, and X. Zhuang. 2007. Multicolor Super-Resolution Imaging with Photo-Switchable Fluorescent Probes. *Science*. 317:1749–1753. doi:10.1126/science.1146598.

Bates, M., S.A. Jones, and X. Zhuang. 2013. Preparation of Photoswitchable Labeled Antibodies for STORM Imaging. *Cold Spring Harb. Protoc.* 2013:pdb.prot075168. doi:10.1101/pdb.prot075168.

Beliveau, B.J., A.N. Boettiger, G. Nir, B. Bintu, P. Yin, X. Zhuang, and C.-T. Wu. 2017. In Situ Super-Resolution Imaging of Genomic DNA with OligoSTORM and OligoDNA-PAINT. *Methods Mol. Biol. Clifton NJ*. 1663:231–252. doi:10.1007/978-1-4939-7265-4_19.

Beliveau, B.J., E.F. Joyce, N. Apostolopoulos, F. Yilmaz, C.Y. Fonseka, R.B. McCole, Y. Chang, J.B. Li, T.N. Senaratne, B.R. Williams, J.-M. Rouillard, and C. Wu. 2012. Versatile design and synthesis platform for visualizing genomes with Oligopaint FISH probes. *Proc. Natl. Acad. Sci.* 109:21301–21306. doi:10.1073/pnas.1213818110.

Bensaude, O. 2011. Inhibiting eukaryotic transcription. Which compound to choose? How to evaluate its activity?: Which compound to choose? How to evaluate its activity? *Transcription*. 2:103–108. doi:10.4161/trns.2.3.16172.

Bhat, P., A. Chow, B. Emert, O. Ettlin, S.A. Quinodoz, M. Strehle, Y. Takei, A. Burr, I.N. Goronzy, A.W. Chen, W. Huang, J.L.M. Ferrer, E. Soehalim, S.-T. Goh, T. Chari, D.K. Sullivan, M.R. Blanco, and M. Guttman. 2024. Genome organization around nuclear speckles drives mRNA splicing efficiency. *Nature*. 629:1165–1173. doi:10.1038/s41586-024-07429-6.

Björkman, A., S.L. Johansen, L. Lin, M. Schertzer, D.C. Kanellis, A.-M. Katsori, S.T. Christensen, Y. Luo, J.S. Andersen, S.J. Elsässer, A. Londono-Vallejo, J. Bartek, and K.B. Schou. 2020. Human RTEL1 associates with Poldip3 to facilitate responses to replication stress and R-loop resolution. *Genes Dev.* 34:1065–1074. doi:10.1101/gad.330050.119.

Bolte, S., and F.P. Cordelières. 2006. A guided tour into subcellular colocalization analysis in light microscopy. *J. Microsc.* 224:213–232. doi:10.1111/j.1365-2818.2006.01706.x.

Bradley, D., and G. Roth. 2007. Adaptive Thresholding using the Integral Image. *J. Graph. Tools*. 12:13–21. doi:10.1080/2151237X.2007.10129236.

Brody, Y., N. Neufeld, N. Bieberstein, S.Z. Causse, E.-M. Böhnlein, K.M. Neugebauer, X. Darzacq, and Y. Shav-Tal. 2011. The In Vivo Kinetics of RNA Polymerase II Elongation during Co-Transcriptional Splicing. *PLoS Biol.* 9:e1000573. doi:10.1371/journal.pbio.1000573.

Carter, K.C., D. Bowman, W. Carrington, K. Fogarty, J.A. McNeil, F.S. Fay, and J.B. Lawrence. 1993. A Three-Dimensional View of Precursor Messenger RNA Metabolism Within the Mammalian Nucleus. *Science*. 259:1330–1335. doi:10.1126/science.8446902.

Carter, K.C., K.L. Taneja, and J.B. Lawrence. 1991. Discrete nuclear domains of poly(A) RNA and their relationship to the functional organization of the nucleus. *J. Cell Biol.* 115:1191–1202. doi:10.1083/jcb.115.5.1191.

Chaturvedi, P., and A.S. Belmont. 2024. Nuclear speckle biology: At the cross-roads of discovery and functional analysis. *Curr. Opin. Cell Biol.* 91:102438. doi:10.1016/j.ceb.2024.102438.

Chen, Y., and A.S. Belmont. 2019. Genome organization around nuclear speckles. *Curr. Opin. Genet. Dev.* 55:91–99. doi:10.1016/j.gde.2019.06.008.

Chen, Y., Y. Zhang, Y. Wang, L. Zhang, E.K. Brinkman, S.A. Adam, R. Goldman, B. Van Steensel, J. Ma, and A.S. Belmont. 2018. Mapping 3D genome organization relative

1931 to nuclear compartments using TSA-Seq as a cytological ruler. *J. Cell Biol*.
1932 217:4025–4048. doi:10.1083/jcb.201807108.

1933 Choi, H., M. Kang, K.-H. Lee, and Y.-S. Kim. 2023. Elevated level of PLRG1 is critical for the
1934 proliferation and maintenance of genome stability of tumor cells. *BMB Rep*. 56:612–
1935 617. doi:10.5483/BMBRep.2023-0162.

1936 Chuang, T.-W., C.-C. Lu, C.-H. Su, P.-Y. Wu, S. Easwvaran, C.-C. Lee, H.-C. Kuo, K.-Y. Hung,
1937 K.-M. Lee, C.-Y. Tsai, and W.-Y. Tarn. 2019. The RNA Processing Factor Y14
1938 Participates in DNA Damage Response and Repair. *iScience*. 13:402–415.
1939 doi:10.1016/j.isci.2019.03.005.

1940 Chubb, J.R., S. Boyle, P. Perry, and W.A. Bickmore. 2002. Chromatin motion is constrained
1941 by association with nuclear compartments in human cells. *Curr Biol*. 12:439–45.

1942 Dias, A.P., K. Dufu, H. Lei, and R. Reed. 2010. A role for TREX components in the release of
1943 spliced mRNA from nuclear speckle domains. *Nat. Commun*. 1:97.
1944 doi:10.1038/ncomms1103.

1945 Dobin, A., C.A. Davis, F. Schlesinger, J. Drenkow, C. Zaleski, S. Jha, P. Batut, M. Chaisson,
1946 and T.R. Gingeras. 2013. STAR: ultrafast universal RNA-seq aligner. *Bioinformatics*.
1947 29:15–21. doi:10.1093/bioinformatics/bts635.

1948 Dopie, J., M.J. Sweredoski, A. Moradian, and A.S. Belmont. 2020. Tyramide signal
1949 amplification mass spectrometry (TSA-MS) ratio identifies nuclear speckle proteins.
1950 *J. Cell Biol*. 219:e201910207. doi:10.1083/jcb.201910207.

1951 Egloff, S., and S. Murphy. 2008. Cracking the RNA polymerase II CTD code. *Trends Genet*.
1952 24:280–288. doi:10.1016/j.tig.2008.03.008.

1953 Ester, M., H.-P. Kriegel, J. Sander, and X. Xu. 1996. A density-based algorithm for discovering
1954 clusters in large spatial databases with noise. *In* Proceedings of the Second
1955 International Conference on Knowledge Discovery and Data Mining. AAAI Press,
1956 Portland, Oregon. 226–231.

1957 Fan, J., B. Kuai, K. Wang, L. Wang, Y. Wang, X. Wu, B. Chi, G. Li, and H. Cheng. 2018. mRNAs
1958 are sorted for export or degradation before passing through nuclear speckles.
1959 *Nucleic Acids Res*. 46:8404–8416. doi:10.1093/nar/gky650.

1960 Fei, J., M. Jadaliha, T.S. Harmon, I.T.S. Li, B. Hua, Q. Hao, A.S. Holehouse, M. Reyer, Q. Sun,
1961 S.M. Freier, R.V. Pappu, K.V. Prasanth, and T. Ha. 2017. Quantitative analysis of
1962 multilayer organization of proteins and RNA in nuclear speckles at super resolution.
1963 *J. Cell Sci*. 130:4180–4192. doi:10.1242/jcs.206854.

Gatfield, D., H. Le Hir, C. Schmitt, I.C. Braun, T. Köcher, M. Wilm, and E. Izaurralde. 2001. The DExH/D box protein HEL/UAP56 is essential for mRNA nuclear export in Drosophila. *Curr. Biol.* 11:1716–1721. doi:10.1016/S0960-9822(01)00532-2.

Gholamalamdari, O., T. Van Schaik, Y. Wang, P. Kumar, L. Zhang, Y. Zhang, G.A.H. Gonzalez, A.E. Vouzas, P.A. Zhao, D.M. Gilbert, J. Ma, B. Van Steensel, and A.S. Belmont. 2025. Beyond A and B Compartments: how major nuclear locales define nuclear genome organization and function. doi:10.7554/eLife.99116.2.

Hall, L.L., K.P. Smith, M. Byron, and J.B. Lawrence. 2006. Molecular anatomy of a speckle. *Anat Rec Discov Mol Cell Evol Biol*. 288:664–75.

Harris, C.R., K.J. Millman, S.J. Van Der Walt, R. Gommers, P. Virtanen, D. Cournapeau, E. Wieser, J. Taylor, S. Berg, N.J. Smith, R. Kern, M. Picus, S. Hoyer, M.H. Van Kerkwijk, M. Brett, A. Haldane, J.F. Del Río, M. Wiebe, P. Peterson, P. Gérard-Marchant, K. Sheppard, T. Reddy, W. Weckesser, H. Abbasi, C. Gohlke, and T.E. Oliphant. 2020. Array programming with NumPy. *Nature*. 585:357–362. doi:10.1038/s41586-020-2649-2.

Hermanson, G.T. 2013. Bioconjugate Techniques. Third edition. Academic Press, an imprint of Elsevier, Amsterdam Boston Heidelberg. 1 pp.

Hondele, M., R. Sachdev, S. Heinrich, J. Wang, P. Vallotton, B.M.A. Fontoura, and K. Weis. 2019. DEAD-box ATPases are global regulators of phase-separated organelles. *Nature*. 573:144–148. doi:10.1038/s41586-019-1502-y.

Hu, Y., I. Kireev, M. Plutz, N. Ashourian, and A.S. Belmont. 2009. Large-scale chromatin structure of inducible genes: transcription on a condensed, linear template. *J. Cell Biol.* 185:87–100. doi:10.1083/jcb.200809196.

Hunter, J.D. 2007. Matplotlib: A 2D Graphics Environment. *Comput. Sci. Eng.* 9:90–95. doi:10.1109/mcse.2007.55.

Iborra, F.J., A. Pombo, D.A. Jackson, and P.R. Cook. 1996. Active RNA polymerases are localized within discrete transcription ‘factories’ in human nuclei. *J. Cell Sci.* 109:1427–1436. doi:10.1242/jcs.109.6.1427.

Ilik, İ.A., M. Malszycki, A.K. Lübke, C. Schade, D. Meierhofer, and T. Aktaş. 2020. SON and SRRM2 are essential for nuclear speckle formation. *eLife*. 9:e60579. doi:10.7554/eLife.60579.

Irgen-Gioro, S., S. Yoshida, V. Walling, and S. Chong. 2022. Fixation can change the appearance of phase separation in living cells. *eLife*. 11:e79903. doi:10.7554/eLife.79903.

Ito, M., C.-X. Yuan, S. Malik, W. Gu, J.D. Fondell, S. Yamamura, Z.-Y. Fu, X. Zhang, J. Qin, and R.G. Roeder. 1999. Identity between TRAP and SMCC Complexes Indicates Novel Pathways for the Function of Nuclear Receptors and Diverse Mammalian Activators. *Mol. Cell*. 3:361–370. doi:10.1016/S1097-2765(00)80463-3.

Jackson, D.A., A.B. Hassan, R.J. Errington, and P.R. Cook. 1993. Visualization of focal sites of transcription within human nuclei. *EMBO J.* 12:1059–1065. doi:10.1002/j.1460-2075.1993.tb05747.x.

JavanMoghadam-Kamrani, S., and K. Keyomarsi. 2008. Synchronization of the cell cycle using Lovastatin. *Cell Cycle*. 7:2434–2440. doi:10.4161/cc.6364.

Jensen, T.H., J. Boulay, M. Rosbash, and D. Libri. 2001. The DECD box putative ATPase Sub2p is an early mRNA export factor. *Curr. Biol.* 11:1711–1715. doi:10.1016/S0960-9822(01)00529-2.

Joo, J., S. Cho, S. Hong, S. Min, K. Kim, R. Kumar, J.-M. Choi, Y. Shin, and I. Jung. 2023. Probabilistic establishment of speckle-associated inter-chromosomal interactions. *Nucleic Acids Res.* 51:5377–5395. doi:10.1093/nar/gkad211.

Kang, H.J., H. Eom, H. Kim, K. Myung, H.M. Kwon, and J.H. Choi. 2021. Thrap3 promotes R-loop resolution via interaction with methylated DDX5. *Exp. Mol. Med.* 53:1602–1611. doi:10.1038/s12276-021-00689-6.

Khanna, N., Y. Hu, and A.S. Belmont. 2014. HSP70 transgene directed motion to nuclear speckles facilitates heat shock activation. *Curr. Biol. CB*. 24:1138–44. doi:10.1016/j.cub.2014.03.053.

Khyzha, N., K. Ahmad, and S. Henikoff. 2025. Profiling transcriptome composition and dynamics within nuclear compartments using SLAM-RT&Tag. *Mol. Cell*. 85:1366-1380.e4. doi:10.1016/j.molcel.2025.02.012.

Kim, J., G.A.H. Gonzalez, N.C. Venkata, K.Y. Han, and A.S. Belmont. 2025. Nonrandom interchromatin trafficking through dynamic multiphase speckle connections. doi:10.1101/2025.05.23.655761.

Kim, J., K.Y. Han, N. Khanna, T. Ha, and A.S. Belmont. 2019. Nuclear speckle fusion via long-range directional motion regulates speckle morphology after transcriptional inhibition. *J. Cell Sci.* jcs.226563. doi:10.1242/jcs.226563.

Kim, J., N.C. Venkata, G.A. Hernandez Gonzalez, N. Khanna, and A.S. Belmont. 2020. Gene expression amplification by nuclear speckle association. *J Cell Biol*. 219. doi:10.1083/jcb.201904046.

Kleinridders, A., H.-M. Pogoda, S. Irlenbusch, N. Smyth, C. Koncz, M. Hammerschmidt, and J.C. Brüning. 2009. PLRG1 Is an Essential Regulator of Cell Proliferation and

2033 Apoptosis during Vertebrate Development and Tissue Homeostasis. *Mol. Cell. Biol.*
2034 29:3173–3185. doi:10.1128/MCB.01807-08.

2035 Kota, K.P., S.R. Wagner, E. Huerta, J.M. Underwood, and J.A. Nickerson. 2008. Binding of
2036 ATP to UAP56 is necessary for mRNA export. *J. Cell Sci.* 121:1526–1537.
2037 doi:10.1242/jcs.021055.

2038 Kumar, P., O. Gholamalamdari, Y. Zhang, L. Zhang, A. Vertii, T. Van Schaik, D. Peric-Hupkes,
2039 T. Sasaki, D.M. Gilbert, B. Van Steensel, J. Ma, P.D. Kaufman, and A.S. Belmont.
2040 2024. Nucleolus and centromere Tyramide Signal Amplification-Seq reveals variable
2041 localization of heterochromatin in different cell types. *Commun. Biol.* 7:1135.
2042 doi:10.1038/s42003-024-06838-7.

2043 Lafontaine, D.L.J., J.A. Riback, R. Bascetin, and C.P. Brangwynne. 2021. The nucleolus as a
2044 multiphase liquid condensate. *Nat. Rev. Mol. Cell Biol.* 22:165–182.
2045 doi:10.1038/s41580-020-0272-6.

2046 Lee, K.-M., I.-W. Hsu, and W.-Y. Tarn. 2010. TRAP150 activates pre-mRNA splicing and
2047 promotes nuclear mRNA degradation. *Nucleic Acids Res.* 38:3340–3350.
2048 doi:10.1093/nar/gkq017.

2049 Lee, K.-M., and W.-Y. Tarn. 2014. TRAP150 activates splicing in composite terminal exons.
2050 *Nucleic Acids Res.* 42:12822–12832. doi:10.1093/nar/gku963.

2051 Levi, V., Q. Ruan, M. Plutz, A.S. Belmont, and E. Gratton. 2005. Chromatin Dynamics in
2052 Interphase Cells Revealed by Tracking in a Two-Photon Excitation Microscope.
2053 *Biophys J*. 89:4275–4285. doi:10.1529/biophysj.105.066670.

2054 Li, Y., M. Mund, P. Hoess, J. Deschamps, U. Matti, B. Nijmeijer, V.J. Sabinina, J. Ellenberg, I.
2055 Schoen, and J. Ries. 2018. Real-time 3D single-molecule localization using
2056 experimental point spread functions. *Nat. Methods*. 15:367–369.
2057 doi:10.1038/nmeth.4661.

2058 Llères, D., M. Denegri, M. Biggiogera, P. Ajuh, and A.I. Lamond. 2010. Direct interaction
2059 between hnRNP-M and CDC5L/PLRG1 proteins affects alternative splice site
2060 choice. *EMBO Rep.* 11:445–451. doi:10.1038/embor.2010.64.

2061 Love, M.I., W. Huber, and S. Anders. 2014. Moderated estimation of fold change and
2062 dispersion for RNA-seq data with DESeq2. *Genome Biol.* 15. doi:10.1186/s13059-
2063 014-0550-8.

2064 Luo, M.-J., Z. Zhou, K. Magni, C. Christoforides, J. Rappsilber, M. Mann, and R. Reed. 2001.
2065 Pre-mRNA splicing and mRNA export linked by direct interactions between UAP56
2066 and Aly. *Nature*. 413:644–647. doi:10.1038/35098106.

Marshall, W.F., A. Straight, J.F. Marko, J. Swedlow, A. Dernburg, A. Belmont, A.W. Murray, D.A. Agard, and J.W. Sedat. 1997. Interphase chromosomes undergo constrained diffusional motion in living cells. *Curr Biol*. 7:930–9.

Martin, S., and A. Pombo. 2003. Transcription factories: quantitative studies of nanostructures in the mammalian nucleus. *Chromosome Res.* 11:461–470. doi:10.1023/A:1024926710797.

Miao, H., F. Wu, Y. Li, C. Qin, Y. Zhao, M. Xie, H. Dai, H. Yao, H. Cai, Q. Wang, X. Song, and L. Li. 2022. MALAT1 modulates alternative splicing by cooperating with the splicing factors PTBP1 and PSF. *Sci. Adv.* 8. doi:10.1126/sciadv.abq7289.

Mor, A., S. Suliman, R. Ben-Yishay, S. Yunger, Y. Brody, and Y. Shav-Tal. 2010. Dynamics of single mRNP nucleocytoplasmic transport and export through the nuclear pore in living cells. *Nat. Cell Biol.* 12:543–552. doi:10.1038/ncb2056.

Nguyen, V. 1996. In vivo degradation of RNA polymerase II largest subunit triggered by alpha-amanitin. *Nucleic Acids Res.* 24:2924–2929. doi:10.1093/nar/24.15.2924.

Otsu, N. 1979. A Threshold Selection Method from Gray-Level Histograms. *IEEE Trans. Syst. Man Cybern.* 9:62–66. doi:10.1109/tsmc.1979.4310076.

Pérez-Calero, C., A. Bayona-Feliu, X. Xue, S.I. Barroso, S. Muñoz, V.M. González-Basallote, P. Sung, and A. Aguilera. 2020. UAP56/DDX39B is a major cotranscriptional RNA–DNA helicase that unwinds harmful R loops genome-wide. *Genes Dev.* 34:898–912. doi:10.1101/gad.336024.119.

Pombo, A. 1999. Regional specialization in human nuclei: visualization of discrete sites of transcription by RNA polymerase III. *EMBO J.* 18:2241–2253. doi:10.1093/emboj/18.8.2241.

Pontén, F., M. Gry, L. Fagerberg, E. Lundberg, A. Asplund, L. Berglund, P. Oksvold, E. Björling, S. Hober, C. Kampf, S. Navani, P. Nilsson, J. Ottosson, A. Persson, H. Wernérus, K. Wester, and M. Uhlén. 2009. A global view of protein expression in human cells, tissues, and organs. *Mol. Syst. Biol.* 5:337. doi:10.1038/msb.2009.93.

Quinodoz, S.A., N. Ollikainen, B. Tabak, A. Palla, J.M. Schmidt, E. Detmar, M.M. Lai, A.A. Shishkin, P. Bhat, Y. Takei, V. Trinh, E. Aznauryan, P. Russell, C. Cheng, M. Jovanovic, A. Chow, L. Cai, P. McDonel, M. Garber, and M. Guttman. 2018. Higher-Order Inter-chromosomal Hubs Shape 3D Genome Organization in the Nucleus. *Cell*. 174:744-757 e24. doi:10.1016/j.cell.2018.05.024.

Ries, J. 2020. SMAP: a modular super-resolution microscopy analysis platform for SMLM data. *Nat. Methods*. 17:870–872. doi:10.1038/s41592-020-0938-1.

Schindelin, J., I. Arganda-Carreras, E. Frise, V. Kaynig, M. Longair, T. Pietzsch, S. Preibisch, C. Rueden, S. Saalfeld, B. Schmid, J.-Y. Tinevez, D.J. White, V. Hartenstein, K. Eliceiri, P. Tomancak, and A. Cardona. 2012. Fiji: an open-source platform for biological-image analysis. *Nat. Methods*. 9:676–682. doi:10.1038/nmeth.2019.

Shang, Y., T. Jiang, L. Ran, W. Hu, Y. Wu, J. Ye, Z. Peng, L. Chen, and R. Wang. 2022. TET2–BCLAF1 transcription repression complex epigenetically regulates the expression of colorectal cancer gene Ascl2 via methylation of its promoter. *J. Biol. Chem*. 298:102095. doi:10.1016/j.jbc.2022.102095.

Sharma, A., H. Takata, K. Shibahara, A. Bubulya, and P.A. Bubulya. 2010. Son Is Essential for Nuclear Speckle Organization and Cell Cycle Progression. *Mol. Biol. Cell*. 21:650–663. doi:10.1091/mbc.e09-02-0126.

Shen, H., X. Zheng, J. Shen, L. Zhang, R. Zhao, and M.R. Green. 2008. Distinct activities of the DExD/H-box splicing factor hUAP56 facilitate stepwise assembly of the spliceosome. *Genes Dev.* 22:1796–1803. doi:10.1101/gad.1657308.

Smith, K.P., L.L. Hall, and J.B. Lawrence. 2020. Nuclear hubs built on RNAs and clustered organization of the genome. *Curr. Opin. Cell Biol*. 64:67–76. doi:10.1016/j.ceb.2020.02.015.

Smith, K.P., P.T. Moen, K.L. Wydner, J.R. Coleman, and J.B. Lawrence. 1999. Processing of endogenous pre-mRNAs in association with SC-35 domains is gene specific. *J Cell Biol*. 144:617–29.

Solovei, I., and M. Cremer. 2010. 3D-FISH on cultured cells combined with immunostaining. *Methods Mol. Biol. Clifton NJ*. 659:117–126. doi:10.1007/978-1-60761-789-1_8.

Spector, D.L., and A.I. Lamond. 2011. Nuclear Speckles. *Cold Spring Harb. Perspect. Biol.* 3:a000646–a000646. doi:10.1101/cshperspect.a000646.

Su, J.H., P. Zheng, S.S. Kinrot, B. Bintu, and X. Zhuang. 2020. Genome-Scale Imaging of the 3D Organization and Transcriptional Activity of Chromatin. *Cell*. 182:1641-1659 e26. doi:10.1016/j.cell.2020.07.032.

Takei, Y., Y. Yang, J. White, J. Yun, M. Prasad, L.J. Ombelets, S. Schindler, and L. Cai. 2023. High-resolution spatial multi-omics reveals cell-type specific nuclear compartments. 2023.05.07.539762. doi:10.1101/2023.05.07.539762.

Takei, Y., J. Yun, S. Zheng, N. Ollikainen, N. Pierson, J. White, S. Shah, J. Thomassie, S. Suo, C.L. Eng, M. Guttman, G.C. Yuan, and L. Cai. 2021. Integrated spatial genomics reveals global architecture of single nuclei. *Nature*. 590:344–350. doi:10.1038/s41586-020-03126-2.

Taniguchi, I., and M. Ohno. 2008. ATP-Dependent Recruitment of Export Factor Aly/REF onto Intronless mRNAs by RNA Helicase UAP56. *Mol. Cell. Biol.* 28:601–608. doi:10.1128/MCB.01341-07.

Titov, D.V., B. Gilman, Q.-L. He, S. Bhat, W.-K. Low, Y. Dang, M. Smeaton, A.L. Demain, P.S. Miller, J.F. Kugel, J.A. Goodrich, and J.O. Liu. 2011. XPB, a subunit of TFIIH, is a target of the natural product triptolide. *Nat. Chem. Biol.* 7:182–188. doi:10.1038/nchembio.522.

Van Der Walt, S., J.L. Schönberger, J. Nunez-Iglesias, F. Boulogne, J.D. Warner, N. Yager, E. Gouillart, and T. Yu. 2014. scikit-image: image processing in Python. *PeerJ*. 2:e453. doi:10.7717/peerj.453.

Varia, S., D. Potabathula, Z. Deng, A. Bubulya, and P.A. Bubulya. 2013. Btf and TRAP150 have distinct roles in regulating subcellular mRNA distribution. *Nucleus*. 4:229–240. doi:10.4161/nucl.25187.

Vohhodina, J., E.M. Barros, A.L. Savage, F.G. Liberante, L. Manti, P. Bankhead, N. Cosgrove, A.F. Madden, D.P. Harkin, and K.I. Savage. 2017. The RNA processing factors THRAP3 and BCLAF1 promote the DNA damage response through selective mRNA splicing and nuclear export. *Nucleic Acids Res.* 45:12816–12833. doi:10.1093/nar/gkx1046.

Wang, K., L. Wang, J. Wang, S. Chen, M. Shi, and H. Cheng. 2018. Intronless mRNAs transit through nuclear speckles to gain export competence. *J. Cell Biol.* 217:3912–3929. doi:10.1083/jcb.201801184.

Wang, Y., Y. Zhang, R. Zhang, T. van Schaik, L. Zhang, T. Sasaki, D. Peric-Hupkes, Y. Chen, D.M. Gilbert, B. van Steensel, A.S. Belmont, and J. Ma. 2021. SPIN reveals genome-wide landscape of nuclear compartmentalization. *Genome Biol*. 22:36. doi:10.1186/s13059-020-02253-3.

Wu, J., Y. Xiao, Y. Liu, L. Wen, C. Jin, S. Liu, S. Paul, C. He, O. Regev, and J. Fei. 2024. Dynamics of RNA localization to nuclear speckles are connected to splicing efficiency. *Sci. Adv.* 10:eadp7727. doi:10.1126/sciadv.adp7727.

Xie, S.Q., S. Martin, P.V. Guillot, D.L. Bentley, and A. Pombo. 2006. Splicing Speckles Are Not Reservoirs of RNA Polymerase II, but Contain an Inactive Form, Phosphorylated on Serine[2] Residues of the C-Terminal Domain. *Mol. Biol. Cell*. 17:1723–1733. doi:10.1091/mbc.e05-08-0726.

Xie, Y., S. Gao, K. Zhang, P. Bhat, B.P. Clarke, K. Batten, M. Mei, M. Gazzara, J.W. Shay, K.W. Lynch, A.E. Angelos, P.S. Hill, A.L. Ivey, B.M.A. Fontoura, and Y. Ren. 2023. Structural basis for high-order complex of SARNP and DDX39B to facilitate mRNP assembly. *Cell Rep.* 42:112988. doi:10.1016/j.celrep.2023.112988.

Xu, Z., X. Li, H. Li, C. Nie, W. Liu, S. Li, Z. Liu, W. Wang, and J. Wang. 2020. Suppression of DDX39B sensitizes ovarian cancer cells to DNA-damaging chemotherapeutic agents via destabilizing BRCA1 mRNA. *Oncogene*. 39:7051–7062. doi:10.1038/s41388-020-01482-x.

Yankulov, K., K. Yamashita, R. Roy, J.-M. Egly, and D.L. Bentley. 1995. The Transcriptional Elongation Inhibitor 5,6-Dichloro-1-β-D-ribofuranosylbenzimidazole Inhibits Transcription Factor IIH-associated Protein Kinase. *J. Biol. Chem.* 270:23922–23925. doi:10.1074/jbc.270.41.23922.

Yesbolatova, A., Y. Saito, N. Kitamoto, H. Makino-Itou, R. Ajima, R. Nakano, H. Nakaoka, K. Fukui, K. Gamo, Y. Tominari, H. Takeuchi, Y. Saga, K. Hayashi, and M.T. Kanemaki. 2020. The auxin-inducible degron 2 technology provides sharp degradation control in yeast, mammalian cells, and mice. *Nat. Commun.* 11. doi:10.1038/s41467-020-19532-z.

Yu, C.-L., T.-W. Chuang, S.Y. Samuel, Y.-C. Lou, and W.-Y. Tarn. 2023a. Co-phase separation of Y14 and RNA in vitro and its implication for DNA repair. *RNA*. 29:1007–1019. doi:10.1261/rna.079514.122.

Yu, R., S. Roseman, A.P. Siegenfeld, S.C. Nguyen, E.F. Joyce, B.B. Liau, I.D. Krantz, K.A. Alexander, and S.L. Berger. 2023b. CTCF/cohesin organize the ground state of chromatin-nuclear speckle association. 2023.07.22.550178. doi:10.1101/2023.07.22.550178.

Zhang, L., Y. Chen, and A.S. Belmont. 2022. Measuring Cytological Proximity of Chromosomal Loci to Defined Nuclear Compartments with TSA-seq. *In* Spatial Genome Organization. T. Sexton, editor. Springer US, New York, NY. 145–186.

Zhang, L., Y. Zhang, Y. Chen, O. Gholamalamdari, Y. Wang, J. Ma, and A.S. Belmont. 2021. TSA-seq reveals a largely conserved genome organization relative to nuclear speckles with small position changes tightly correlated with gene expression changes. *Genome Res.* 31:251–264. doi:10.1101/gr.266239.120.

Zhang, M., Z. Gu, S. Guo, Y. Sun, S. Ma, S. Yang, J. Guo, C. Fang, L. Shu, Y. Ge, Z. Chen, and B. Wang. 2024. SRRM2 phase separation drives assembly of nuclear speckle subcompartments. *Cell Rep.* 43:113827. doi:10.1016/j.celrep.2024.113827.

Zhang, N., R. Kaur, S. Akhter, and R.J. Legerski. 2009. Cdc5L interacts with ATR and is required for the S-phase cell-cycle checkpoint. *EMBO Rep.* 10:1029–1035. doi:10.1038/embor.2009.122.

Zhang, N., R. Kaur, X. Lu, X. Shen, L. Li, and R.J. Legerski. 2005. The Pso4 mRNA Splicing and DNA Repair Complex Interacts with WRN for Processing of DNA Interstrand Cross-links. *J. Biol. Chem.* 280:40559–40567. doi:10.1074/jbc.M508453200.

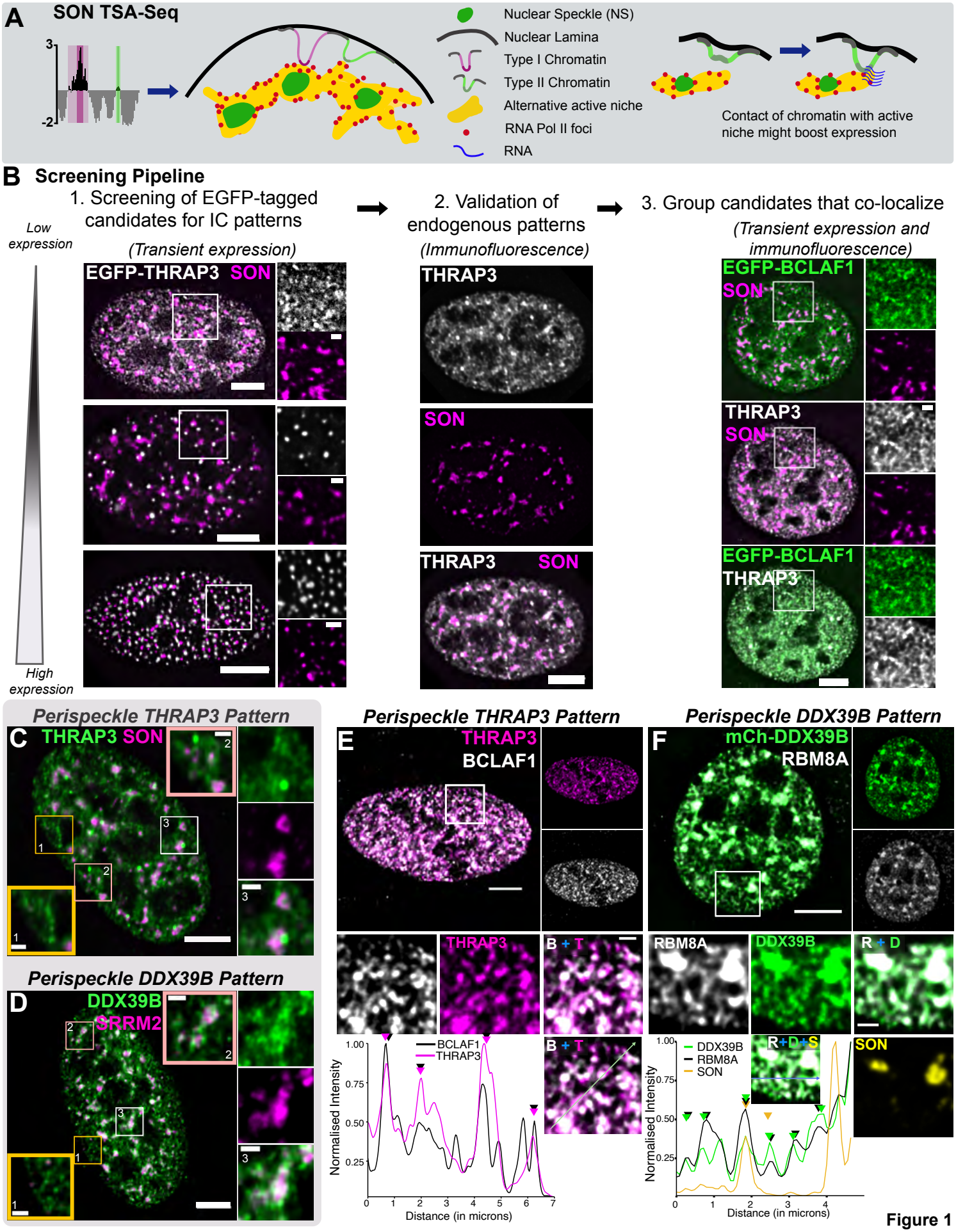
A
SON TSA-Seq
3
-2
Nuclear Speckle (NS)
Nuclear Lamina
Type I Chromatin
Type II Chromatin
Alternative active niche
RNA Pol II foci
RNA
Contact of chromatin with active niche might boost expression
B
Screening Pipeline
1. Screening of EGFP-tagged candidates for IC patterns
(Transient expression)
Low expression
High expression
EGFP-THRAP3 SON
2. Validation of endogenous patterns
(Immunofluorescence)
THRAP3
SON
THRAP3 SON
3. Group candidates that co-localize
(Transient expression and immunofluorescence)
EGFP-BCLAF1
SON
THRAP3
SON
EGFP-BCLAF1
THRAP3
Perispeckle THRAP3 Pattern
C
THRAP3 SON
Perispeckle DDX39B Pattern
D
DDX39B
SRRM2
Perispeckle THRAP3 Pattern
E
THRAP3
BCLAF1
THRAP3
B + T
BCLAF1
THRAP3
Normalised Intensity
Distance (in microns)
Perispeckle DDX39B Pattern
F
mCh-DDX39B
RBM8A
RBM8A
DDX39B
R + D
R+D+S
SON
DDX39B
RBM8A
SON
Normalised Intensity
Distance (in microns)

Figure 1

Single connection: Dynamic over seconds

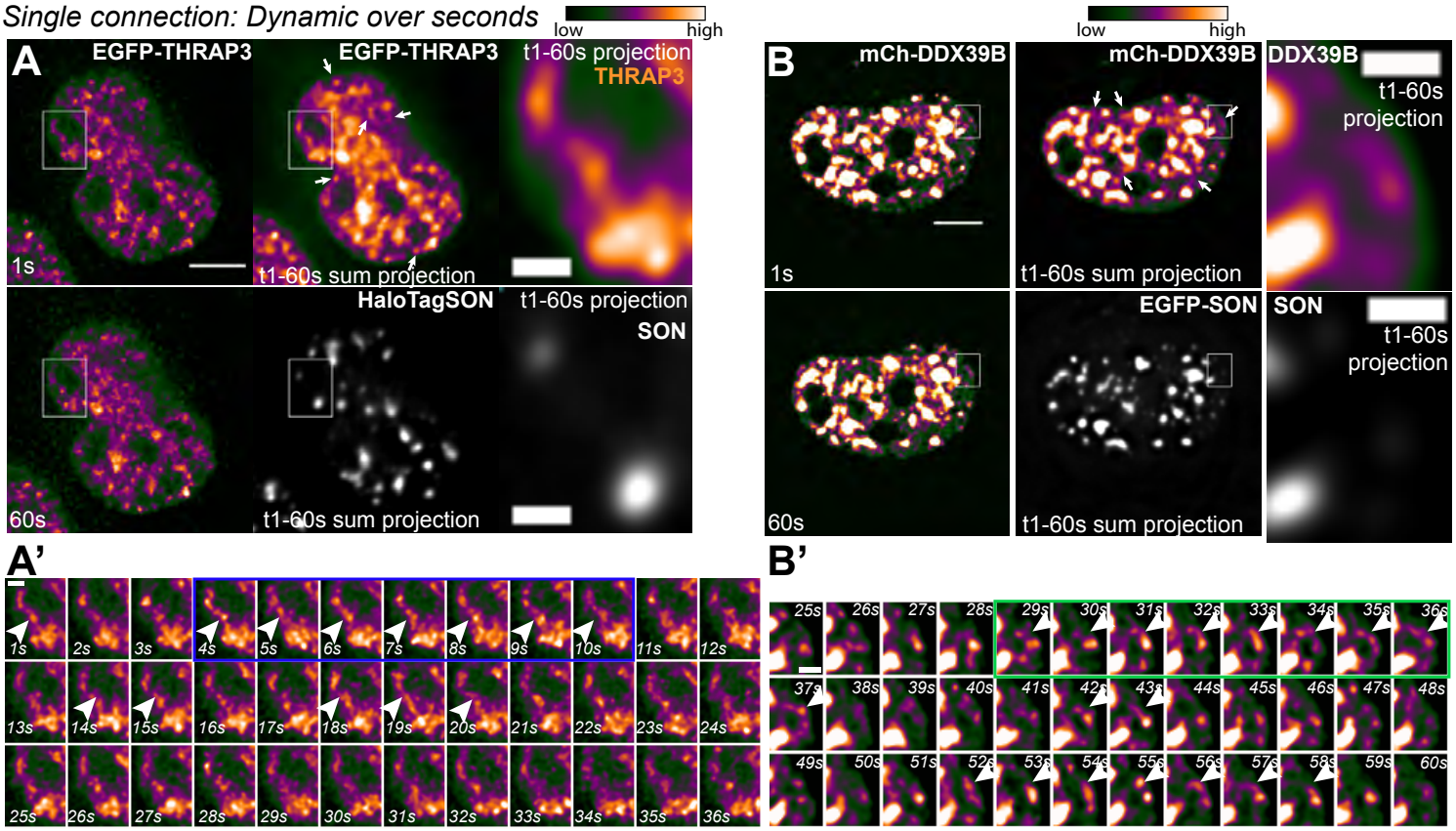

Network: Stable over hours

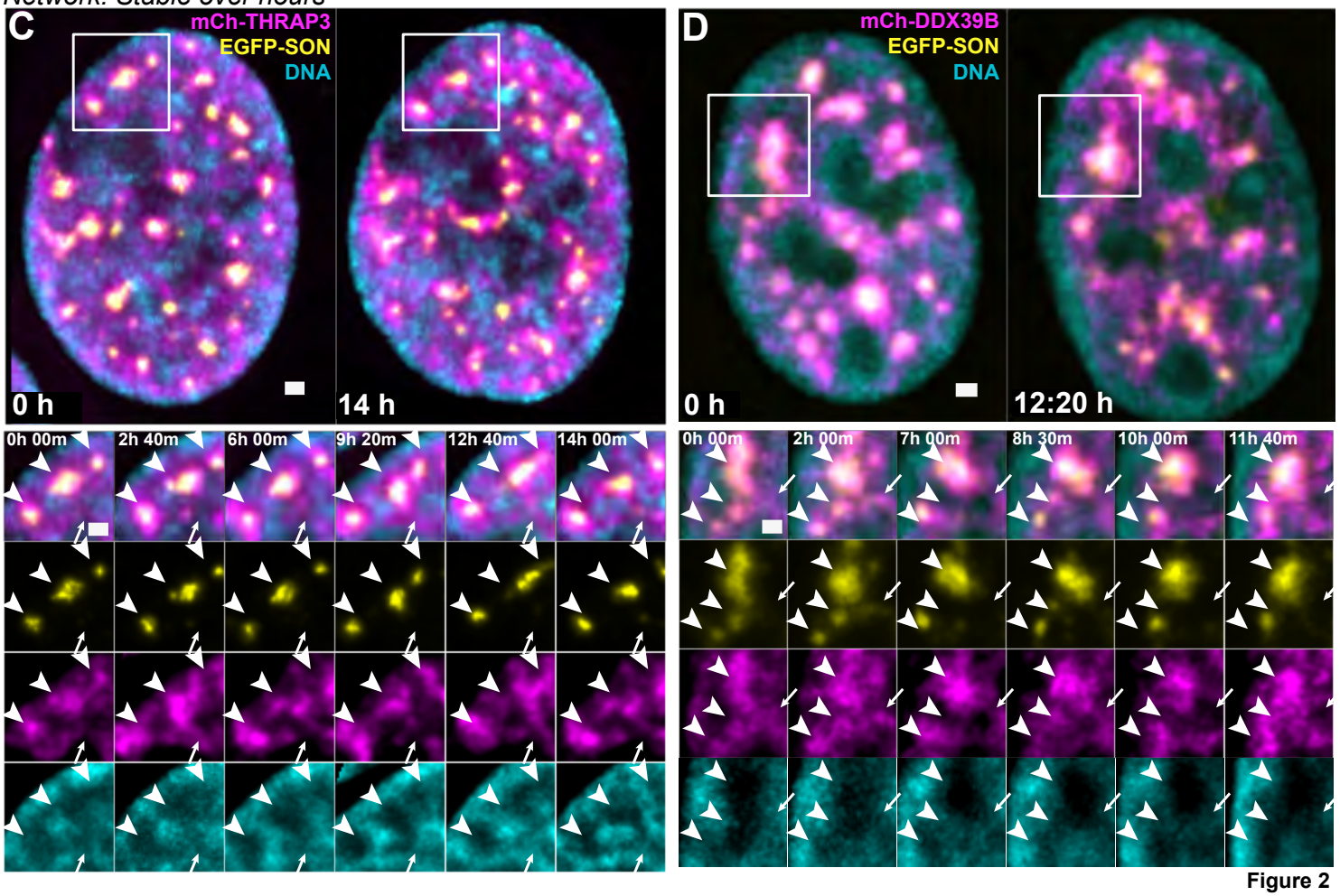

Figure 2

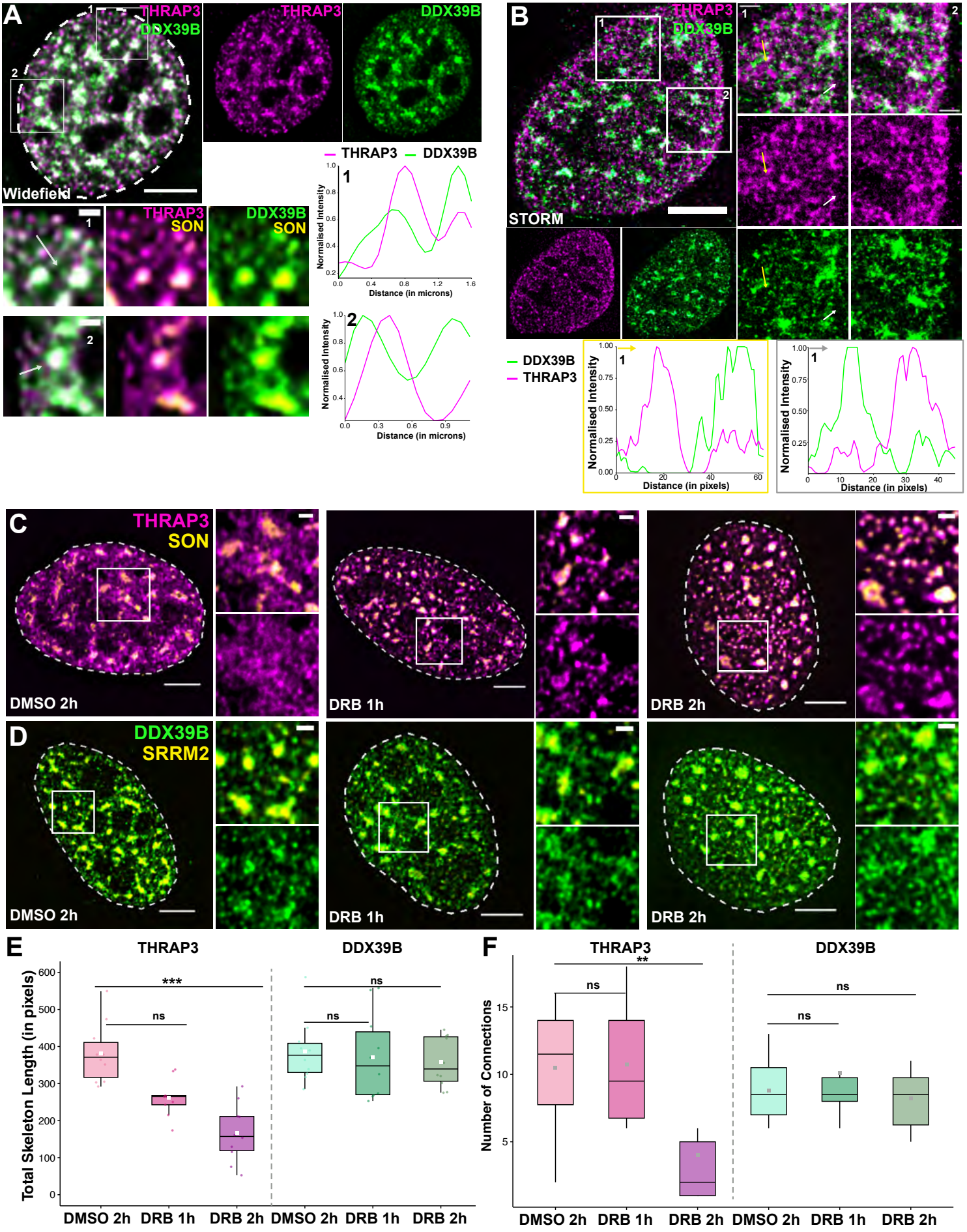
A
THRAP3
DDX39B
Widefield
THRAP3
DDX39B
THRAP3
SON
DDX39B
SON
THRAP3
DDX39B
Normalised Intensity
Distance (in microns)
B
THRAP3
DDX39B
STORM
DDX39B
THRAP3
Normalised Intensity
Distance (in pixels)
C
THRAP3
SON
DMSO 2h
DRB 1h
DRB 2h
D
DDX39B
SRRM2
DMSO 2h
DRB 1h
DRB 2h
E
THRAP3
DDX39B
Total Skeleton Length (in pixels)
***
ns
ns
ns
DMSO 2h
DRB 1h
DRB 2h
DMSO 2h
DRB 1h
DRB 2h
F
THRAP3
DDX39B
Number of Connections
**
ns
ns
ns
DMSO 2h
DRB 1h
DRB 2h
DMSO 2h
DRB 1h
DRB 2h

Figure 3

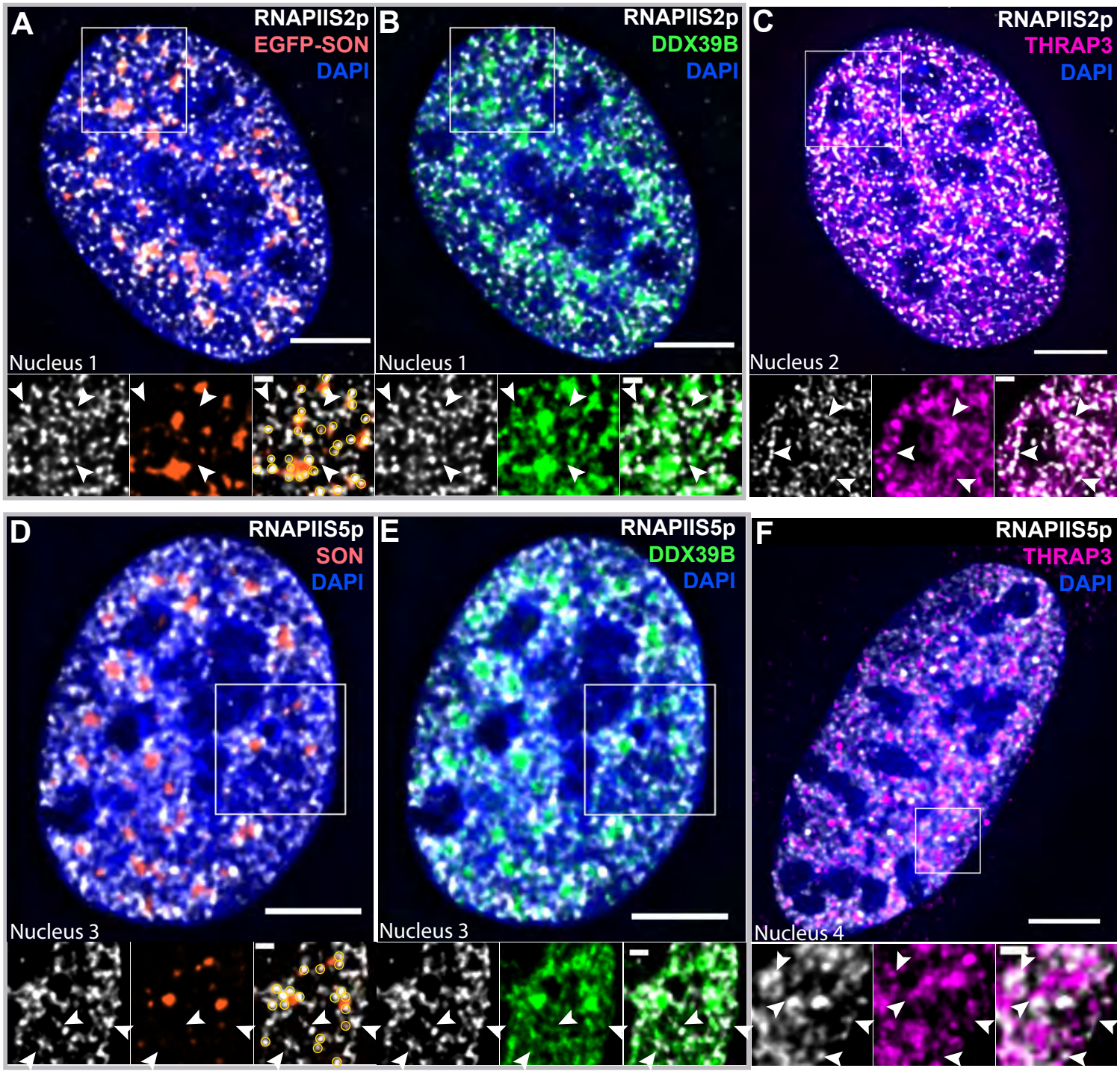
A
RNAPIIS2p
EGFP-SON
DAPI
Nucleus 1
B
RNAPIIS2p
DDX39B
DAPI
Nucleus 1
C
RNAPIIS2p
THRAP3
DAPI
Nucleus 2
D
RNAPIIS5p
SON
DAPI
Nucleus 3
E
RNAPIIS5p
DDX39B
DAPI
Nucleus 3
F
RNAPIIS5p
THRAP3
DAPI
Nucleus 4

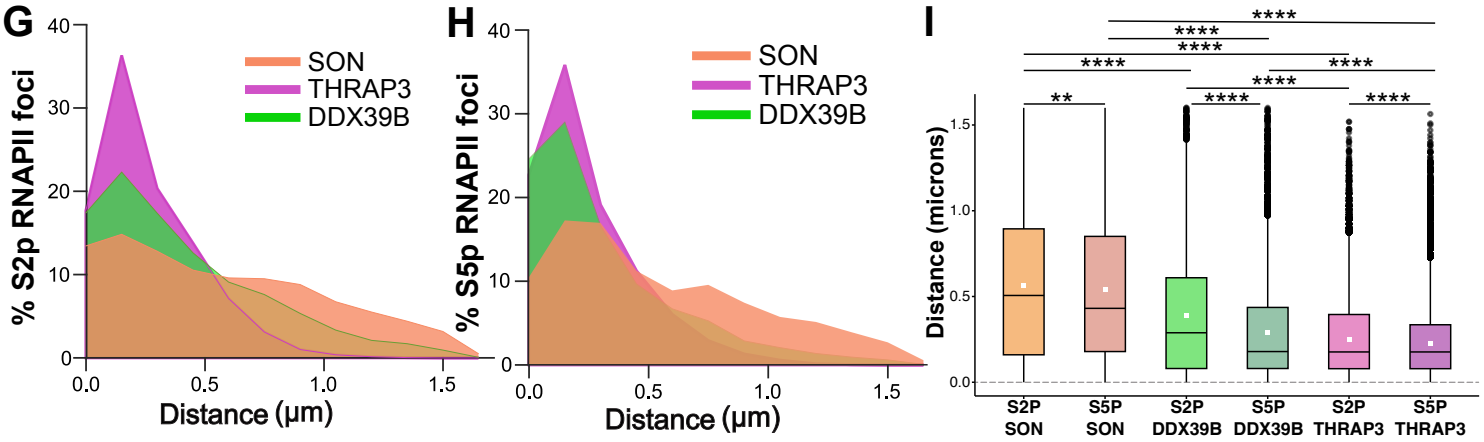
G
% S2p RNAPII foci
Distance (µm)
SON
THRAP3
DDX39B
H
% S5p RNAPII foci
Distance (µm)
SON
THRAP3
DDX39B
I
Distance (microns)
S2P SON
S5P SON
S2P DDX39B
S5P DDX39B
S2P THRAP3
S5P THRAP3

Figure 4

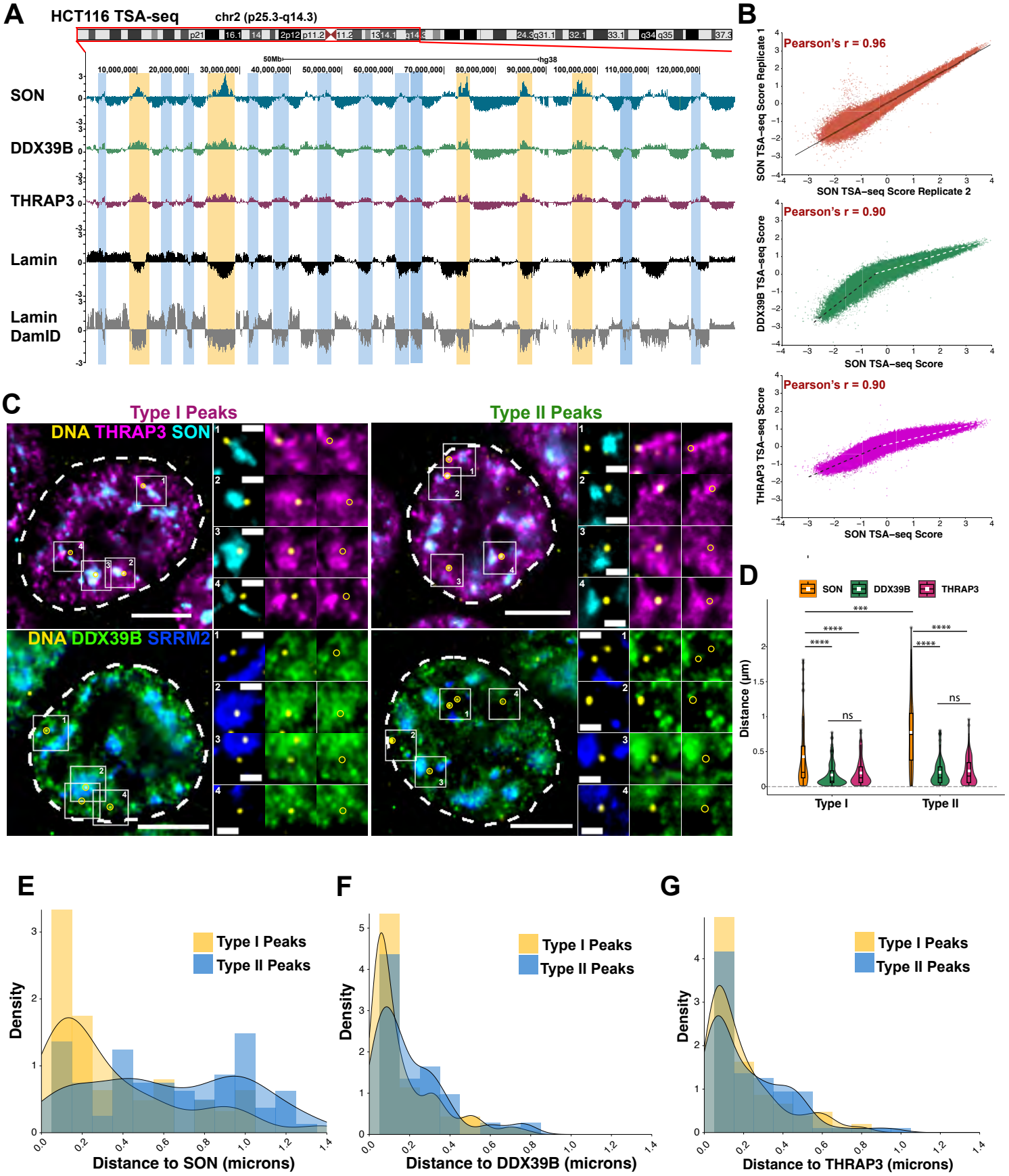
A
HCT116 TSA-seq
chr2 (p25.3-q14.3)
SON
DDX39B
THRAP3
Lamin
Lamin DamID
B
Pearson's r = 0.96
SON TSA-seq Score Replicate 1
SON TSA-seq Score Replicate 2
Pearson's r = 0.90
DDX39B TSA-seq Score
SON TSA-seq Score
Pearson's r = 0.90
THRAP3 TSA-seq Score
SON TSA-seq Score
C
Type I Peaks
Type II Peaks
DNA THRAP3 SON
DNA DDX39B SRRM2
D
SON
DDX39B
THRAP3
Distance (µm)
Type I
Type II
E
Type I Peaks
Type II Peaks
Density
Distance to SON (microns)
F
Type I Peaks
Type II Peaks
Density
Distance to DDX39B (microns)
G
Type I Peaks
Type II Peaks
Density
Distance to THRAP3 (microns)

Figure 5

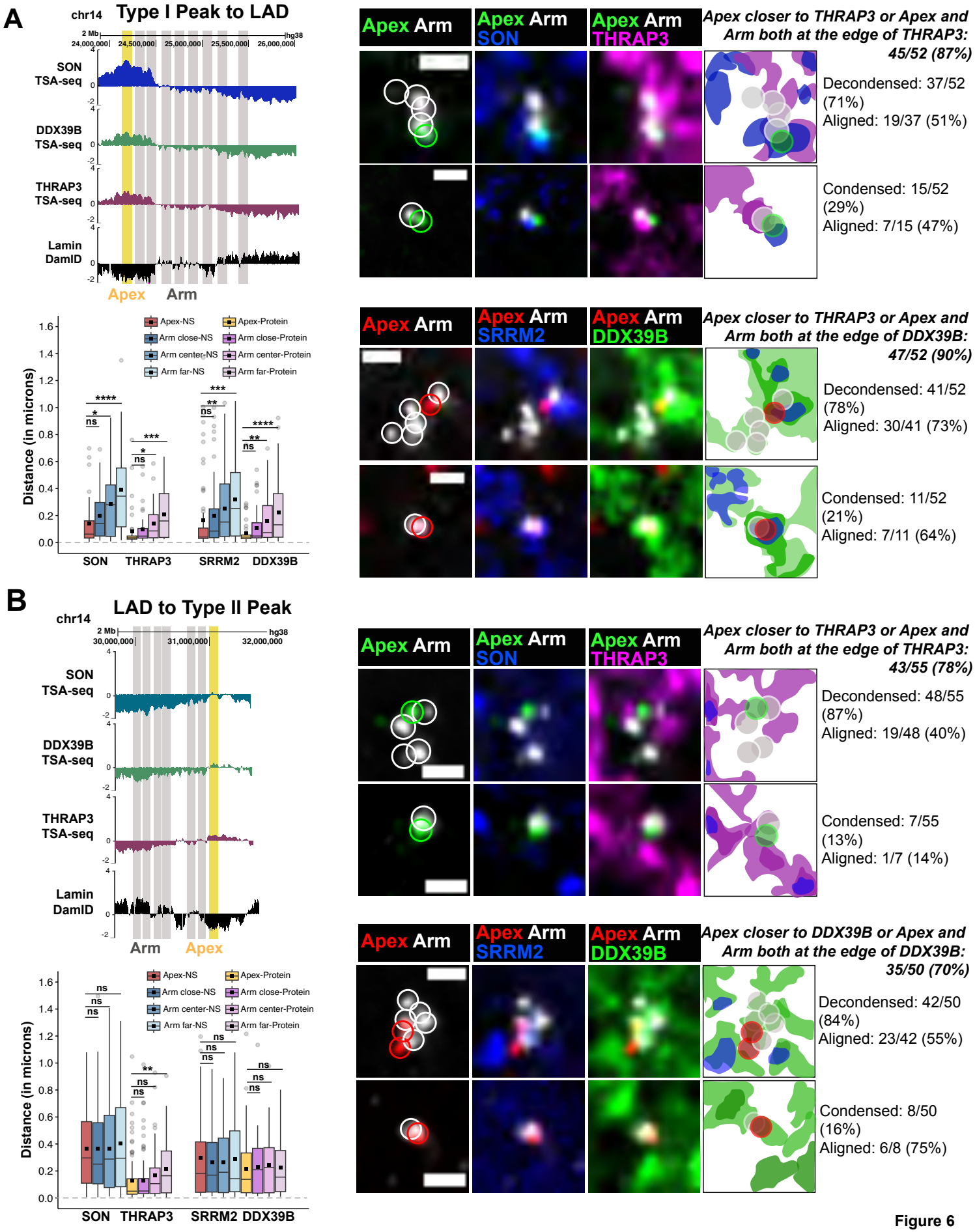
A
chr14
Type I Peak to LAD
2 Mb
hg38
24,000,000
24,500,000
25,000,000
25,500,000
26,000,000
SON TSA-seq
DDX39B TSA-seq
THRAP3 TSA-seq
Lamin DamID
Apex
Arm
Apex-NS
Apex-Protein
Arm close-NS
Arm close-Protein
Arm center-NS
Arm center-Protein
Arm far-NS
Arm far-Protein
Distance (in microns)
SON
THRAP3
SRRM2
DDX39B
Apex Arm
Apex Arm SON
Apex Arm THRAP3
Apex closer to THRAP3 or Apex and Arm both at the edge of THRAP3: 45/52 (87%)
Decondensed: 37/52 (71%)
Aligned: 19/37 (51%)
Condensed: 15/52 (29%)
Aligned: 7/15 (47%)
Apex Arm SRRM2
Apex Arm DDX39B
Apex closer to THRAP3 or Apex and Arm both at the edge of DDX39B: 47/52 (90%)
Decondensed: 41/52 (78%)
Aligned: 30/41 (73%)
Condensed: 11/52 (21%)
Aligned: 7/11 (64%)
B
LAD to Type II Peak
30,000,000
31,000,000
32,000,000
Apex closer to THRAP3 or Apex and Arm both at the edge of THRAP3: 43/55 (78%)
Decondensed: 48/55 (87%)
Aligned: 19/48 (40%)
Condensed: 7/55 (13%)
Aligned: 1/7 (14%)
Apex closer to DDX39B or Apex and Arm both at the edge of DDX39B: 35/50 (70%)
Decondensed: 42/50 (84%)
Aligned: 23/42 (55%)
Condensed: 8/50 (16%)
Aligned: 6/8 (75%)

Figure 6

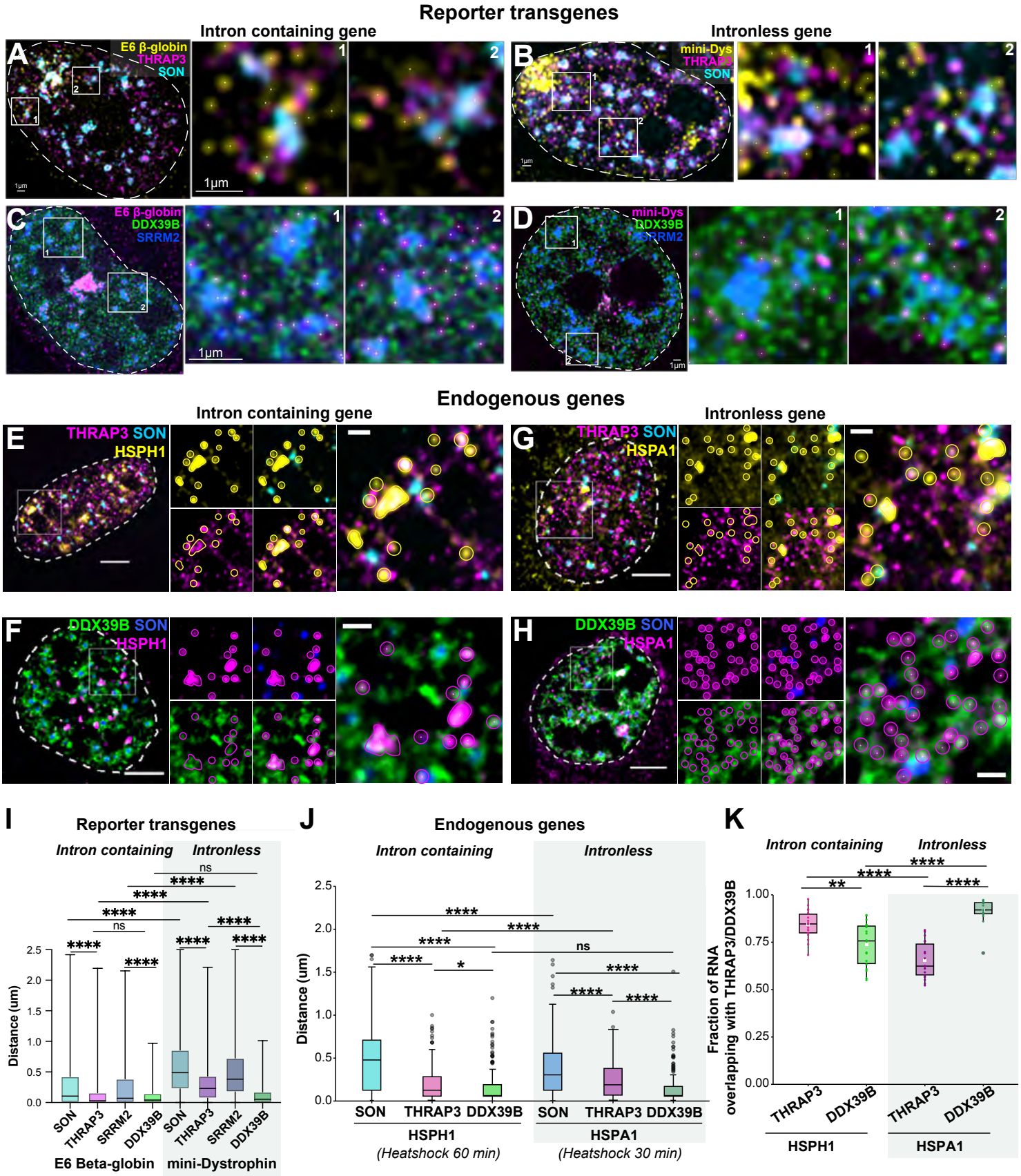
Reporter transgenes
Intron containing gene
Intronless gene
A
E6 β-globin
THRAP3
SON
B
mini-Dys
THRAP3
SON
C
E6 β-globin
DDX39B
SRRM2
D
mini-Dys
DDX39B
SRRM2
1μm
Endogenous genes
Intron containing gene
Intronless gene
E
THRAP3 SON
HSPH1
G
THRAP3 SON
HSPA1
F
DDX39B SON
HSPH1
H
DDX39B SON
HSPA1
I
Reporter transgenes
Intron containing
Intronless
Distance (um)
SON
THRAP3
SRRM2
DDX39B
E6 Beta-globin
mini-Dystrophin
J
Endogenous genes
Intron containing
Intronless
Distance (um)
SON
THRAP3
DDX39B
HSPH1
(Heatshock 60 min)
HSPA1
(Heatshock 30 min)
K
Intron containing
Intronless
Fraction of RNA overlapping with THRAP3/DDX39B
THRAP3
DDX39B
HSPH1
HSPA1

Figure 7

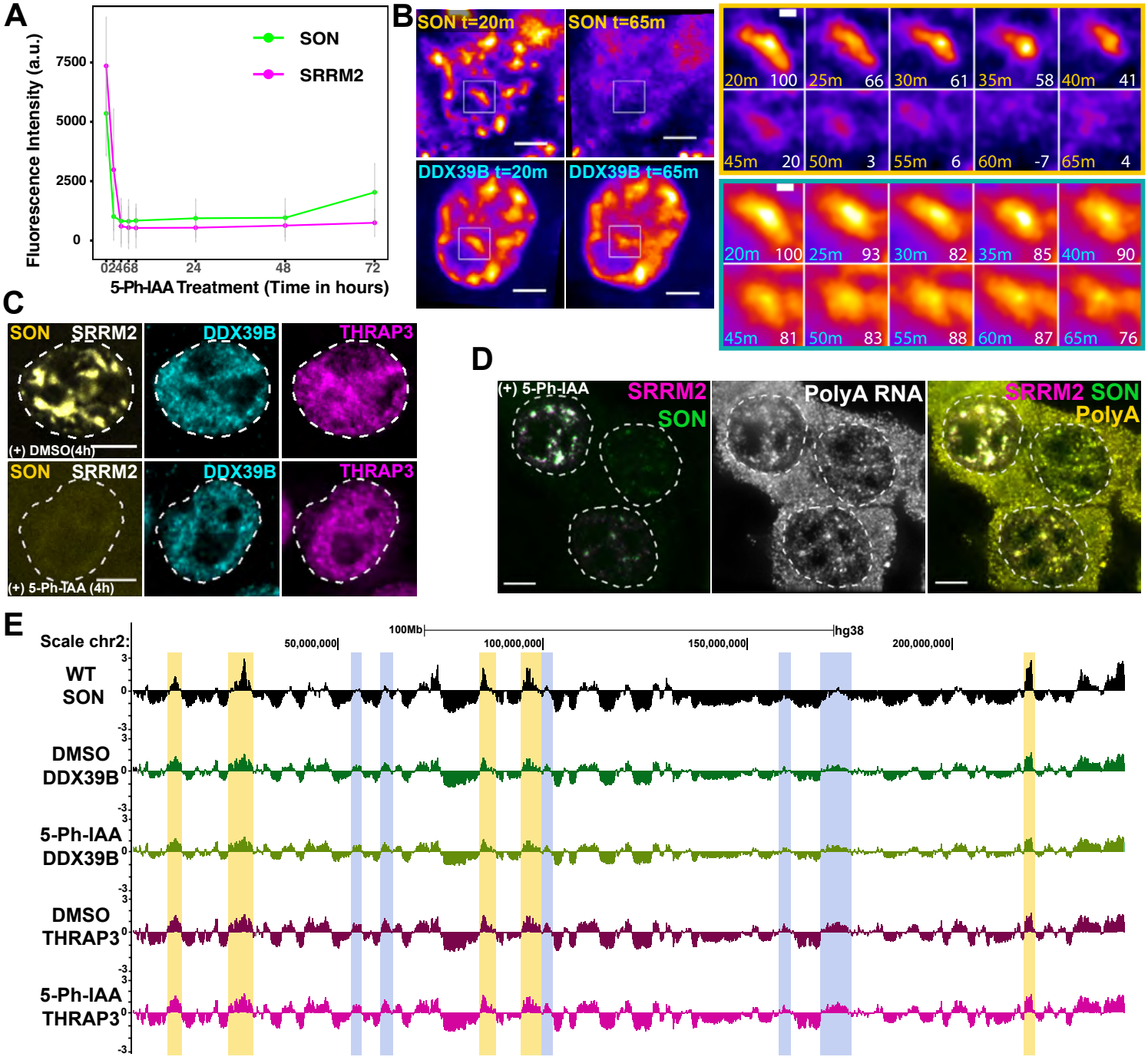
A
Fluorescence Intensity (a.u.)
7500
5000
2500
0
SON
SRRM2
02468
24
48
72
5-Ph-IAA Treatment (Time in hours)
B
SON t=20m
SON t=65m
DDX39B t=20m
DDX39B t=65m
20m 100
25m 66
30m 61
35m 58
40m 41
45m 20
50m 3
55m 6
60m -7
65m 4
20m 100
25m 93
30m 82
35m 85
40m 90
45m 81
50m 83
55m 88
60m 87
65m 76
C
SON
SRRM2
DDX39B
THRAP3
(+) DMSO(4h)
(+) 5-Ph-IAA (4h)
D
(+) 5-Ph-IAA
SRRM2
SON
PolyA RNA
SRRM2 SON
PolyA
E
Scale chr2:
100Mb
hg38
50,000,000
100,000,000
150,000,000
200,000,000
WT SON
DMSO DDX39B
5-Ph-IAA DDX39B
DMSO THRAP3
5-Ph-IAA THRAP3
F
Genes within Type I peaks
Genes within Type II peaks
−log10(FDR)
log FC
G
Genes within Type I peaks
Genes within Type II peaks
123 Upregulated
62 Downregulated
log FC
Mean SON TSA−seq Score
H
Genes within Type I peaks
Genes within Type II peaks
Upregulated 162 192
Downregulated 897 144
log FC
Density

Figure 8

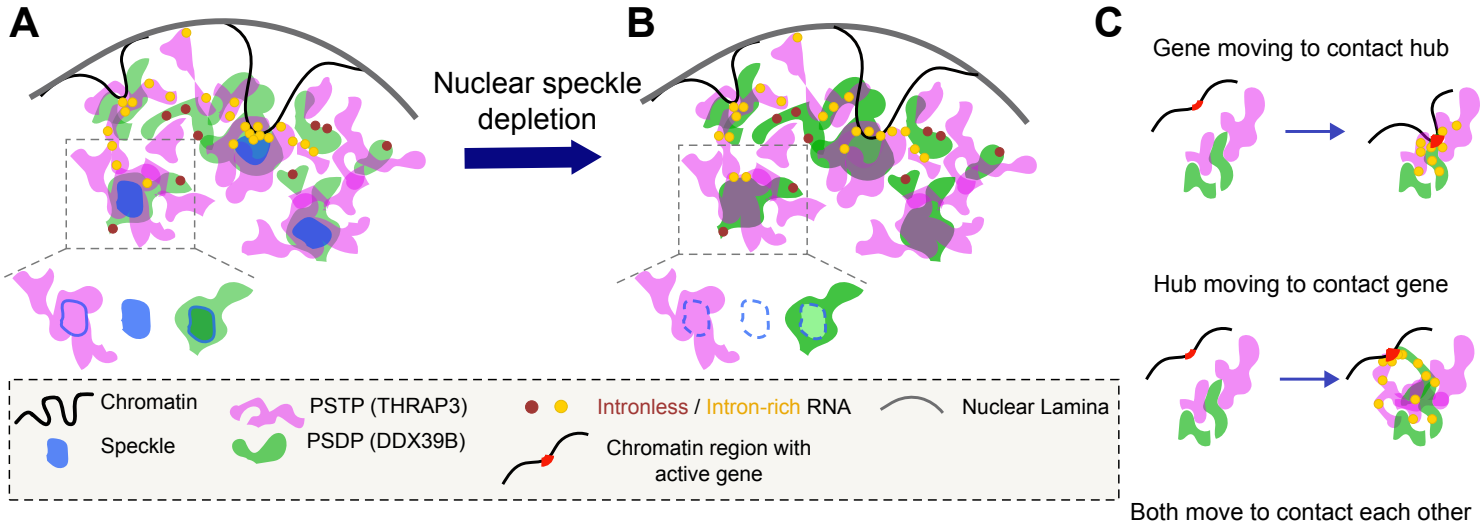

Interchromatin space divided into distinct networks in addition to nuclear speckles.

These networks interact with active DNA.

PSTP and PSDP foci overlap differentially with different subsets of RNPs as they move through the IC space

Networks maintained even after speckles are depleted.

Gene positioning remains unaltered.

Are speckles specialized bodies for added efficiency above the basal function of these networks?

Figure 9